ESTIMATION OF GUIDED WAVES FROM CROSS-CORRELATIONS OF DIFFUSE WAVEFIELDS FOR PASSIVE STRUCTURAL HEALTH MONITORING

A Thesis
Presented to
The Academic Faculty

by

Adelaide A. Duroux

In Partial Fulfillment
of the Requirements for the Degree
Master of Science in Mechanical Engineering in the
Woodruff School of Mechanical Engineering

Georgia Institute of Technology
May 2009

ESTIMATION OF GUIDED WAVES FROM CROSS-CORRELATIONS OF DIFFUSE WAVEFIELDS FOR PASSIVE STRUCTURAL HEALTH MONITORING

Approved by:

Dr. Karim G. Sabra, Advisor
Woodruff School of Mechanical Engineering
Georgia Institute of Technology

Dr. Massimo Ruzzene
School of Aerospace Engineering
Georgia Institute of Technology

Dr. Jianmin Qu
Woodruff School of Mechanical Engineering
Georgia Institute of Technology

Date Approved: March 3rd, 2009

ACKNOWLEDGEMENTS

My sincere gratitude goes to everyone who has supported me during my studies at Georgia Institute of Technology. The research presented in this thesis would not have been possible without the support of many people.

First of all, I would like to thank the members of my supervisory committee: Prof. Karim Sabra, Prof. Massimo Ruzzene, and Prof. Jianmin Qu.

Deepest gratitude is due to my advisor, Prof. Karim Sabra who was abundantly helpful and offered invaluable assistance, support and guidance; his efforts made my stay at Georgia Tech possible in the first place. I want to thank him for his steady encouragement during the different stages of my research.

My gratefulness also goes to Prof. Massimo Ruzzene who provided me with so much of the assistance and equipment that was needed for these experiments. I have sincerely appreciated his priceless advices and help in all stages of this research.

Special thanks go to Prof. Jianmin Qu for being an outstanding teacher.

I am also immensely grateful for the help that I have received from other faculty, staff, and graduate students during my tenure at Georgia Tech. My thankfulness goes especially to James Ayers, Dr. Vin Sharma and Wes Langston, for their considerable help and time in setting up my experiments. This project would be nowhere near what it is today without their knowledge and skills shared gratefully with me. Special thanks also go to my lab mates and friends for their supports and positive work environment that make my stay even more joyful.

I also want to express my gratitude towards the staff of my engineering school in France who gave me this unique opportunity to pursue a double degree program between ENSTA-ParisTech and Georgia Institute of Technology. Especially I want to thank Prof. Antoine Chaigne for supervising this exchange program and his steady support at all stages of my research.

Finally I wish to express my love and gratitude to my American family, parents, two sisters and brother-in-laws who have supported me before and during my time in Atlanta. Their unlimited confidence and encouragement are an important key in the success of my studies.

TABLE OF CONTENTS

LIST OF TABLES

LIST OF FIGURES

LIST OF SYMBOLS AND ABBREVIATIONS

SHM	Structural Health Monitoring
DFI	Diffuse Field Interferometry
FT ; FFT	Fourier Transform; Fast Fourier Transform
PZT	Piezoelectric Transducer
SLDV	Scanning Laser Doppler Vibrometer
CC	Cross-correlation
GF	Green's function
$SNR(t)$	Coherent signal-to-noise ratio
$\otimes$	Symbol for the convolution operation
*	Symbol for the conjugation operation
< >	Symbol for averaging
α	Symbol for proportional to used in figures only
t ; t'; u	Time coordinate
ω ; ω_i	Angular frequency $2\pi f$
f_c	Center frequency of the signal band
N	Secondary sources
T ; T_r ; T_i ; T_{max}	Recordings duration
B ; B_i ; B_{laser}	Frequency bandwidth of the recorded signals

$S_i(t)\,;\ S_i^j(t)$	Reverberating signals (diffuse field) generated by the jth remote source's and recorded at point #i
$C_{ik}^j(t)$	Cross-correlation between $S_i^j(t)$ and $S_k^j(t)$
$C_{ik}(t)$	Average of the cross-correlations $C_{ik}^j(t)$ obtained from each secondary source *j* between sensor #i and #k
$G_{ik}(t)$	Local Green's function between sensor #i and #k
$\tilde{G}_{12}(\omega)\ ;\ G_{12}(t)$	Causal impulse response in the frequency and time domain
$\tilde{G}_{21}(\omega)\ ;\ G_{21}(-t)$	Anti-causal impulse response in the frequency and time domain
D	Actual distance between sensors #1 and #2
$\boldsymbol{r}_i$	Location of the sensors
$\boldsymbol{r}_{s,j}$	Spatial distribution uncorrelated elastic sources
L_{ij}	Distance between measured points
Act1 ; Act2	Location of the piezoelectric actuators on the plate
t_o	A_0 mode arrival time
$V_{12}(t)$	Variance
std	Standard deviation
$NL(i)$	Incoherent noise level
β	Noise spectrum
Q	Sensors' transfer function and the exciting sources spectrum
Ω	Factor set by the attenuation in the medium
$I(t)$	Envelope of the recorded signal averaged over the *N* sources
$I_c^2(t)$	Temporal evolution of the averaged intensity of the decaying elastic wavefield i.e. the signal's envelope

$I_o(t)$	Amplitude of the signal's envelope
$F(t)$	Function taking into account the combined effect of transducer's response (in phase and amplitude) and the normalized autocorrelation of the source signal
τ_D	Decay time
σ_N^2	Variance of the idealized noise field
δ_{ij}	Kronecker delta function
SNR_r	Signal-to-noise ratio of the recorded diffuse waveforms ($= I_o^2(t)/\sigma_N^2$)
$R(N;T_l)$	Relative amplitude changes of the coherent A0 arrival amplitude
Ts ; Ts_{new}	Recording step of time and reassigned step of time (3.9e-7; 3.9e-8)
C_p ; C; C_i	Phase velocity
C_g	Group velocity
λ	Wavelength
τ	Time delay
R_{lm}	Ratio of the A_0 mode amplitude in the damaged case to the undamaged case
γ_{lm}	Relative cumulated decay of the A_0 mode along the inter-sensor path of length L_{lm}
$\boldsymbol{\gamma}$	Column vector of cumulated decay estimated γ_{lm} from the cross-correlation time-function
α_0	Attenuation determined from the median value of the measured quantities γ_{lm} / L_{lm}

$\boldsymbol{\alpha}$	Column vector of the local attenuation coefficient $\alpha(i)$ at each grid cell #i
Φ	Forward mapping matrix (or kernel)
Σ_T	Measurement-error covariance matrix
Σ_s	Slowness matrix
σ_s	$(2m^{-1})$ a-priori (large) variance in local attenuation
$D_{i,j}$	The distance (in cm) between the center of the i^{th} and j^{th} grid cell

SUMMARY

The detection of defect is a real challenge in Structural Health Monitoring (SHM). This thesis suggests the potential for a Structural Health Monitoring method for aircraft panels based on passive ultrasound imaging reconstructed from diffuse fields.

This study will, first, present passive-only reconstruction of coherent Lamb waves (80-200 kHz) i.e. estimation of the Green's functions (impulse responses) experimentally from full-field measurements obtained with a scanning Laser Doppler Velocimeter in an aluminum plate of thickness comparable to aircraft fuselage and wing panels. Diffuse fields were generated by probing the structure at random locations with a few sources (actuators or laser). In particular, the influence of the noise source characteristics (location, number, frequency spectrum, and recording duration) on the signal-to-noise ratio of the emerging coherent waveform will be investigated. This first part is based on recent theoretical and experimental studies in a wide range of applications, which have demonstrated that Green's functions can be extracted from cross-correlation of diffuse fields using only passive sensors.

Secondly, the knowledge of the Green's functions between large numbers of points can be used to successfully identify and localize damage in complex structural components. This provides the wealth of a-priori information necessary to detect and localize "secondary" sources, such as damages, when only a limited number of sensors are actually mounted on the structure. The approach in this thesis relies on the detailed knowledge of the structural response, which is exclusively obtained through experimental measurements performed on the actual component under consideration.

CHAPTER 1

INTRODUCTION

Structural health monitoring (SHM) often relies on propagating elastic waves (e.g. guided waves) through a structure using embedded sensors in order to assess its structural integrity and detect eventual degradations. However most inspected structures are geometrically complex (e.g. aircraft wings): rivets, holes and stiffeners cause scattering, and subsequent multiple reflections also enhance modal conversion, particularly at high frequencies. Indeed the superposition and complex interaction of guided waves can rapidly lead to complicated waveforms away from the elastic source (e.g. piezoelectric actuator or laser). Hence, the geometric complexity of the inspected structures enhances the randomization of the elastic energy within these structures and thus actually favors the formation of diffuse fields over long reverberation time. Fully diffuse wave fields are often defined as ones that are globally equipartitioned, with all normal modes having uncorrelated amplitudes with equal mean squares [Weaver 1982; Weaver 1984; Evans and Cawley 1999; Weaver 2004]. Overall, a structure capable of sustaining a diffuse field must be lightly damped, allowing many reflections of the initial wave energy.

Diffuse fields in structures have an apparent random nature and are thus generally discarded in conventional SHM systems. However, despite their apparent complexity, the diffuse field signals generated by distant ultrasonic sources can be used to reconstruct *remotely* the *local* elastic response between a pair of (embedded) sensors [Weaver and Lobkiss 2001; Larose et al. 2007, Sabra et al. 2008] (see Fig. 1). For instance, for

practical applications, the distant ultrasonic sources could be located in easily accessible areas during routine maintenance operations (e.g. on the outer wing of aircraft structure) while the sensors would be embedded in hard to reach area (e.g. in the vicinity of a hidden structural “hot-spots” within the wing panels) where structural failure (e.g. fatigue cracks) is likely to occur. Indeed several theoretical and experimental studies have demonstrated a general relationship between the Green’s function (or impulse response) and the cross-correlations of diffuse fields or ambient noise records for various environments and frequency ranges such as seismology [Shapiro et al. 2005; Sabra et al. 2005c], underwater acoustics [Roux et al. 2004; Sabra et al. 2005a; 2005b], civil engineering [Farrar and James 1997; Snieder and Cafak 2006], low-frequency (< 5 kHz) flexural properties identification of hydrofoils [Sabra et al. 2007] and high frequency ultrasonics (~Mhz) [Weaver and Lobkis, 2001; Larose et al. 2006; Van Wijk 2006; Langley 2007] and guided wave measurements (~kHz) [Larose et al. 2007; Sabra et al. 2008]. In the context of SHM methodology, we will refer to this coherent processing of diffuse field as *Diffuse Field Interferometry* (DFI) since this technique allows for compensation of signal distortion accumulated along the propagation paths up to the (embedded) sensors locations. The term "interferometry" generally refers to the study of interference phenomena between pairs of signals in order to obtain information from the phase differences between them. Indeed, DFI can be thought as an analogy with an astronomical technique in which light from a bright "guide star" is used to correct atmospheric aberration of weaker objects that are nearby in the angular sense. More specifically, DFI unravels the recorded diffuse fields through a correlation process and extracts coherent (guided) waves which travel locally between a pair of sensors

(see Fig. 1). These coherent waveforms are similar to those obtained from conventional pitch-catch measurements between a source and receiver pair (i.e. the Green's function). The sources spectra define the frequency bandwidth in which the Green's function response can be retrieved. Thus overall, DFI provides a mean for SHM without a local source. Furthermore, DFI offers an inherently safe sensing technique for monitoring structural hot-spots in hazardous regions (e.g. fuel transfer holes in the wing risers), since it does not require locally an active source, which could cause electrical sparks, but only sensors.

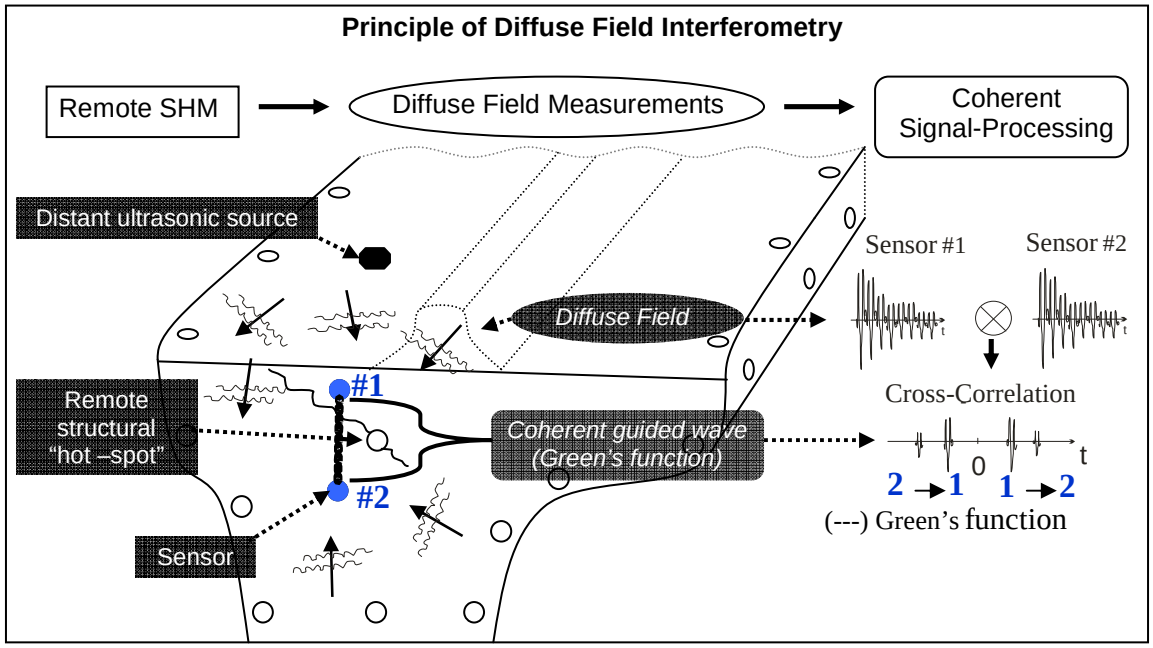

FIGURE 1: Principle of the Diffuse Field Interferometry (DFI) technique: A coherent guided wave propagating locally between two sensors (and proportional to the actual Green's function) can be extracted from the cross-correlation of the recorded diffuse field (e.g. scattered waves) generated by a distant ultrasonic source (see Chapter 2, Eq. (4) and Eq. (6)). DFI provides a mean for monitoring remote structural hot-spots in an elastic structure, illustrated here by a rivet hole (note the crack running leftward from it) on a random structure.

In practice, being able to generate a fully diffuse field in the monitored structure is critical in order to extract an accurate estimate of the Green's function (i.e. with the correct phase and amplitude) from the DFI output. Hence, a practical issue in the

implementation of DFI resides in selecting the number *N* of secondary ultrasonic sources and their locations in order to generate a fully diffuse field in the structure after superposition of their individual contributions at the receiver. Furthermore, in complex structures, the measured signals are typically non-stationary signals with an exponentially decaying coda which is dominated by multiply scattered waves. On one hand, it has been shown that the diffuse-field regime is more likely to be achieved within the late coda waves (after multiple reflections have occurred) than during the early ballistic direct arrivals [Weaver et al. 1986; Larose et al. 2004; Paul et al. 2005]. On the other hand, coda waves have an overall exponential decay, mainly determined by elastic attenuation in most cases and thus late coda waves can quickly be contaminated by measurements noise or electronic noise (e.g. due to imperfect sensors). Thus selecting the optimal portion of duration *T* of the recorded signals for implementing DFI may not be straightforward and indeed depends on the experimental conditions. One metric commonly used to asses the performance of DFI is the signal-to-noise ratio (*SNR*) of the emerging coherent arrivals from the cross-correlation waveform obtained from DFI output. This coherent *SNR* is defined as the ratio of the maximum amplitude of the coherent waveform (i.e. obtained from the mean of the DFI output) to the standard deviation of temporal residuals of the cross-correlation time-function (i.e. determined by the square root of the variance of the DFI output). Hence for a given measurement system and secondary sources configuration, the variance level sets the measurement precision (e.g. for phase or group velocity measurements from the extracted coherent guided waves). Thus, a relevant question for practical SHM systems based on DFI may be how to achieve a given coherent *SNR* level in order to ensure accurate defect detection between a pair of passive

sensors? One contribution to the variance of the DFI output results from the imperfect averaging over the N secondary sources or recordings duration T when computing an estimate of the expected value of the cross-correlation waveform (also called “pseudo-noise” contribution by Larose et al. 2008) as compared to the ideal case of using recordings of fully diffuse wavefield. Based on previous studies considering only this “pseudo-noise” contribution to the variance [Sabra et al. 2005b; Weaver et al. 2005; Larose et al. 2008], the coherent *SNR* is expected to grow theoretically as the square root of both the processed diffuse field duration T and the number N of secondary ultrasonic sources, all others parameters kept constant. Larose et al. (2008) have presented general theoretical predictions and numerical studies clearly emphasizing the role of multiple scattering on reducing the level of the “pseudo-noise” due to imperfect ensemble averaging (in space or time) of computed cross-correlation waveforms. However the influence of experimental sensor noise or electrical noise (i.e. “incoherent measurement noise”) on the variance of the obtained coherent waveforms has not been explicitly described by the previous literature. Furthermore, few experimental studies [Larose et al. 2007; Sabra et al. 2008] have been conducted to assess the performance of DFI for SHM applications: for instance regarding the precision of the phase and group velocity measurements from DFI, in addition to the usual coherent SNR metric.

The main objective of this thesis is to investigate experimentally the emergence of coherent lamb waves from the cross-correlations output of the DFI technique in a thin plate with complex geometry and boundaries in order to assess the performance of DFI for practical SHM application and thus complement previous theoretical studies [Weaver

and Lobkis 2004; Weaver et al. 2005; Sabra et al. 2005b; Larose et al. 2008]. To do so, the diffuse nature of the vibrating field recorded over the whole plate for long recording time was assessed using a scanning laser vibrometer. Furthermore, the coherent *SNR* as well as the accuracy of the phase and group velocities of the extracted coherent guided wave arrivals from DFI were measured to quantify: 1) the performance of various processing schemes of the recorded diffuse fields, 2) the effect of the spatial configuration of the secondary ultrasonic sources and 3) the influence of incoherent measurement noise (e.g. sensor noise) on the DFI performance.

Following this introductory section, the second chapter of the thesis exposes the theory linked to the reconstruction of the Green's function and to the variance prediction in the presence of incoherent measurement noise. Chapter 3 presents first the experimental setup, followed by the study of the onset of the diffuse field regime for waves propagating in a plate with complex geometry (chaotic plate) and finally the experimental parametric study of the coherent *SNR* and accuracy of the phase and group velocity measurements to assess the performance of DFI in chaotic plate. Chapter 4 details the experimental setup and results for the detection of a simulated defect by applying the technique seen in Chapter 3. Chapter 5 will present the influence of boundary conditions on the measurement from DFI to highlight the robustness of this technique. Finally the conclusions drawn from this study are summarized in the last chapter of this thesis.

CHAPTER 2

THEORETICAL BACKGROUND

2.1 Reconstruction of the estimate of the true Green's function (GF)

The way to retrieve the GF in passive and conventional also called active testing is different. Indeed active testing uses one sensor to broadcast and another one to record (Fig. 2.a), passive testing (Fig. 2.b) instead uses only sensors to extract the GF from ambient noise or diffuse field recordings.

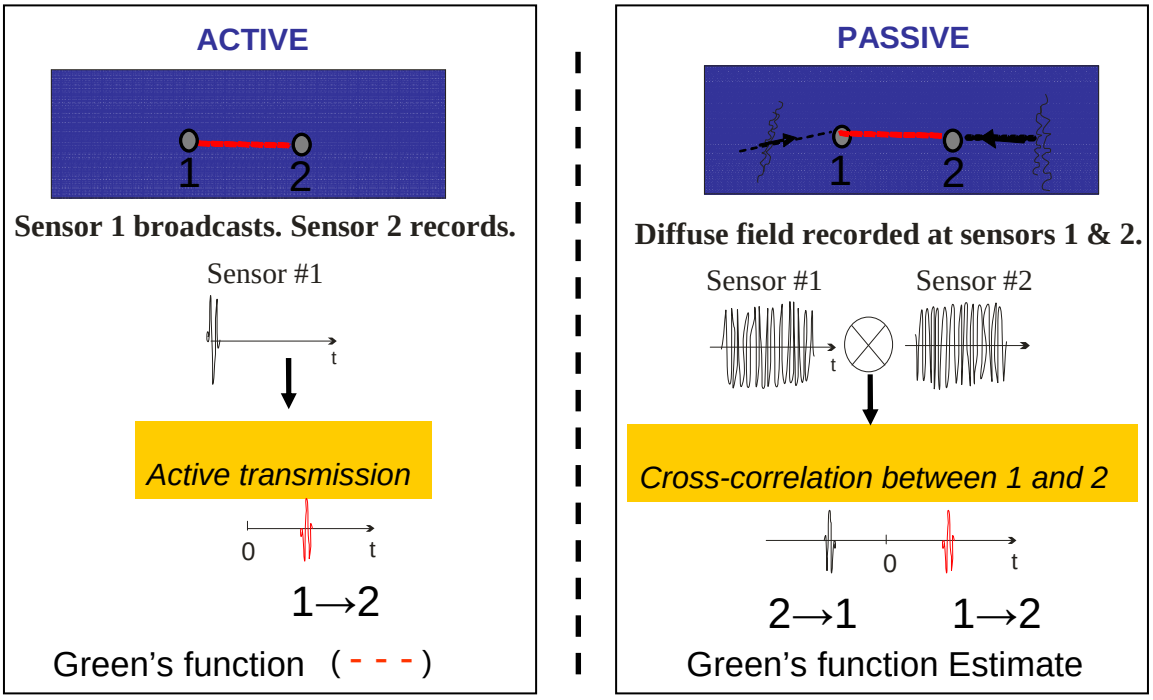

(a) (b)

FIGURE 2.a. Active sensing principle. **2.b.** Passive testing principle.

The main assumption for the theoretical derivations of the DFI technique is that the wavefield resulting from the excitations of all remote, or secondary, sources in the structure is homogeneous in space and in time which requires the field to be diffused

[Weaver and Lobkis 2004]. Indeed having a diffuse field ensures that all paths existing between a pair of sensors are fully illuminated by the various wave components of the diffuse field.

The cross-correlation between the diffuse field recorded at the two sensors (#1 and #2), denoted $S_1(t)$ and $S_2(t)$ respectively, is defined by the following formula.

$$C_{12}(\tau) = \int_{-\infty}^{\infty} S_1(t)\, S_2(t+\tau)\mathrm{d}\, t \tag{1}$$

where τ is the time delay.

On a specific time-window of length T_r, the previous formula becomes:

$$< C_{12}(t) >= \frac{1}{T_r} \int_{-\frac{T_r}{2}}^{+\frac{T_r}{2}} S_1(\tau) S_2(t+\tau) d\tau \tag{2}$$

It can be shown that the Fourier Transform (FT) of the cross-correlation is related to the frequency-domain GF through the following formula [Roux et al. 2004; Weaver and Lobkis 2004]:

$$< \tilde{C}_{12}(\omega) >= i\beta(\tilde{G}_{12}(\omega) - \tilde{G}_{21}^{*}(\omega)) \tag{3}$$

where β is the noise spectrum, $\tilde{G}_{12}(\omega)$ is the causal impulse response, $\tilde{G}_{21}(\omega)$ is the anti-causal impulse response.

Furthermore in the time domain equivalent of Eq. (3), it is the time-derivative of the cross-correlations which actually yields the time-domain GF as it is illustrated here:

$$\frac{d < C_{12}(t) >}{dt} \approx Q\Omega D(G_{12}(t) - G_{21}(-t)) \tag{4}$$

where Q is set by the sensors' transfer function and the exciting sources spectrum, Ω is a

factor set by the attenuation in the medium, and D is the actual distance between sensors #1 and #2.

Diffuse field can be easily generated in aircraft fuselage and wing structures thanks to their complex geometry and the random excitation in flight. Hence, being able to reconstruct the local GF with the diffuse part of a signal would be of big interest.

2.2 Definitions of Mean and Variance of the DFI estimate

As stated in the introductory section, DFI is typically implemented by using one or several remote sources distributed throughout the structure of interest away from the sensors region to generate a diffuse field in the sensor region (see Fig. 1). The cross-correlation $C_{12}^{j}(t)$ between the reverberating signals $S_1^{j}(t)$ and $S_2^{j}(t)$ generated by the jth remote source and recorded by two sensors #1 and #2 respectively is given by:

$$C_{12}^{j}(t) = \frac{1}{T}\int_{0}^{T} S_1^{j}(\tau) S_2^{j}(t+\tau)\, d\tau \tag{5}$$

where T is the duration of the reverberating recordings. The temporal integration in Eq. (5) physically corresponds to a temporal averaging operation over the finite duration T. The expected value of the DFI estimate $C_{12}(t)$ can be constructed from an ensemble average of the cross-correlations $C_{12}^{j}(t)$ obtained from each secondary source j:

$$C_{12}(t) = \frac{1}{N}\sum_{j=1}^{N} C_{12}^{j}(t) \tag{6}$$

The ensemble average over all remote sources helps establishing a diffuse regime at the receiver's locations by cumulating multiple realizations of the scattered field in the

structure of interest. Simply put, the more complex and reverberant the structure is, the fewer sources are needed, in general, to generate in practice a diffuse field throughout the structure.

Furthermore, it should be noted that since DFI involves cross-correlating signals originating from the same source event at both sensors (i.e. a coherent processing), only the square of the amplitude spectrum of the signal excitation matters and not its absolute phase (which cancels out in the cross-correlation operation). Hence, various source excitations could indeed be used in practice (e.g. pulse, frequency sweeps, coded sequences) depending on the sensors types and signal-to-noise ratio constraints. Indeed, DFI has even been implemented using random excitations or ambient noise, recorded for instance during flight operation due to air-turbulence [Sabra et al. 2007a]. However, obtaining reliable sources of ambient noise excitations at higher frequencies (~kHz, required for guided-waves sensing) remains challenging.

In practice, the computed mean coherent estimate $C_{12}(t)$ (see Eq. (6)) is only an approximation of the actual local Green's function $G_{12}(t)$ between sensor #1 and #2 (see Eq. (4)). Consequently, $C_{12}(t)$ always contains some residual temporal fluctuations which can blur the identification of the symmetric arrivals of $C_{12}(t)$. High levels of residual fluctuations may potentially prevent the accurate extraction of the local Green's function $G_{12}(t)$ from DFI. The level of these temporal fluctuations can be estimated from the square root of the variance $V_{12}(t)$ of the DFI estimate $C_{12}(t)$ which is defined as [Weaver et al. 2005; Sabra et al. 2005b; Larose et al. 2008]:

$$V_{12}(t) = \frac{1}{N-1}\left(\frac{1}{N}\sum_{j=1}^{N}(C_{12}^{j}(t))^2 - \left(\frac{1}{N}\sum_{j=1}^{N} C_{12}^{j}(t) \right)^2 \right) \quad (7)$$

Finally, as stated in the introduction chapter, the coherent signal-to-noise ratio ($SNR(t)$) of the DFI estimate $C_{12}(t)$ can be defined by:

$$SNR(t) = \frac{C_{12}(t)}{\sqrt{V_{12}(t)}} \quad (8)$$

The value of $SNR(t)$ is a commonly used metric to assess the performance of DFI for estimating the local Green's function $G_{12}(t)$ between sensors #1 and #2. Theoretical predictions of $SNR(t)$ are developed in the next section for a simple model of the recorded signals in a reverberant elastic structure.

2.3 Theoretical prediction of the coherent SNR

Theoretical expressions for the mean $C_{12}(t)$ and variance $V_{12}(t)$ of the DFI estimate variance $V_{12}(t)$ have been previously derived for various recorded signal models (e.g. stationary or non-stationary elastic field) [Weaver et al. 2005; Sabra et al. 2005b; Larose et al. 2008]. To the first order, following the notations of Larose et al. (2008), the theoretical expression of $C_{12}(t)$ reduces to:

$$C_{12}(t) \approx F(t) \otimes (G_{12}(t) - G_{21}(-t)) \cdot \int_0^T I(u)I(t+u)du \quad (9)$$

where $G_{12}(t)$ is the actual Green's function between sensors #1 and #2, $I(t)$ is the envelope of the recorded signal averaged over the N sources (i.e. the square root of the averaged intensity) , T is the recording duration, $F(t)$ is a function taking into account the combined effect of transducer's response (in phase and amplitude) and the normalized

autocorrelation of the source signal (close to a Dirac function for impulsive sources) and the symbol $\otimes$ denotes a convolution operation. When using identical transducers at location #1 and #2 and impulsive remote sources (e.g. laser impulse) to generate the elastic wavefields, $F(t)$ simply acts as band-pass filter on the true Green's function $G_{12}(t)$.

The energy equipartition of the diffuse field is a necessary and sufficient condition to extract the full Green's function from the coherent output of the DFI [Weaver and Lobkis 2004; Paul et al. 2005; Langley 2007]. Structural complexity (e.g. due to random geometry) typically enhances multiple scattering and hence helps achieving a diffuse field regime. Indeed, the existence of a diffuse field ensures that all paths existing between #1 and #2 are fully illuminated, thus leading to an accurate estimate of the Green's function from DFI. The two Green's function terms in Eq. (9) are respectively: 1) the causal impulse response which comes from the portion of the diffuse field propagating from sensor #1 to #2 and yielding a non-zero correlation for a positive time-delay, and 2) the time-reversed (or anti-causal) impulse response which comes from the portion of the diffuse field that propagates from #2 to #1 and yields a non-zero correlation at a negative time-delay (see Fig. 1). Thus, for a fully diffuse field, the cross-correlation is a symmetric function of time, as shown in the following illustration. Hence, in practical applications, symmetric arrivals of $C_{12}(t)$ can be used as reliable estimates of actual paths of the local Green's function $G_{12}(t)$.

Similarly to Eq. (9), the theoretical expression of the variance $V_{12}(t)$ is given by [Weaver et al. 2005; Sabra et al. 2005b; Larose et al. 2008]:

$$V_{12}(t) \approx \frac{1}{2BN}\int_0^T I^2(u)I^2(t+u)du \tag{10}$$

where N is the number of remote sources, T is the recording duration and B is the frequency bandwidth of the recorded signals.

In complex structures, the measured signals at the sensors' locations, generated by an impulsive source, are typically non-stationary signals with an exponentially decaying coda (see Fig. 1). This coda is dominated by multiply scattered waves over long reverberation time. In this case, the temporal evolution of the averaged intensity of the decaying elastic wavefield, noted $I_c^2(t)$ (i.e. the signal's envelope), can be fitted by (see Fig. 7):

$$I_c(t) = I_0 e^{-t/\tau_D} \tag{11}$$

where τ_D is the decay time of the elastic field whose value depends on the scattering properties and elastic attenuation of the structure [Evans and Cawley 1999; Derode et al. 1999; Larose et al. 2008].

Furthermore, in practice, the recorded signals always contained some amount of non-propagating noise (e.g. experimental sensor noise or electrical noise) which hinders the accurate recording of weak multiply scattered signals at longer times. The simplest noise model for this incoherent noise contribution is: an additive stationary homogeneous flat-spectrum band-limited zero-mean random field that is uncorrelated between sensors' locations and uncorrelated with the diffuse elastic wavefield. Since both the reverberating

signal and noise would be subjected to the same filtering in any actual DFI application, the noise bandwidth is assumed to coincide with the signal bandwidth *B*, and, for simplicity, the band-pass filtering is assumed to be ideal (unity band-pass response with complete spectral rejection outside the passband). Under these circumstances, the autocorrelation function of the idealized noise field (at sensor #1 or #2 location) is:

$$< n(r_i,t)n(r_j,t') >= \sigma_N^2 \delta_{ij} \frac{\sin(B\pi(t-t'))}{B\pi(t-t')} \cos(2\pi f_c(t-t')) \qquad (12)$$

where σ_N^2 is the variance of the idealized noise field, δ_{ij} is the Kronecker delta function and $2\pi f_c = (\omega_1 + \omega_2)/2$ is the center frequency of the signal band [Proakis 1995]. It was also assumed that the variance of the noise field σ_N^2 is identical for all measurements. Although this noise-field model is idealized, it allows simplification of the total variance $V_{12}(t)$ and provides gage performance results for actual DFI implementation. In particular, in the expression of the variance $V_{12}(t)$ (see Eq. (10)), the total recorded intensity $I^2(t)$ can then be approximated by $I_c^2(t) + \sigma_N^2$. On the other hand, since the incoherent noise-field is assumed to be spatially uncorrelated and with zero mean, it does not contribute, to the first order, to the mean coherent estimate $C_{12}(t)$. Hence in the numerator of $C_{12}(t)$ the envelope $I(t)$ (associated with the amount of coherent energy flowing between sensor #1 and #2) can then simply be approximated by $I_c(t)$. Consequently, after combining Eq. (9-12) and based on this simple model for noise multiply scattered signals, the theoretical prediction of the signal-to-noise ratio $SNR(t)$ (see Eq. (8)) of the DFI estimate $C_{12}(t)$ is:

$$SNR(t) = \sqrt{2BN}\,\frac{\int_0^T I_c(u)I_c(t+u)du}{\sqrt{\int_0^T \left(\sigma_N^2 + I_c^2(u)\right)\left(\sigma_N^2 + I_c^2(t+u)\right)}} \cdot \left(F(t) \otimes (G_{12}(t) - G_{21}(-t))\right) \qquad (13)$$

which can be rewritten explicitly, after using Eq. (11) as:

$$SNR(t) = \sqrt{2B\tau_D N}\,\frac{SNR_r\left(e^{-\frac{t}{\tau_D}} - e^{-\frac{(2T+t)}{\tau_D}}\right)}{\sqrt{\frac{(SNR_r)^2}{4}\left(e^{-\frac{2t}{\tau_D}} - e^{-2\frac{(2T+t)}{\tau_D}}\right) + \frac{SNR_r}{2}\left(1+e^{-\frac{2t}{\tau_D}}\right)\left(1-e^{-\frac{2T}{\tau_D}}\right) + \frac{T}{\tau_D}}} \qquad (14)$$
$$\cdot \left(F(t) \otimes (G_{12}(t) - G_{21}(-t))\right)$$

where $SNR_r = I_o^2(t)/\sigma_N^2$ is defined as the signal-to-noise ratio of the recorded diffuse waveforms. Figure 3 illustrates the result of the coherent *SNR* in function of SNR_r using parameters from the experiment described in Chapter 3: T=6ms, τ_D=5ms and t=A_0 arrival time = 0.14777ms.

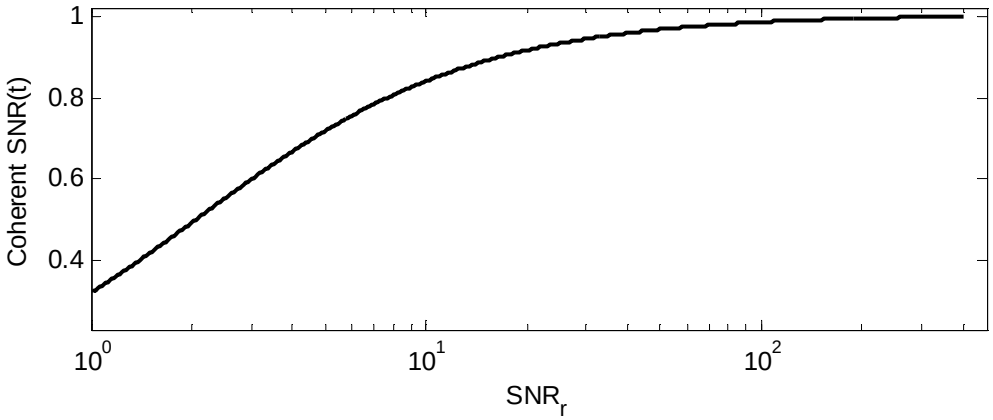

FIGURE 3: Normalized variations of the coherent signal-to-noise ratio (*SNR(t)*) vs. signal-to-noise ratio of the recordings (SNR_r) based on theoretical predictions of Eq. (10) for the parameters: T=6ms, τ_D=5ms and t_0 =A_0 arrival time = 0.14777ms.

Eq. (13-14) can be used to estimate the influence of various parameters such as N (number of sources), B (signal frequency bandwidth), T (recording duration), τ_D (the decay time of the diffuse field signals) and SNR_r on the coherent signal-to-noise ratio

$SNR(t)$ of the cross-correlation waveform. Based on Eq. (13-14), it appears that the parameters *T* and *N* do not have the same influence on the increase of the incoherent *SNR* in the case of noisy recorded waveforms (see Eq. (15)). Indeed, since the incoherent noise component is assumed to be spatially uncorrelated (Eq. (12)), it can be noticed that $SNR(t)$ theoretically grows as $\sqrt{N}$, which is the same dependency found by previous studies not accounting for the incoherent noise component. This physically occurs since adding secondary sources provides additional realizations of the scattered wavefield in the complex structure so that the averaged recorded field is a better approximation of the ideal diffuse elastic wavefield. On the other hand, the dependence of coherent *SNR* with respect to the parameters *T* and τ_D is affected by the presence of incoherent noise, via the parameter SNR_r (recorded signal-to-noise ratio), for the case of non-stationary decaying elastic wavefield.

For low values of SNR_r ($SNR_r << 1$), Eq. (13-14) can be reduced to:

$$SNR(t) = \sqrt{2BN}\,\frac{\tau_D.(\frac{I_0^2}{\sigma_n^2}).\sinh(\frac{T}{\tau_D}).e^{-(\frac{T+t}{\tau_D})}}{\sqrt{T}} \cdot \left(F(t) \otimes (G_{12}(t) - G_{21}(-t))\right) \qquad (15)$$

This case is to be avoided as the incoherent noise is much too high and will then make the reconstruction of the GF difficult. Eq. (13-15) show then that low values of SNR_r for the recorded signals limit the achievable value of the coherent *SNR*, especially if the recordings duration *T* is erroneously selected longer than τ_D. Thus, in the case of weakly-scattered signals and in the presence of incoherent noise, it is often necessary to increase the number of sources *N* in order to reduce the variance $V_{12}(t)$ (i.e increase the coherent

SNR) and improve the convergence of $C_{12}(t)$ towards the true Green's function.

Finally, in the case of high values of the recorded SNR_r (i.e. weak incoherent noise level), the expression of the coherent SNR is, as expected, independent of SNR_r and reduces to the formula expressed in previous studies [Weaver et al. 2005; Sabra et al. 2005b; Larose et al. 2008]:

$$\text{for } SNR_r >> 1 \,, \qquad SNR(t) \approx \sqrt{2B\tau_D N}\, \frac{\sinh(\frac{T}{\tau_D})}{\sqrt{\sinh(\frac{2.T}{\tau_D})}} \cdot \left(F(t) \otimes (G_{12}(t) - G_{21}(-t))\right) \qquad (16)$$

where the classical dependency of $\sqrt{2B\tau_D N}$ (for exponentially decaying diffuse signals, that is T~τ_D) or $\sqrt{2BTN}$ (for stationary signals -such continuous ambient noise- that is $\tau_D \to \infty$) is recovered.

For high level of attenuation (i.e. small decay time τ_D), the recorded signals can be very short, which can lower the values of the coherent SNR (see Eq. (16)). In this case, the late portion of coda of the signals, composed of weak multiply scattered waves, would not contribute significantly to the total correlation $C_{12}(t)$. Hence the DFI process would not benefit from the coherence of these weak multiply scattered waves although they represent the portion of the recorded signal which is closer to the ideal diffuse field regime. Previous experimental studies have proposed to increase the coherent SNR by clipping the amplitude of the recorded signal to an arbitrary threshold in order to artificially enhance the contribution of these weak arrivals in the recorded coda [Larose et al. 2004; Sabra et al. 2008]. This clipping procedure allows maximizing the amount of useful information in the recorded signals which contributes to the mean DFI estimate,

$C_{12}(t)$ obtained from cross-correlation (see Eq. (6)). However if the recorded SNR_r is low, amplitude clipping also artificially enhances the relative importance of the incoherent noise in the late coda. Indeed, very low clipping level of the recorded signals, such as "one-bit clipping", may actually be detrimental to the DFI performance since it artificially amplifies the effect of incoherent noise. The theoretical prediction of Eq. (13) indicates that the clipping level should, as expected, be significantly larger than the level of incoherent noise (σ_N^2) in order to effectively enhance the signal-to-noise ratio $SNR(t)$ of the mean DFI estimate $C_{12}(t)$. Practical selection of this clipping level will be discussed in following experimental chapters.

Overall, the theoretical results in Eq. (13-14) confirmed the role of multiple scattering for accelerating the apparition of the diffuse field regime (for high $SNR(t)$ and large values of τ_D) and hence reducing the variance $V_{12}(t)$. These analytical results suggest that for any given structures (i.e. a given τ_D) and noise level (i.e. SNR_r), some optimal combinations of the parameters N and T exist to reach a given targeted coherent SNR value. However, as discussed by Larose et al. (2008), the simple model of the diffuse signals yielding Eq. (9-11) is not valid if long-range correlations occur in the multiply scattered signals, for instance due to the existence of closed loops or recurrent scattering which may exist in a highly disorganized propagating medium. In this case, the coherent SNR significantly differs from the ideal prediction of Eq. (13-14), and increasing the duration T (with or without using amplitude clipping) or the number of sources N may not then be useful to efficiently improve the coherent SNR after a certain point.

CHAPTER 3

BROADBAND PERFORMANCE OF THE DIFFUSE FIELD INTERFEROMETRY TECHNIQUE

3.1 Presentation of the experiments

Experiments were conducted on an aluminum plate of thickness 2mm (Fig. 4.a), similar to the one in aircraft fuselage and wing panels to demonstrate the potential of the DFI technique for remote monitoring of structural hot-spots. Cutting the plate edges irregularly enhances the generation of diffuse field through multiple scattering and reflections from the plate's edges and other discontinuities [Weaver 1986; Evans and Cawley 1999]. A practical issue in the implementation of DFI resides in the spatial distribution of the secondary ultrasonic sources in order to generate a fully diffuse field in the plate. To investigate these diffuse field requirements, a parametric study of the DFI technique can be conducted for a given pair of sensors at location $\boldsymbol{r_1}$ and $\boldsymbol{r_2}$ by varying the spatial distribution of N uncorrelated elastic sources located at $\boldsymbol{r_{s,j}}$ ($j=1..N$). This approach is not very practical for large values N since it involves either using a large number of sources or repeating the experiment several times by moving a single source. Instead, by swapping the role of source and receiver based on elastic reciprocity [Aachenbach 1993], experimental parametric studies of the DFI were conducted by 1) scanning the plate with a Laser Doppler Vibrometer to record the signals generated by two separated sources, now located at $\boldsymbol{r_1}$ and $\boldsymbol{r_2}$, over the distributed sensing locations $\boldsymbol{r_{s,j}}$ (j=1..N) (see Fig. 4) and 2) summing the cross-correlations contributions according to Eq. (5-7). This reciprocal implementation of the DFI allows simply varying the number and location of reciprocal sources.

To this end, two piezoelectric (PZT) ceramic actuators disks (Steminc mod. SMD15T09F2275S) [Giurgiutiu 2007] were mounted 15.6cm apart on the plate at two arbitrary locations (plate dimensions 18cm*16.5cm). Each actuator was driven by a wave generator (Agilent mod. 33220A – 20Mhz Functions) sending sinusoidal bursts of frequency 50kHz of amplitude 1V and of width 20µs**.** These piezoelectric actuators provide shot-to-shot repeatability and are commonly used for SHM applications. A Scanning Laser Doppler Vibrometer (SLDV) [Polytec PI, Model PSV400M2] allowing sampling to 1MHz, was used to record the reverberant wavefield over a fixed grid of 624 points (see Fig. 4.b). The sampling frequency of the recorded signals was 2.5MHz and the total recorded signal duration was 12.8ms.

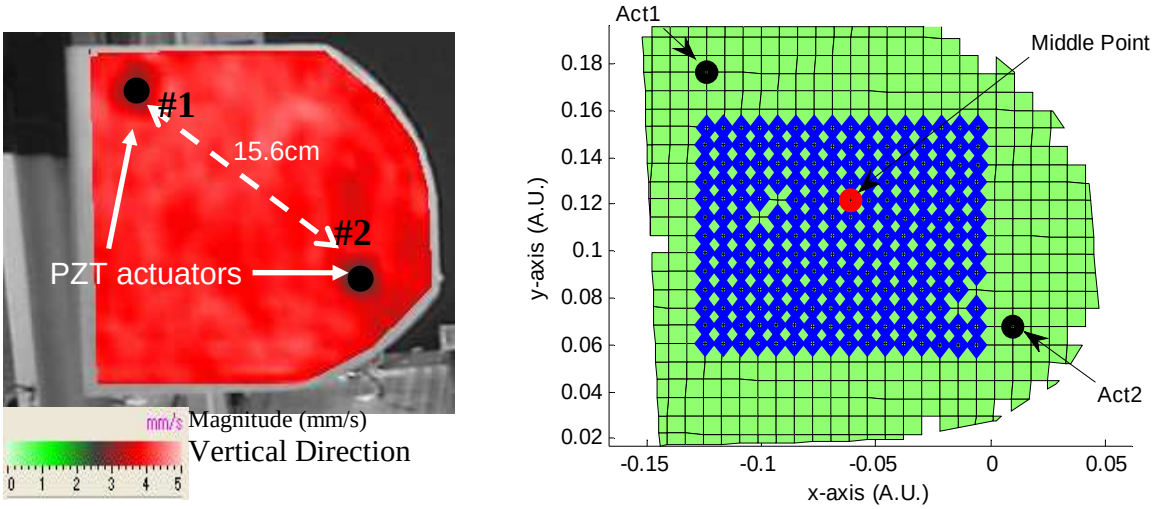

(a) (b)

FIGURE 4.a: 2mm-thick aluminum plate subjected to piezoelectric devices excitations at location #1 first, then at location #2. The color scale indicates the measured small variations of the average rms velocity over the plate. **4.b:** Measurement grid of the SLDV (624 points). The square pixel size is 0.6 cm. The locations of the two actuators as well as the grid point equidistant from the sensors (middle point) are also indicated. The blue dots represent the area of the central scanning grid used for the diffuse field analysis (see 3.2.2).

Figure 5.a illustrates the waveforms collected by the SLDV following a piezoelectric pulse sent by the first actuator at the actuator 1 (Act1) in solid red line and at actuator 2 (Act2) in dotted blue line reported in function of time. There is a delay between the two

signals, which represents the traveling time of a wave from Act1 to Act2. There is also a difference of amplitude between the first arrivals due to some damping happening in the plate. The waveforms show also a long "coda" caused by the multiple reflections on the edges. Their FFT is shown in Fig. 5.b and are composed of three main bandwidths due to the circular shape of the piezoelectric: B=[4-90]kHz, B_2=[90-186]kHz and B_3=[186-440]kHz. B concentrates almost all the energy.

The SLDV is mainly sensitive to the out-of-plane displacements of the plate dominated here by the A_0 guided wave modes given the thin plate geometry and the use of PZT actuators. Furthermore, due to the limited bandwidth and geometry of the PZT actuators, the energy spectrum extends in the frequency band B=[4-90]kHz (see Fig. 5.b), with most signal energy concentrated around 40-50kHz. Finally, as it is a narrowband signal, no significant frequency dispersion was observed for the A_0 mode arrival for the recorded signals (see Fig .14).

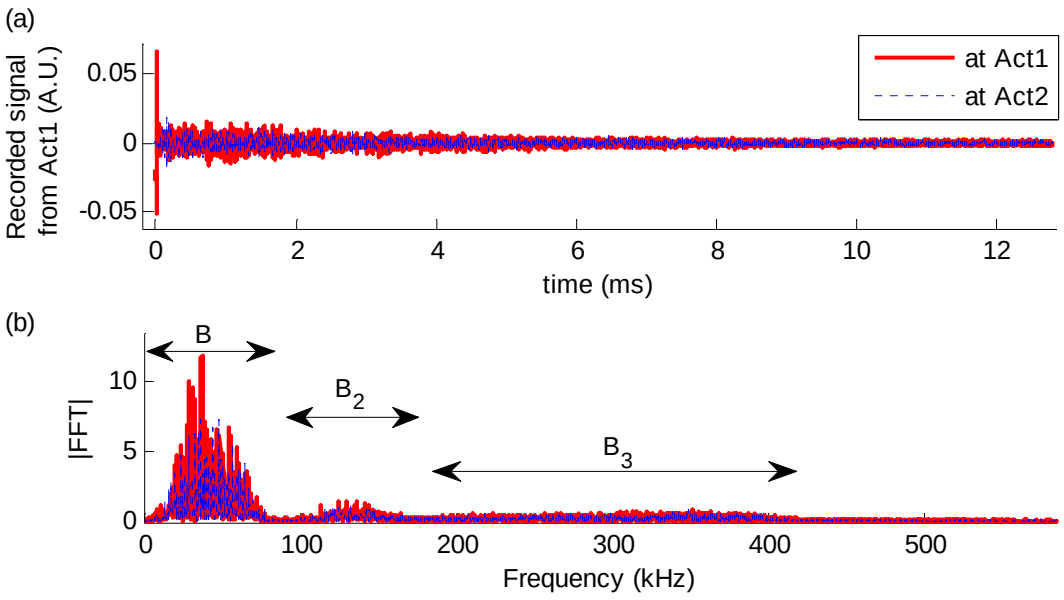

FIGURE 5.a: Waveforms collected by the SLDV following a piezoelectric pulse sent by the first actuator at Act1 (solid) and at Act2 (dot) reported in function of time. **5.b:** FFT of the recorded signals.

3.2 Experimental results

3.2.1 Elimination of erroneous recorded signals

In order to improve the overall signal-to-noise ratio *SNR*, the signals with high incoherent noise level (NL) were dismissed. The incoherent noise level also called electronic noise was estimated from the standard deviation during the last .4ms of the tail of each recorded signal after filtering in the main bandwidth *B*=[4-90]kHz (see Fig. 6.a). Usually the electric noise is measured on the pre-trigger signal but in our case we did not dispose of pre-trigger recordings. Then, the signals with a noise level ($NL(i)$ i=1..624) higher than three times the averaged value of all these 624 noise level estimates ($NL(i) < 3*(\frac{1}{N}\sum_{i=1}^{N} NL(i))$, N=624 and i=1..N) were considered as bad signal and thus did not participate in the estimation of the cross-correlation. 11 points have been dismissed using this method. Moreover the FFT of each signal has to contain the three main lobes shown in Fig. 5.b; those that didn't, were also dismissed: there were 3. So from this point, all the calculation will be done on these 610 remaining points and not on the 624 initial ones (see Fig. 6.b).

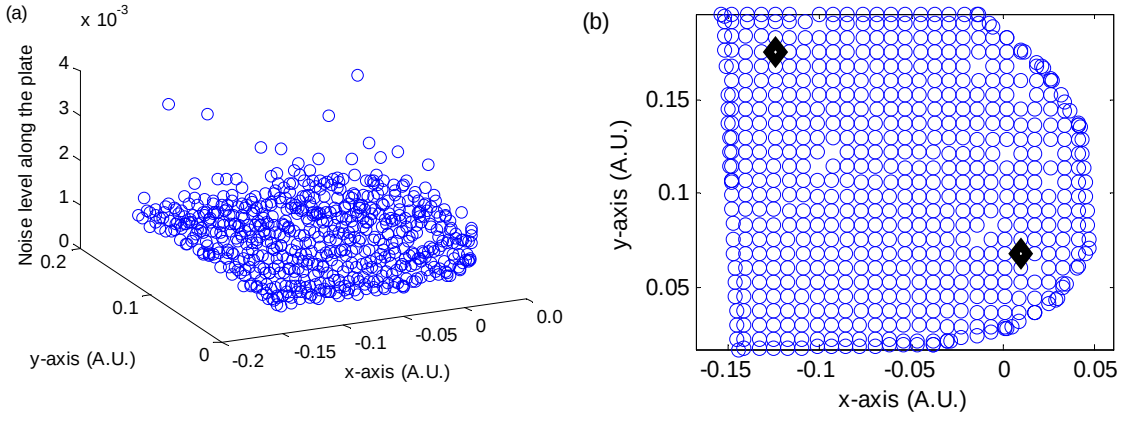

FIGURE 6.a: Noise Level $NL(i)$ along the plate before elimination when the Act2 is active. **6.b:** Location of the erroneous points on the plate (holes). Black diamonds are the locations of Act1 and Act2.

3.2.2 Diffuse field analysis

The spatial and temporal variations of the elastic energy distribution in the plate were investigated in order to determine the overall onset of the diffuse field regime using the SLDV measurements. The energy equipartition of the diffuse field is a necessary and sufficient condition to extract the full Green's function from the coherent output of the DFI [Weaver and Lobkis 2004; Paul et al. 2005; Langley 2007]. Formal equipartition means that in phase space the available energy is equally distributed in fixed average amounts among all the possible “states” (e.g. normal modes or incidence angle at the receiver) of the structure [Weaver 1982; 1984]. In the context of this study, energy equipartition should occur among the different guided wave modes supported by the structure which are primarily the lowest order modes S_0 and A_0 given the thin plate geometry and low frequency excitations [Akolzin and Weaver 2004]. Previous studies have shown that a diffuse field can be generated within a few tens wave transits across a regular thin plate [Evans and Cawley 1999].

The decay time τ_D of the elastic energy for the recorded reverberant wavefield was determined by fitting the exponential decaying model (see Eq. (11)) to the smoothed envelopes of the measured signals. The fitting procedure was only performed in the central portion of the signals, for 3.3ms<t<10.6ms in order to exclude the ballistic and singly scattered portion of the signal. The last 2.2ms of the recorded signals were excluded from the analysis since they appeared to be dominated by incoherent measurement noise (see Fig. 5.a). Figure 7 displays the smoothed envelopes of the signals recorded on the middle point between the two actuators (see Fig. 4.b), when either actuator #1 or #2 were activated. The slight difference between these two envelopes, even

at late times, results from the experimental differences inherent to these simple PZT actuators (actuator size, mounting conditions, and transducer response). Figure 7 also shows the best fit model, based on Eq. (11), of the recorded signal's envelope averaged over all SLDV sensing locations when either actuator is activated. This fitting procedure yields very similar estimates for τ_D of 4.7ms and 5ms respectively for actuator #1 and #2. Based, on the estimated velocity of the A_0 mode (around 1000m/s, see section 3.2.4.2), the decay time corresponds to an effective travel distance for the scattered waves of $D \approx 5$m, i.e. over 30 reflections across the dimensions of the plate which is in quantitative agreement with previous studies [Evans and Cawley 1999].

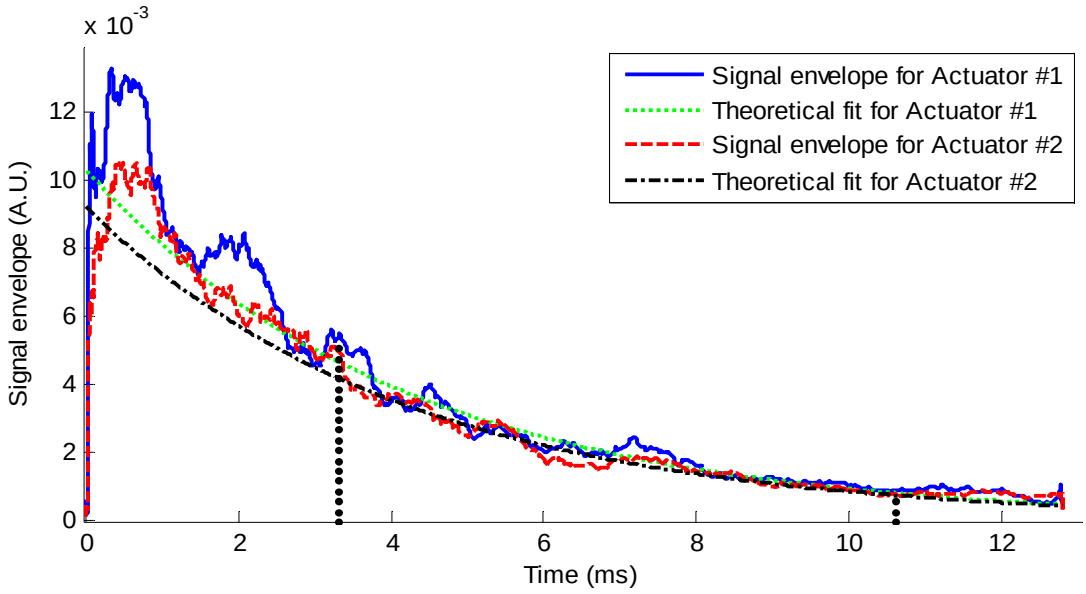

FIGURE 7: Smoothed envelopes of the signals filtered in *B* and exponential fit of the signal for the two cases (act #1 and act #2 active one at a time) at the point #261, middle point between the two actuators. The two vertical lines is the interval [3.3 - 10.6] ms on which the fit had been calculated.

As stated in the introduction, a uniform spatial distribution of the elastic energy is a consequence of the existence of energy equipartition in the plate. Figure 4.a qualitatively shows that the rms velocity of each recorded reverberant wavefield (see Fig. 5.a) across the SLDV scanning region is uniform, as a result of the wavefield randomization induced

by the irregular geometry of the plate. The spatial fluctuations of the elastic energy over the plate were measured in more details in order to further investigate the onset of the diffuse field regime. Furthermore, in order to avoid any artefacts due to proximity of the plate edges and corners, the spatial variations of the elastic energy were only measured in the central section of the SLDV measurement grid (see 204 points blue dots on Fig. 4.b) while actuator #1 was exciting the plate and the signals were filtered in the band B=[4-90]kHz. To do so, the smoothed time-varying envelopes (similar to the ones displayed in Fig. 7) of the recorded signals at these 204 central locations were divided into 35 successive time-intervals of equal duration 0.37ms. For each interval, the amount of energy fluctuations across the plate was estimated from the spatial variations of the mean value of the signal envelope (i.e. square root of the signal energy) in each interval. Figure 8 displays the spatial fluctuations of the mean envelope value across the 204 points on the 1^{st} time interval ($0<t<0.37$ ms), which includes the ballistic arrival, and the 25^{th} time interval ($8.8ms<t<9.17ms$) which corresponds to late coda arrivals. Note the different vertical scaling on each plot to enhance the visualization of the much weaker amplitudes of the late arrivals in Fig. 8.b. These results illustrate, as expected, that the averaged mean energy is more uniformly distributed over the plate at later time (multiply scattered waves), when compared to first interval where the spatial anisotropy of the energy is due to energy flux emanating from the first actuator which is mounted on the right hand side of the plate.

Similar results were found when using the other actuator #2. Hence the diffuse field regime is more likely to occur during the late coda of the recorded signals which is composed of multiply scattered waves.

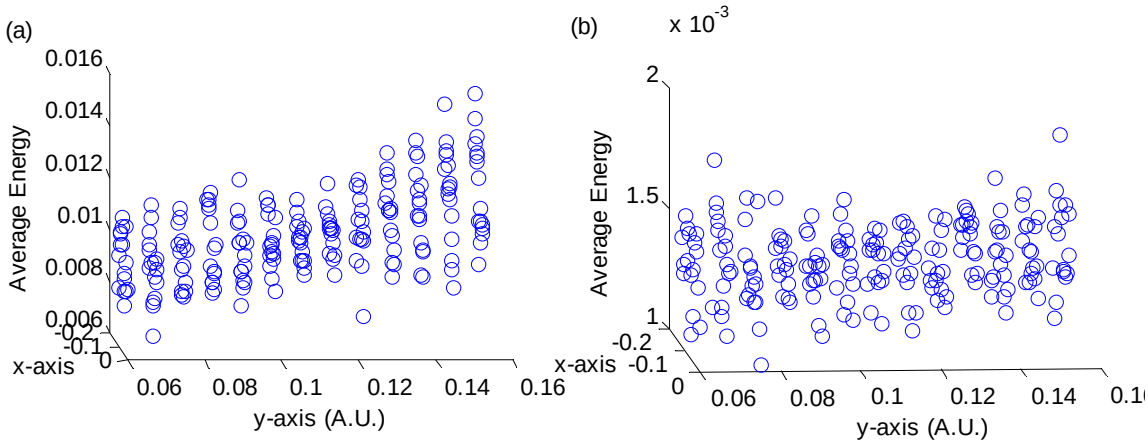

FIGURE 8: Average energy (mean values) of the envelopes of the filtered signals generated by Act1 over the 204 selected points located in the centre of the plate during both intervals: **8.a:** T_1=[0 – 0.37] ms and **8.b:** T_{25}=[8.8 – 9.1]ms.

Figure 9 displays the evolution, for increasing recording time, of the relative temporal fluctuations of the mean envelope value computed in each of the 35 successive time-intervals of equal duration 0.37ms. The relative temporal energy fluctuations were computed from the ratio of the standard deviation to the mean value of the averaged energy values obtained at each of the 204 points locations over the whole plate area for each time interval (e.g. as displayed in Fig. 8). After the first initial 1.5ms of the recordings, the temporal fluctuations of the averaged envelope level remain on the order of 10%. The increase in fluctuations at late time (t>12ms) is an artifact due to the high variance of the incoherent measurement noise which actually dominates the recorded signals in the late coda (see Fig. 5.a).

Overall, the results displayed in Fig. 7-9 indicate that the selected thin plate with random geometry appears to rapidly randomize the propagating elastic energy which rapidly exhibits characteristic features of a diffuse field regime. Hence this thin plate appears as a relevant test structure to assess the performance of the DFI technique

between location #1 and #2 using the implementation based on spatial reciprocity as discussed in the section 3.1.

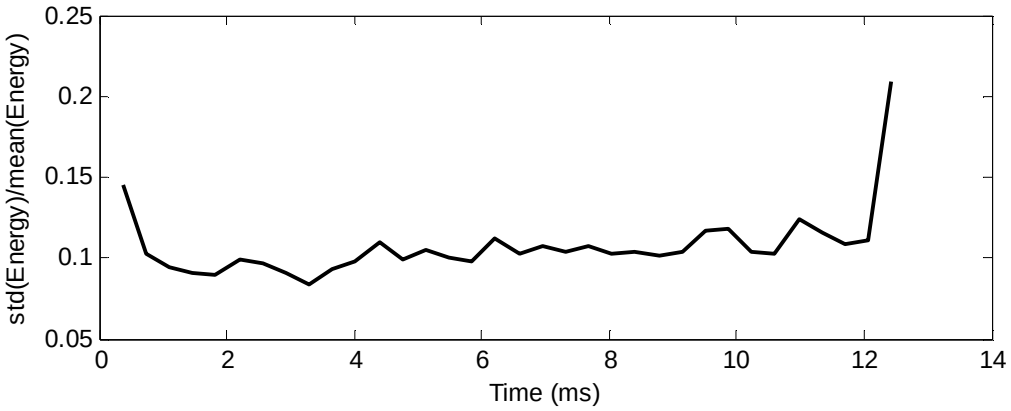

FIGURE 9: Temporal evolution, for increasing recording time, of the relative spatial fluctuations of the elastic energy in the central region of the plate. At each measurement location, the elastic energy was estimated from the mean envelope value of the time-windowed recorded wavefield for each of the selected 35 successive time-intervals (see Fig. 8).

Now that we are sure to dispose of a diffuse noise field, the cross-correlation of the two signals can be done. Different improvements of the correlation (filtering, clipping) have been studied in order to improve the results. The next sections will present the results.

3.2.3 Estimate of the Green's function

3.2.3.1 Cross-correlation (CC) of the two signals measured at every 610 points

The signals were filtered in *B*=[4-90]kHz, and then cross-correlated at each single point ($C_{12}^{j}(t)$) using the command *"xcorr"* in Matlab (see Eq. (1)). The summation of all the cross-correlations had been done in a random order to have the most general solution (see Eq. (6)). This specific random order had been used each time that the evaluation of the cross-correlation was needed in order to allow comparison between the different cases

studied in the following subsections.

To compensate for possible signal clipping at its maximums, each cross-correlation was reevaluated on a 10 times more precise scale (Ts_{new}=Ts/10=39.063ns), using the *"spline"* function in Matlab. Figure 10 illustrates this final cross-correlation ($C_{12}(t)$) with a distinct first arrival, where the energy is mainly concentrated, and also part of the later reflections.

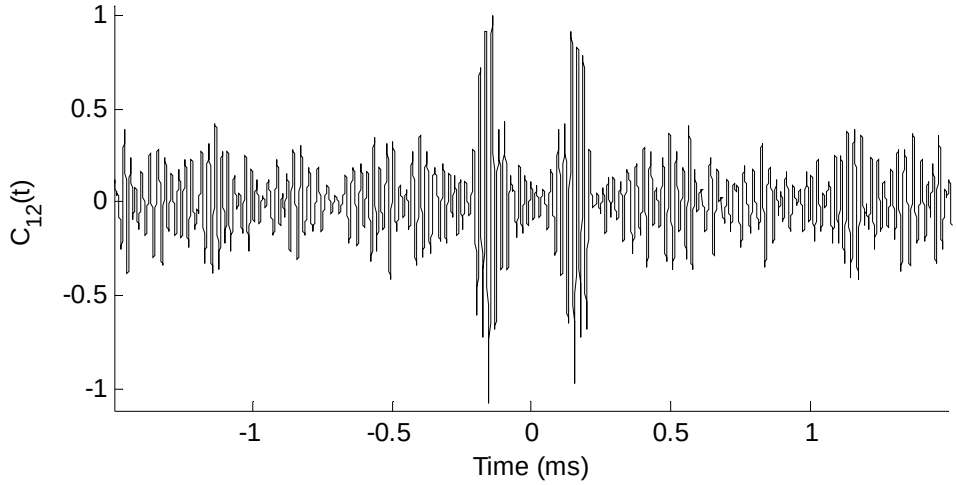

FIGURE 10: Cross-correlation ($C_{12}(t)$) of the two signals recorded by the SLDV when Act1 and Act2 were active at the 610 points on a scale [-1.5 1.5]ms.

3.2.3.2 Estimate of the true Green's function (GF)

Section 2.1 explained the theoretical method to access to the Green's function especially through Eq. (4). Thus, the estimate of the GF had been evaluated by taking the derivative with respect to time of the cross-correlation (see Fig.10) and the result is shown in Fig. 11.

$\frac{dC_{12}(t)}{dt}$ is not exactly equal to the GF but proportional to the sum of the reciprocal and the anti-reciprocal Green's function (See Eq. (4)). This result seems satisfactory, as the first arrival clearly dominates the later reflections.

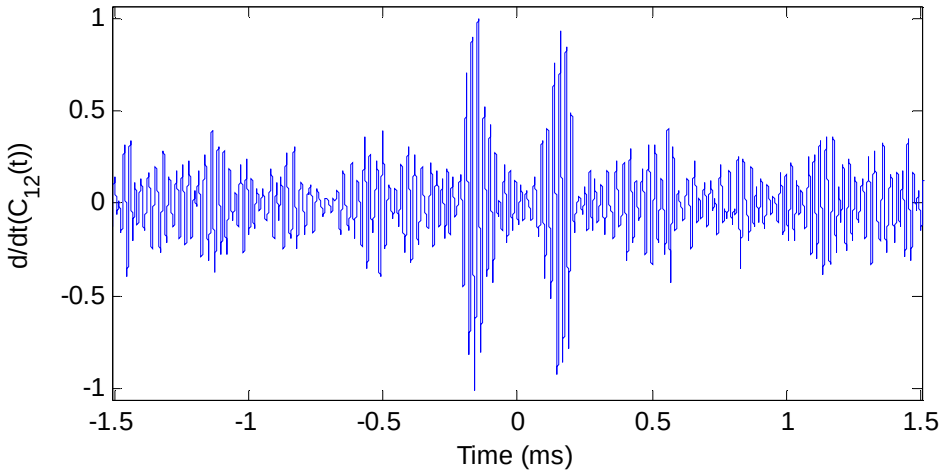

FIGURE 11: Estimate of the true Green's function by taking the derivative with respect to time of the cross-correlation ($\frac{dC_{12}(t)}{dt}$) over the 610 points on a time scale of [-1.5 1.5]ms.

Also, this estimate of the GF can be considered as being symmetric in time, required criterion by the theory in a fully diffuse field. Table 1 sums up the study of the symmetry of $\frac{dC_{12}(t)}{dt}$.

TABLE 1: Comparison of the maximums on the negative and positive time of $\frac{d}{dt}C_{12}(t)$ and on the positive side of its symmetric. Their corresponding A_0 mode arrival times are also given.

	For negative time	**For positive time**	**For symmetric CC**
t_{max} (s)	-1.4770e-4	1.4789e -4	1.4781e-4
Max (A.U.)	0.5257	0.4866	0.5060

The positive time of the maximum represents the time that a wave takes to propagate from Act1 to Act2, and the negative time is the time taken from Act2 to Act1. Thus the symmetry is needed. The table shows that between the corresponding times of the maximums on the negative and positive sides of the GF there is 0.2 μs of difference (less than one recording step of time Ts) which is very good. And the difference with the time of the maximum on the symmetric of the GF (see Fig. 12) is ~0.1 μs. So the symmetry in

time of the GF can be admitted, especially when the exact similarity of the two actuators have not been proven. Furthermore, the error between the amplitude of the two maximums is around 8.0% which is also a good result.

The symmetric part of the total estimate of the GF, i.e. the mean contribution of the amplitude obtained for both positive and negative time-delays is compared to the estimate of the GF in the Fig. 12. The two estimates of the GF are mainly in phase along the time unless around zero where there is mainly only electrical noise.

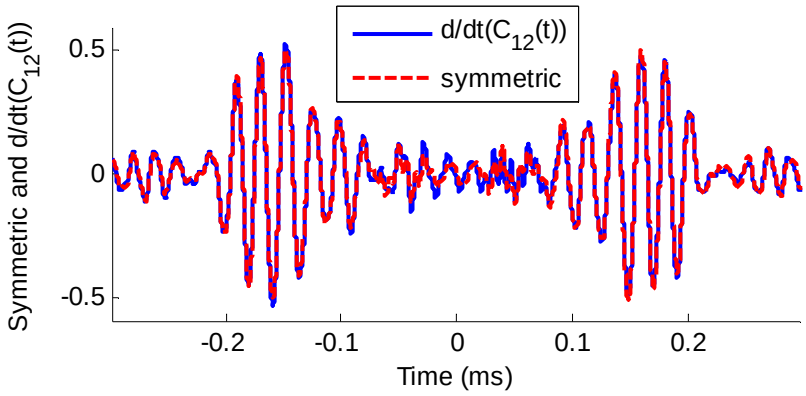

FIGURE 12: Comparison of $\frac{d}{dt}C_{12}(t)$ (blue) and its symmetric (red) on the interval [-0.25 0.25]ms.

From this symmetric estimate of the GF the dispersion of the A_0 mode arrival can be computed using two different methods first a smooth-pseudo Wignerville and a scalogram. Both are based on the study: frequency vs. time. Therefore $\frac{d}{dt}C_{12}(t)$ vs. time and its FFT are shown in Fig.13. The FFT confirms the filtering applied to the signals in B=[4-90]kHz, and shows that the signals are mainly in the frequency bandwidth B_{main}=[40-50]kHz. Then Figure 14 illustrates the results of the two methods. As said earlier no significant frequency dispersion is observed for the A_0 mode arrival for the recorded signals filtered in B. Indeed around the arrival time of the A_0 mode: t_0=0.148 ms (see Table1), the signal is concentrated in the frequency bandwidth B_{main}, as agreed by the

two figures 14.a and b.

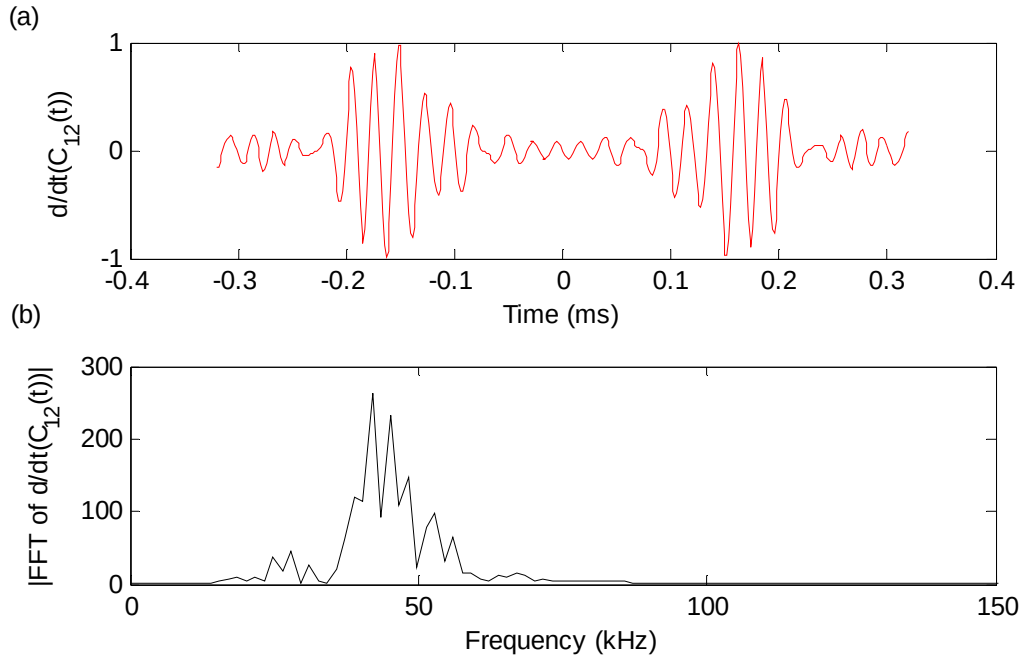

FIGURE 13.a: Symmetric of the estimate of the Green's function vs. time. **13.b:** Corresponding FFT.

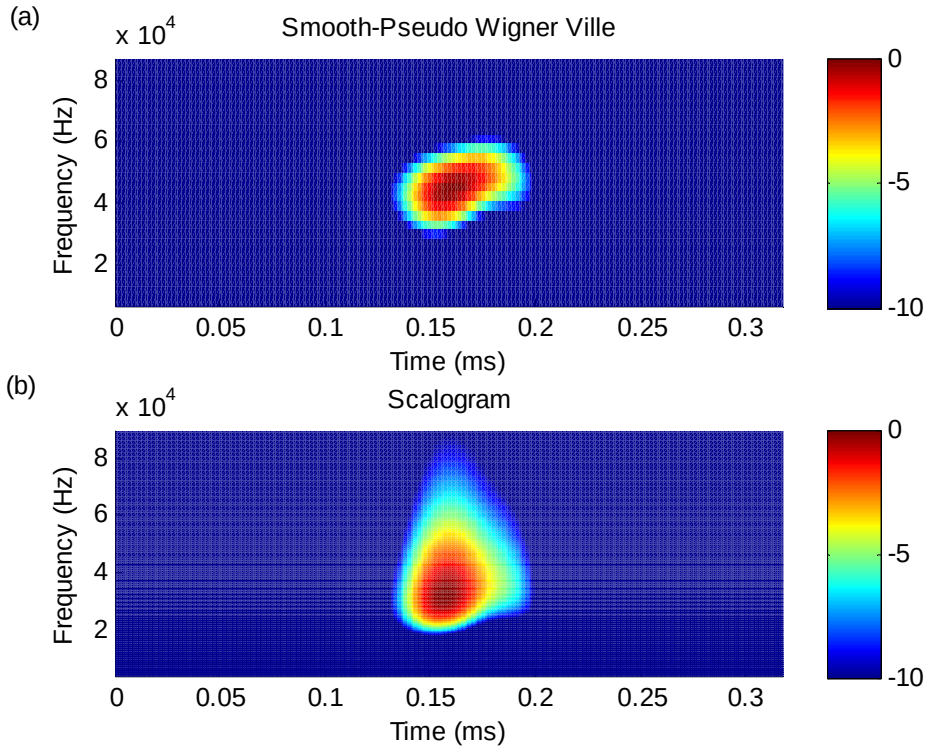

FIGURE 14.a: Smooth-pseudo Wignerville of $\frac{d}{dt}C_{12}(t)$. **14.b:** Scalogram of $\frac{d}{dt}C_{12}(t)$.

3.2.4 Performance study of the Diffuse Field Interferometry (DFI) technique

3.2.4.1 Influence of clipping level of the reverberant waveforms

To better understand the information contained in the diffuse field portion of the signal, a study of its impact on the Green's function calculation was done. The signals filtered in *B*=[4-90]kHz were further processed using an amplitude clipping procedure to assign uniform weights to the multiple reverberations in order to improve the apparent contribution of the late coda (tail of the signal) of the diffuse field records [Sabra et al. 2008; Larose et al. 2004] (see section 2.3). Three different threshold levels were studied: no threshold, 5 and 15 times the standard deviation of the ambient noise level (5NL and 15NL) calculated on the last .4ms of the signals (see subsection 3.2.1). The clipped signals in both cases (5NL and 15NL) have the same time length: the first 4.3ms of the original waveform, corresponding to the length of the signals clipped at 15NL. The processed waveforms are shown in Fig. 15.a, and the clipping effects are easily noticeable in term of change of amplitude (5NL dashed line, 15NL dotted line).

The estimate of the Green's function, illustrated in Fig. 15.b, was evaluated for each case following the steps developed in the previous section after summing over the contributions of all 610 points of the scanning grid. The first observation, coming from Fig. 15.b, is that the computed estimates of the GF are similar for the three different processing schemes, so the estimate of the GF does not depend much on the processing, at least for the early A_0 arrival. Thus the DFI process is robust with respect to applying various clipping level. As expected, Fig. 15.b shows the first arrival distinct from the following reflections. A second result is the symmetry of the cross-correlation in function of time, satisfying the theoretical prediction in a fully diffuse field. As in the previous

section, the symmetry had been proven with a difference between the positive and negative times of the A_0 mode less than 2 steps of well-defined time (Ts_{new}) which correspond to <0.1 µs. Hence, the first high-amplitude symmetric arrival provides a reliable estimate of the A_0 mode contribution of the local Green's function between the locations #1 and #2 (see Fig. 4).

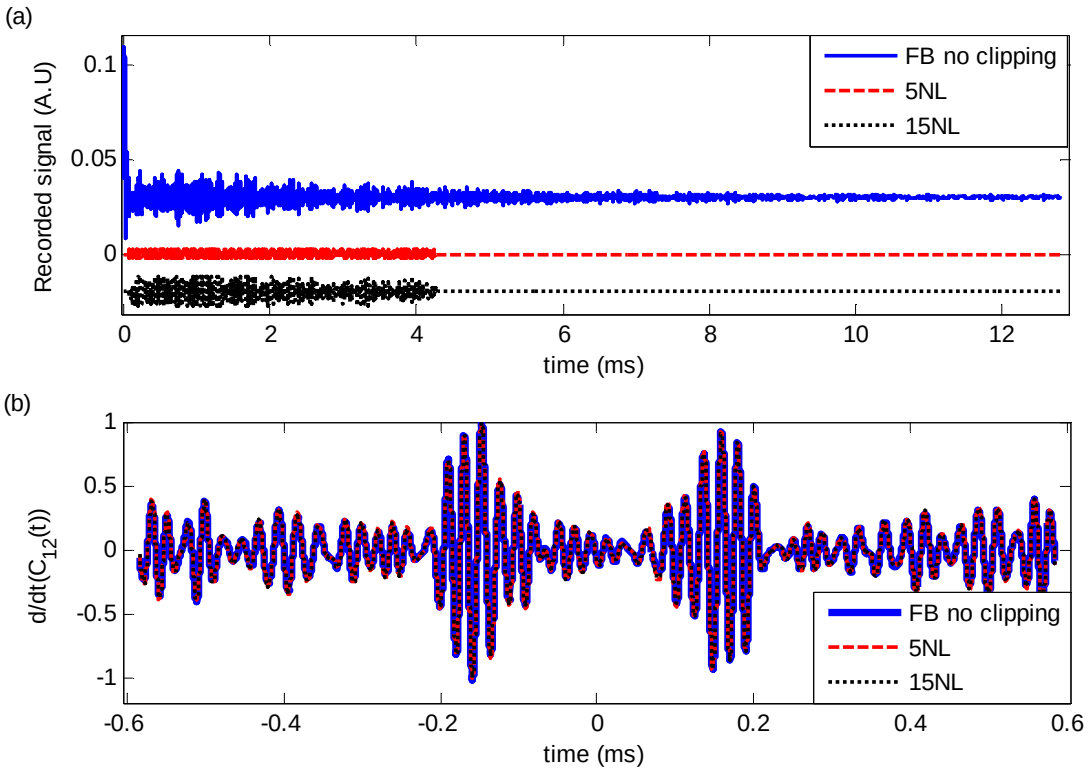

FIGURE 15.a: Recorded signal at Act1 when Act1 was active filtered in *B*=[4-90] kHz. The second and third ones have been clipped respectively at 5 and 15 times the electronic noise level over the same time-window of length 4.3ms. **15.b:** Normalized estimate of the Green's function of the 610 points added in a specific random order in the three cases (see 3.2.3.1).

Furthermore, as stated in Section 2.3, this amplitude clipping procedure is sensitive to the amount of incoherent measurement noise present in the recorded waveforms, and can potentially degrade the performance of DFI at low recorded SNR_r (see Eq. (13)). Thus, the influence of clipping threshold of the reverberant waveforms on the DFI performance was investigated by measuring the obtained coherent $SNR(t)$.

High coherent *SNR* of the A_0 mode arrivals (t_0=148μs) were measured for the three waveforms (no clipping, 5NL and 15NL) for N=610 as respective level: 71, 73 and 75 using Eq. (6-8) (i.e. ~36dB). To evaluate the coherent *SNR*, both Eq. (6) and (7) were first computed over a time-window T_0=[-0.234 0.234]ms containing the first arrival only. Then in order to minimize the effect of local temporal fluctuations around t_0, the local variance $V_{12}(t)$ (see Eq. (7)) was approximated by its mean value on the interval t=[70-223]μs centered on t_0. Then Eq. (8) was evaluated at t_0 for each contribution of the secondary sources *N*.

The process just described had been used to evaluate the variations of the coherent $SNR(t)$ in function of the clipping level as shown in Fig. 16. The waveforms were filtered in *B* and then clipped at different level from 5NL to 70NL, using two different recording durations: *T*=4.3ms (solid line) or *T*=6ms (dash line). The chosen lengths of the signals both correspond to a certain clipping level: 15NL and 9.84NL respectively. The *SNR* were evaluated from the symmetric of the estimate of the GF for which only the contributions of the first 200 measured points of the specific random order cited earlier had been taking into account. High clipping level (e.g 70*NL*) barely modifies the initial reverberant waveform while low clipping level (e.g. 5*NL*) removes all visual appearance of the ballistic arrival and exponential decay, as shown qualitatively on Fig. 15.a.

The experimental curves displayed on Fig. 16 indicate that lower clipping improves the coherent *SNR* up to a maximum obtained around 15NL approximately for both selected recording duration *T*. Beyond this value, any additional clipping increase the contribution of incoherent measurement noise on the measurement which lowers the

effective recorded SNR_r and thus, in turn, the measured coherent SNR decreases as expected from theoretical predictions (see Eq. (9-10)).

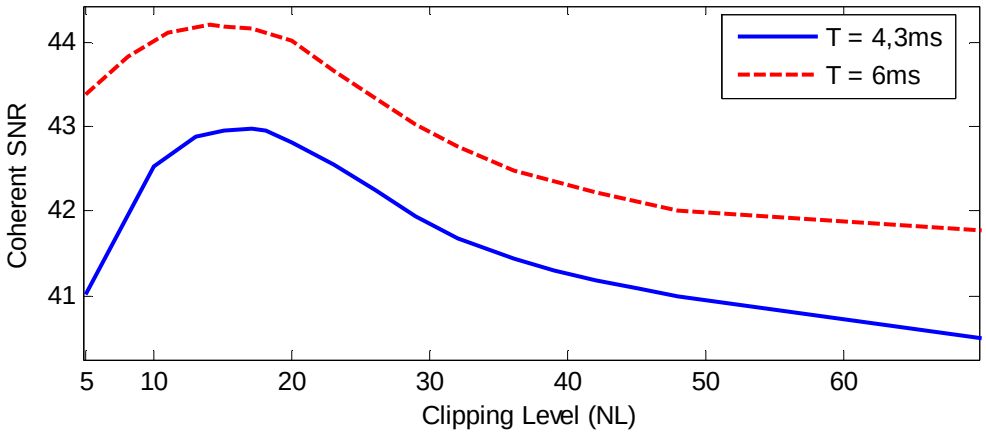

FIGURE 16: Variations of the coherent *SNR* of the correlation waveform (linear scale) for increasing clipping level applied to the different recording duration of the reverberant waveforms T=4.3ms (solid line) or T=6ms (dash line).

3.2.4.2 Influence of the number of secondary sources *N*

The influence of the number of sources *N* on the DFI performances is studied in this section. The coherent *SNR* of the A_0 arrival is evaluated as explained in the previous section for the three cases from Fig. 15 (no clipping, 5NL and 15NL on recording duration *T*=4.3ms). This definition of the *SNR* provides the contribution of each source in the cross-correlation and will help minimizing the number of sources required. In agreement with previous studies [Snieder 2004; Sabra et al. 2005b; weaver and Lobkis 2005; Larose et al. 2008], the *SNR* evolves as $\sqrt{N}$ regardless of the specific amplitude clipping threshold apply to the reverberant waveforms (Fig. 17, linear scale). This study showed that the first arrival contained good signal growing as N with the fluctuation in this portion growing as $\sqrt{N}$. Furthermore, results of Fig. 17 also demonstrate the improvement of coherent *SNR* when using a moderate clipping level (15NL, dotted line) with respect to no clipping at all (plain line), while very low clipping level (5NL, dashed

line) improves only slightly the coherent *SNR*. For example to reach a *SNR* level of 60 (i.e. 35dB), the number of sources increases from respectively 384 for a clipping threshold of 15NL to 410 for a clipping threshold of 5NL and 428 if no clipping is applied to the recorded waveforms.

The clipping procedure thus allows the diminution of the number of secondary sources by almost 50. However the lower the SNR level is, the less difference there is between the three cases.

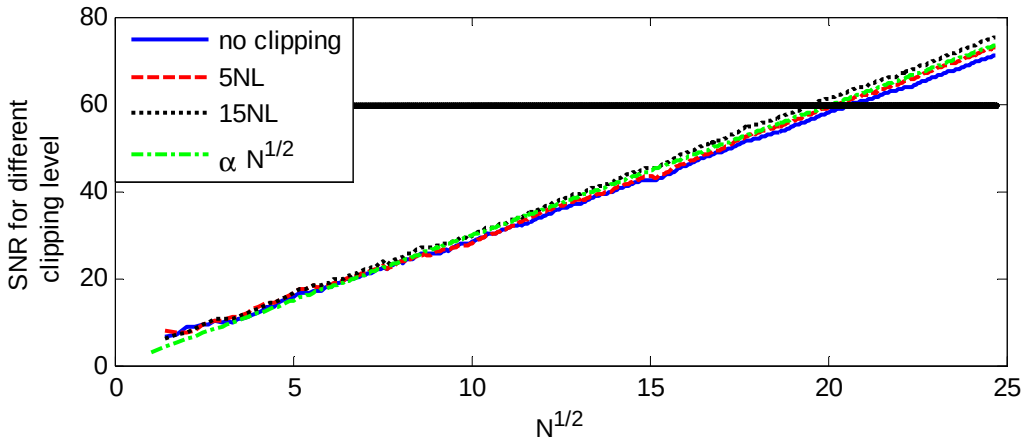

FIGURE 17: *SNR* in *B* using the definition given by Eq. (6-8) for the three cases of thresholding from the previous part vs. $\sqrt{N}$. The theoretical result is given in green, and confirms the growth in $\sqrt{N}$.

In SHM, the precision of the phase and group velocity measurements obtained from DFI for a given set of *N* secondary sources is another important criterion to estimate the performance and robustness of the DFI technique. It is thus studied in this subsection, in addition to the usual coherent *SNR* metric. For a given value of *N*, the phase (resp. group) velocity was computed respectively based on the arrival times of the first maximum of the symmetric of the derivative with respect to time of the cross-correlation waveform (t_0 =0.148ms for *N*=610) (resp. envelope (t_0^{env} =0.153ms for *N*=610)) and given the knowledge of the separation distance *D*=15.6cm between the two actuators. The

asymptotic estimate of the phase (resp. group) velocity obtained for the largest number N=610 points, and hence best reconstructed waveforms (see Fig. 15.b), was estimated as C_p=1057m/s^{-1} (resp. C_g=1020m/s^{-1}), which is in good agreement with predicted valued for the A_0 mode (wavelength $\lambda \approx 1$cm) in aluminum samples [Achenbach, 1993]. The relative variation of these arrival times t_0, with respect to the asymptotic values used to compute C_p and C_g, computed for each contribution of the secondary sources N are shown respectively in Fig. 18.a and .b for the three previous cases (5NL, 15NL clipping or no clipping).

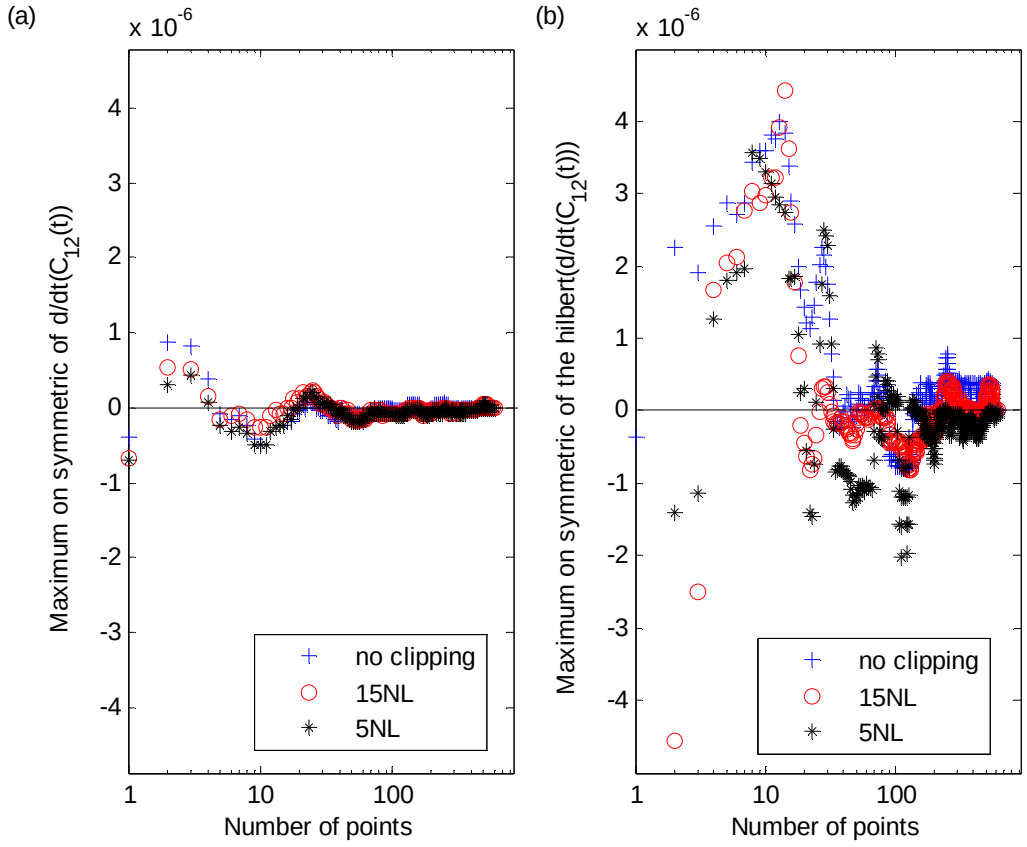

FIGURE 18.a: Evolution of the time of the maximums of the symmetric of the Green's function for the three cases in B in function of the number of sources ($\log_{10}$ (N)). **18.b:** Evolution of the time of the maximums of the symmetric of the envelope of the Green's function for the three cases in function of the number of sources ($\log_{10}(N)$). For each curve, the final time had been centered on zero.

The decision to perform the study on the symmetric function had been made in order

to have the most general and accurate result. A logarithmic scale was used for the horizontal axis in order to enhance the visualization of the variations for small values of the parameter *N*. Note that the vertical scale is the same for both and thus the variations are more than 10 times higher in the group velocity measurements than in the phase ones. This is even truer that to minimize the variation between consecutive times the *"smooth"* function in Matlab had been used in the group velocity measurement shown in Fig. 18.b. As a consequence, the error in measured arrival times becomes very small (<0.5 μs ($13*Ts_{new}$)) after *N*=25 (resp. *N*=205) for phase (group) velocity measurements. Hence, at this point, the obtained cross-correlation waveforms from DFI should yield reliable estimates of the phase and group velocity of the A_0 mode on this thin plate.

3.2.4.3 Influence of the location of the secondary sources

The effects of the spatial configuration and the number of the secondary ultrasonic sources on the DFI performance were then assessed in a practical SHM scenario where only 25 secondary sources would be used to remotely extract the coherent A_0 mode between locations #1 and #2 (indicated by diamond shapes on Fig. 19). The choice of 25 sources is made for practical reasons, none experiment will indeed allow having more than 30 sources.

To do so, 25 measurement points of the SLDV, acting as secondary sources in this reciprocal DFI implementation, were selected on the plate along three different patterns: surrounding the whole plate (Fig. 19.a), randomly located (Fig. 19.b) or aligned along the three top lines of the measurement grid (Fig. 19.c).

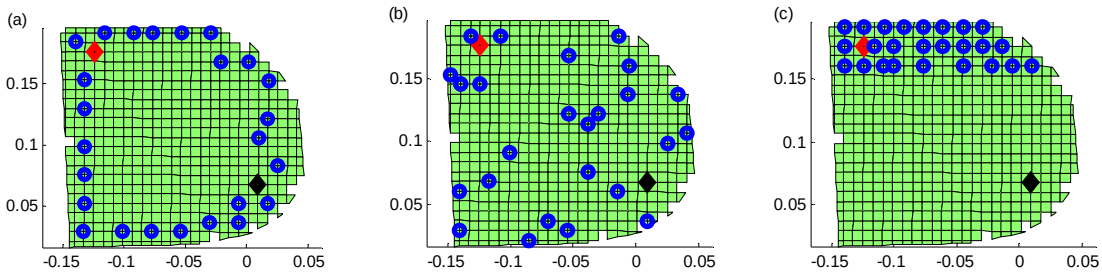

FIGURE 19: Geometric configurations of the selected N=25 measurement points (circle), acting as secondary sources for the reciprocal DFI implementation, **19.a:** all around the plate, **19.b:** randomly distributed, **19.c:** aligned along one side of the plate. The actuators' locations (see Fig. 4.a), acting as sensors' locations for the reciprocal DFI implementation, are indicated by diamond shapes

Using waveforms filtered in *B*=[4-90] kHz and clipped at 5NL, for each configuration the estimate of the GF was reconstructed and normalized. Figure 20 shows the superposition of these three previous estimated GF obtained from DFI.

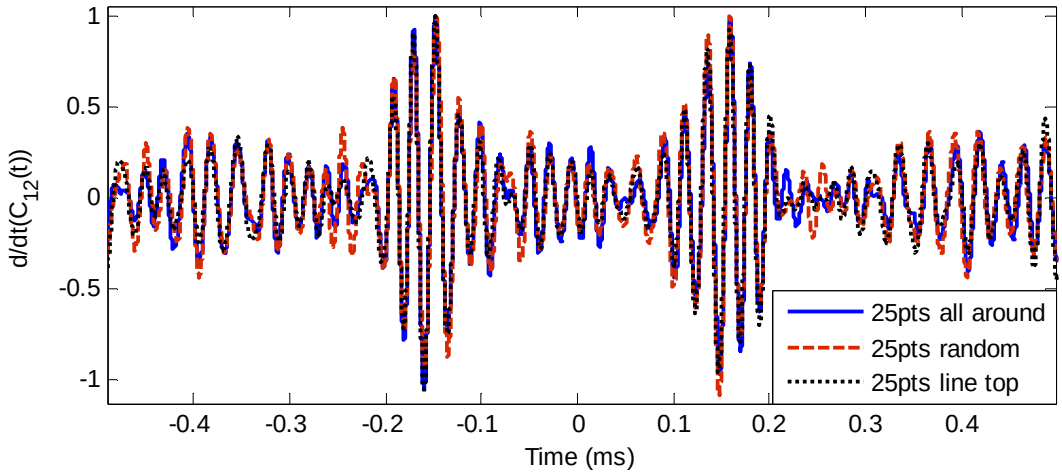

FIGURE 20: Superimpose normalized estimate of the Green's function obtained from DFI for the three configurations of secondary sources displayed in Fig. 19.

Visual evaluation once again reveals that the cross-correlation waveforms using these three different sources configurations are highly similar, especially during the first symmetric A_0 arrival (100µs<t<200µs). Indeed, when the measured A_0 arrival times for the three configuration are compared with the asymptotic value obtained using the whole 610pts measurement point (see Fig. 15.b and Fig. 18): $t_0^{610\,pts}$ = 0.14777 ms, the errors

made respectively in case a, b and c are: 0.08%, 0.1%, 0.18%. Even if, using sensors either all around or randomly on the plate leads to the smallest error in the estimation of t_0, the error made by putting them in the same area is also small. This result highlights the fact that, once the recorded (or processed) reverberant field of the structure approximates well a diffuse wavefield, the location of a small number of sensors on the plate does not drastically alter the performance of the DFI technique, as expected from previous numerical simulations [Larose et al. 2008]. And furthermore, it demonstrates that practical implementations of the DFI technique for SHM applications are feasible even using a small number of secondary sources.

In addition to these performance criteria, it will also be shown in the following subsection that relative measurements of the *SNR* for the direct waves vs. late arrivals of the cross-correlation waveforms obtained from DFI can be used to determine if those late arrivals are actually dominated by weak coherent coda arrivals (thus potentially usefully for SHM purposes) or by residual fluctuations instead (thus indicating that more spatial or temporal averaging is required). Therefore, a new definition of the *SNR* will be developed.

3.2.4.4 Emergence of coherent coda arrivals from DFI

Based on the previous discussion, a clear coherent A_0 arrival emerges from cross-correlation waveform when using a sufficient number of sources *N* (see Fig. 15.b, and Fig. 20). But, the computed cross-correlation waveform contains also multiple later arrivals for any given value of *N* (see Fig. 21.a). Hence a practical question for SHM

applications is to determine beyond which point these late arrivals correspond to actual coherent coda arrivals of Green's function vs. residual temporal fluctuations due to the imperfect convergence of the DFI process.

One simple way to distinguish between these two situations is to measure the variations of relative amplitude changes $R(N;T_l)$ of the coherent A_0 arrival amplitude with respect to the standard deviation of these late arrivals averaged over a given time interval T_l for increasing number of sources *N*, defined as:

$$R(N;T_l) = \frac{Max_t(\frac{d}{dt}C_{12}(t))}{std(\frac{d}{dt}C_{12}(t);t \in T_l)} \qquad \text{Eq. (17)}$$

where the cross-correlation waveform $C_{12}(t)$ computed using Eq. (6) for *N* randomly selected secondary sources. No amplitude clipping was applied to the recorded waveforms. This second definition is similar to the equation giving the *SNR* (Eq. 8), but instead of dividing the square root of the standard deviation of these late arrivals, it divides it directly. And since DFI is a coherent process, the amplitude of any coherent arrival (e.g. related to an actual arrival of the local Green's function) would grow linearly with *N*, while the amplitude of residual temporal fluctuations (e.g. due to incoherent noise) only grows as $\sqrt{N}$ [Weaver and Lobkis 2005; Sabra et al. 2005b; Larose et al. 2008]. Hence the ratio $R(N;T_l)$ theoretically grows as $\sqrt{N}$ as long as the arrivals in the window T_l are dominated by residual fluctuations, but then plateaus at a fixed value when coherent arrivals actually emerge in the selected time-window T_l. Figure 21.b displays the normalized variations of $R(N;T_l)$ vs. $\sqrt{N}$ for three successive time-

windows T_l selected from the reference cross-correlation waveforms (see Fig 21.a). The windows had been chosen one close (T_1=[0.58ms-1.8ms]), one in the middle (T_2=[3.2-4.3]ms) and one far (T_3=[10.2ms-11.4ms]) from the first A_0 mode arrival to have thus an overview of the waveform content in its whole. The normalized variations of the coherent $SNR(t)$ for increasing N in the case of no clipping (same as Fig. 17) are also indicated as a reference.

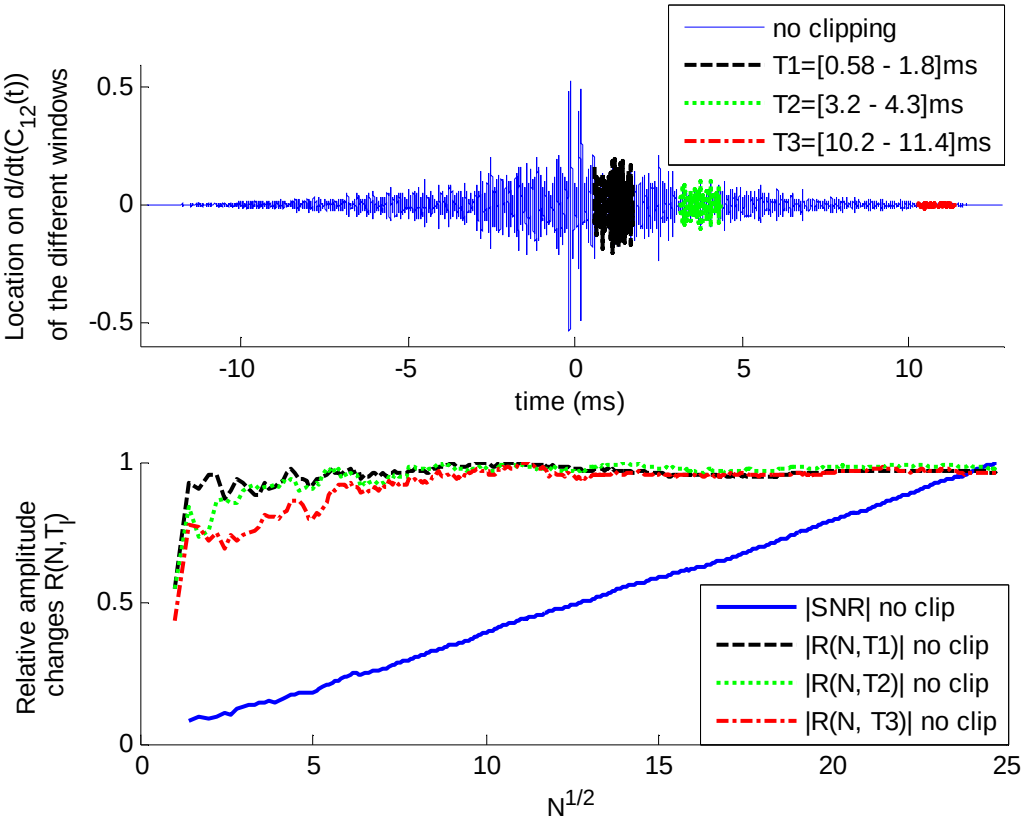

FIGURE 21.a: Location of the three selected time-windows: T_1=[0.58-1.8]ms, T_2=[3.2-4.3]ms, T_3=[10.2-11.4]ms, on the filtered d/dt(C_{12}(t)) obtained from N=610 secondary sources. **21.b:** Normalized variations of the ratio $R(N;T_l)$ (see Eq. (17)) for increasing values of $\sqrt{N}$ for the three time-windows shown in 21.a. The normalized variations of the coherent *SNR* are also indicated for comparison (blue solid line).

As expected the ratio $R(N;T_l)$ starts to plateau more rapidly for increasing N when the selected time-window T_l contains early coherent arrivals (dashed line, T_1) compared to a later time-window (dot-dashed line, T_2 or T_3). As expected, the emergence of the late

coherent arrivals is thus slower than for early coherent arrivals. For instance, the ratio $R(N;T_l)$ reaches 95% of the asymptotic plateau value after N=4 for the window T_1=[0.58ms-1.8ms], after N=28 for the window T_2=[3.2ms-4.3ms], and after N=73 for the window T_3=[10.2ms-11.4ms]. However, in practice, for sufficient number of sources N, even the late coda arrivals appear to be genuine coherent arrivals which could potentially be used for structural monitoring purposes (e.g. for passive coda wave interferometry).

The following part uses these results to go further in the analysis of the contribution of the diffuse field part of the signal in the improvement of the *SNR*.

3.2.4.5 Influence of the duration of the reverberant signal

After improving the *SNR* by playing on the clipping level, on the number and locations of the secondary sources *N*, it is known that using a longer duration *T* of the recorded waveforms allows the benefit from the multiple scattering effects (see Eq. (13-15)), and thus it is important to know the relation between the coherent *SNR* and the length of the signal.

The coherent $SNR(t)$ had then been experimentally measured for signals of increasing recording duration T_l varying on the same time interval than the one set by clipping at 15NL: *T*=[0.43-4.3]ms so the maximum recording duration is T_{max} = 3.87ms; and this, for the three different cases from the previous studies: no clipping, 5NL, and 15NL. The variation of the recording duration T_l is done almost continuously from *0* to T_{max} = 3.87ms with an increment of 40 μs. Figure 22 shows the recorded signal at Act2 when Act2 was active, filtered in *B* and clipped at 15NL on the full length of the time-

window T (solid line), and on a smaller time-window T_1=[0.43-1.8]ms (dashed line), which is only one example among the different time-windows measured.

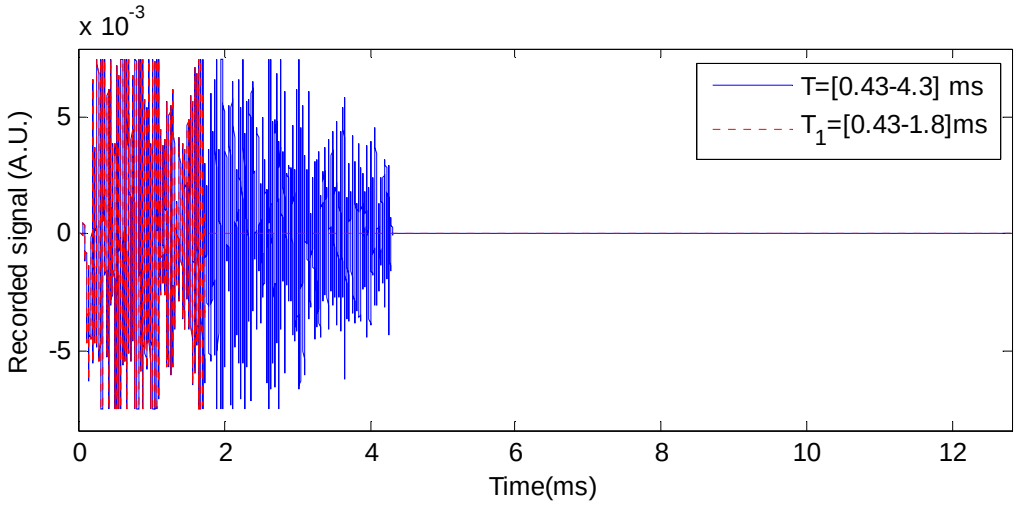

FIGURE 22: Recorded signal at Act2 when Act2 was active filtered in *B*=[4-90]kHz and clipped at 15NL. The time-window (red part) is one example among the time-windows on which the estimate of the GF had been evaluated. These time-windows start from 0.43ms to 4.3ms (blue part).

The cross-correlation and thus the coherent $SNR(t)$ were then evaluated for these three cases taking the contribution of different numbers of secondary sources *N*=25 (Fig. 23.a), *N*=100 (Fig. 23.b) and *N*=200 (Fig. 23.c). The coherent $SNR(t)$ measured at the A_0 arrival time t=0.148ms are displayed in Fig. 23 in function of the square-root normalized length of the signal: $\sqrt{T_l / T_{\max}}$.

These measured variations of *SNR*(*t*) appear to be very similar regardless of which pre-processing types (no clipping, 5NL or 15NL) or specific number of secondary sources *N* used (see Fig. 23 for *N*=25, *N*=100 or *N*=200). Moreover, for each number of secondary sources, the *SNRs* of the signals clipped at 15NL are, as expected, always the highest of the three experimental curves (see Fig. 16). And the differences in terms of *SNR* level reached by each curve increase with *N*, which is due to the contribution of each extra sources taking into account: when *N*=25 (see Fig. 23.a), the *SNR* obtained with no

clipping and 5NL reached the same level: 17, and when N=200 (see Fig. 23.c), SNR with no clipping reaches 39 and SNR after clipping at 5NL reaches 41.

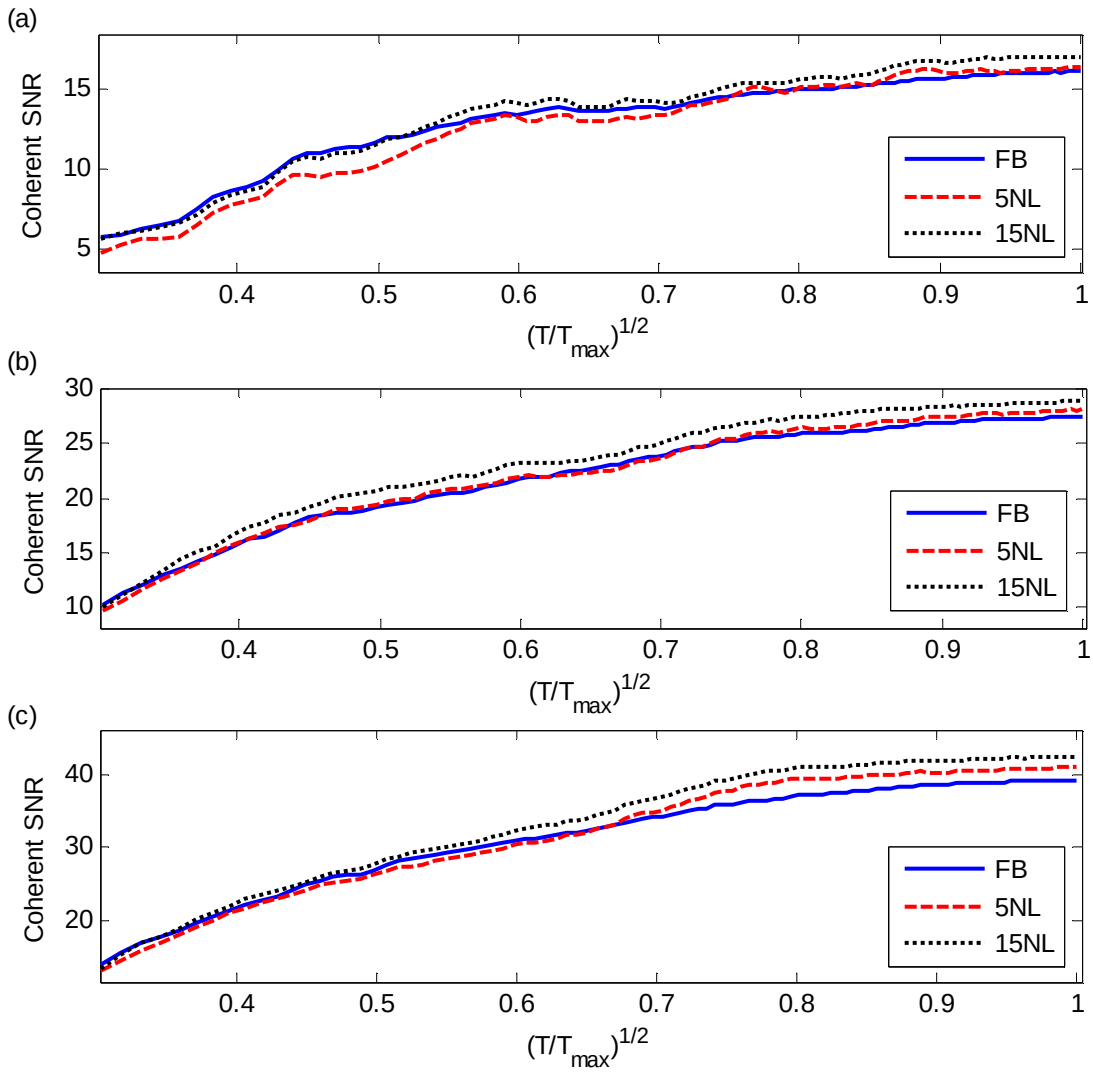

FIGURE 23: Evolution of the coherent *SNR* vs. the normalized recording duration $\sqrt{T/T_{\max}}$ for T_{max}=3.87ms using three clipping levels of the recordings: no clipping (solid line), 5NL (dashed line), and 15NL (dotted line) with **23.a:** N=25, **23.b:** N=100, **23.c:** N=200.

In order to compare the experimental result obtained in Fig. 23, the theoretical prediction had been computed from Eq. (13). As the waveforms are best reconstructed with increasing numbers of secondary sources, the variables in Eq. (13) have been estimated from the experimental results using N=200 points.

In the selected time-window T=[0.43ms-4.3ms], the exponential decay of the reverberant field was estimated as τ_D =3.8ms (see the procedure described in Section 3.2.2), the average signal-to-noise ratio of the recorded waveforms was measured as $SNR_r = 616 >> 1$, and finally t corresponds to the arrival time of the A_0 mode t_0=0.148ms. Due to the high-values of the recorded SNR_r, the influence of the incoherent measurement noise can be neglected in the selected time-window [0.43ms-4.3ms], and Eq. (13) tends toward Eq. (14). Thus Eq. (14) was used to predict the theoretical variations of $SNR(t)$ (dot-dashed line) which are compared in Fig. 24 to the variations of the coherent experimental *SNR* of the signals clipped at 15NL with N=200 points (dotted line).

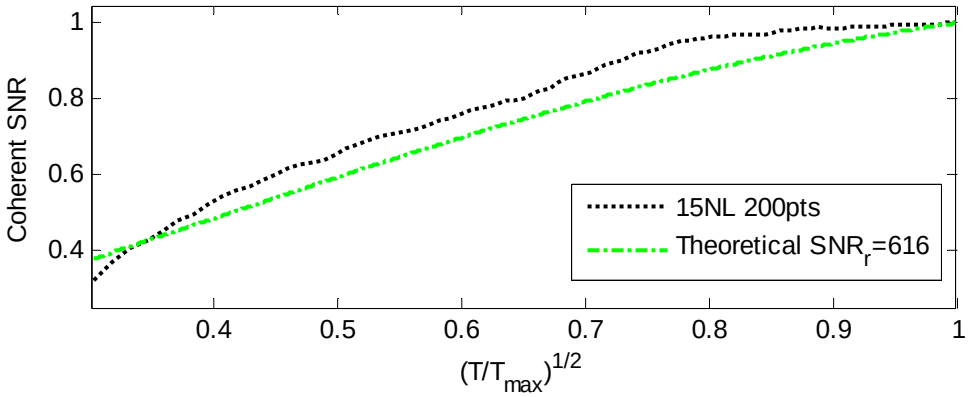

FIGURE 24: Comparison between the experimental variations of the coherent *SNR* of the cross-correlation waveforms obtained using a clipping at 15NL and *N*=200 (same as Fig. 23.c dotted line) and the theoretical predictions for 0<T<T_{max} obtained from Eq. (14) by using: T_{max}=3.87ms, t=t_0=0.148ms, τ_D =3.7ms, SNR_r=616.

The theoretical curve appears in good agreement with the measured one. Both experimental and measured variations of the coherent $SNR(t)$ tend towards the expected plateau when $T > \tau_D$ (i.e. when all the energetic part of the recorded waveforms had been processed). This limit shows that the *SNR* does not depend on the length of the signal beyond a certain recording duration, as the energy in the late arrivals is not enough to

have a significant contribution in the evaluation of the *SNR*. The recording of the signal can thus be done on shorter period of time than 12.8ms, as it has been done here.

Different time-windows of same length

Now that we know that increasing the recording duration of the signal will not improve significantly the coherent *SNR*, a further study had been performed to evaluate the energy content of different parts of the signal by studying the coherent *SNR* on different time-windows of same length; and thus to assess the effect of incoherent measurement noise on the performance of the DFI. Each reverberant signals collected over the whole measurement grid were first filtered in *B*, and then clipped at 5NL, then they were divided into four arbitrary time-windows of same length: T_1=[0 - 4.6133]ms, T_2=[1.3672 - 5.9258] ms, T_3=[2.7344 - 7.2930] ms , T_4=[4.1016 - 8.6602]ms as shown in Fig. 25.a. The four estimates of the GF using all processed reverberant signals (N=610) for each of the four selected time-windows, are presented in Fig. 25.b. As seen earlier, no big difference can be observed between each coherent A_0 arrival. A study of the arrival time t_0 was also conducted, to confirm this observation. On the first three windows, t_0 is the same (t_0 = 0.14785ms) which also corresponds to the final time found by taking the entire signal filtered in *B* and clipped at 5NL without any length constraints. On T_4, $t_0^{(4)}$ has a difference of 0.2 μs compared to the previous one, which remains a really good result. This highlights the robustness of the DFI process for obtaining deterministic Green's function estimate and illustrates that both early (e.g. window T_1) and late coda (e.g. window T_4) portions of the diffuse recordings -of similar duration- contain a comparable amount of coherent propagating waves, or "coherent information", between

the actuators locations #1 and #2 for this randomly cut thin plate. However, the effective recorded SNR_r decreases over the four selected time-windows since the amplitude of the reverberant wavefield decays exponentially with time (see subsection 3.2.2) while the amplitude of the incoherent measurement noise likely remains constant throughout the recording.

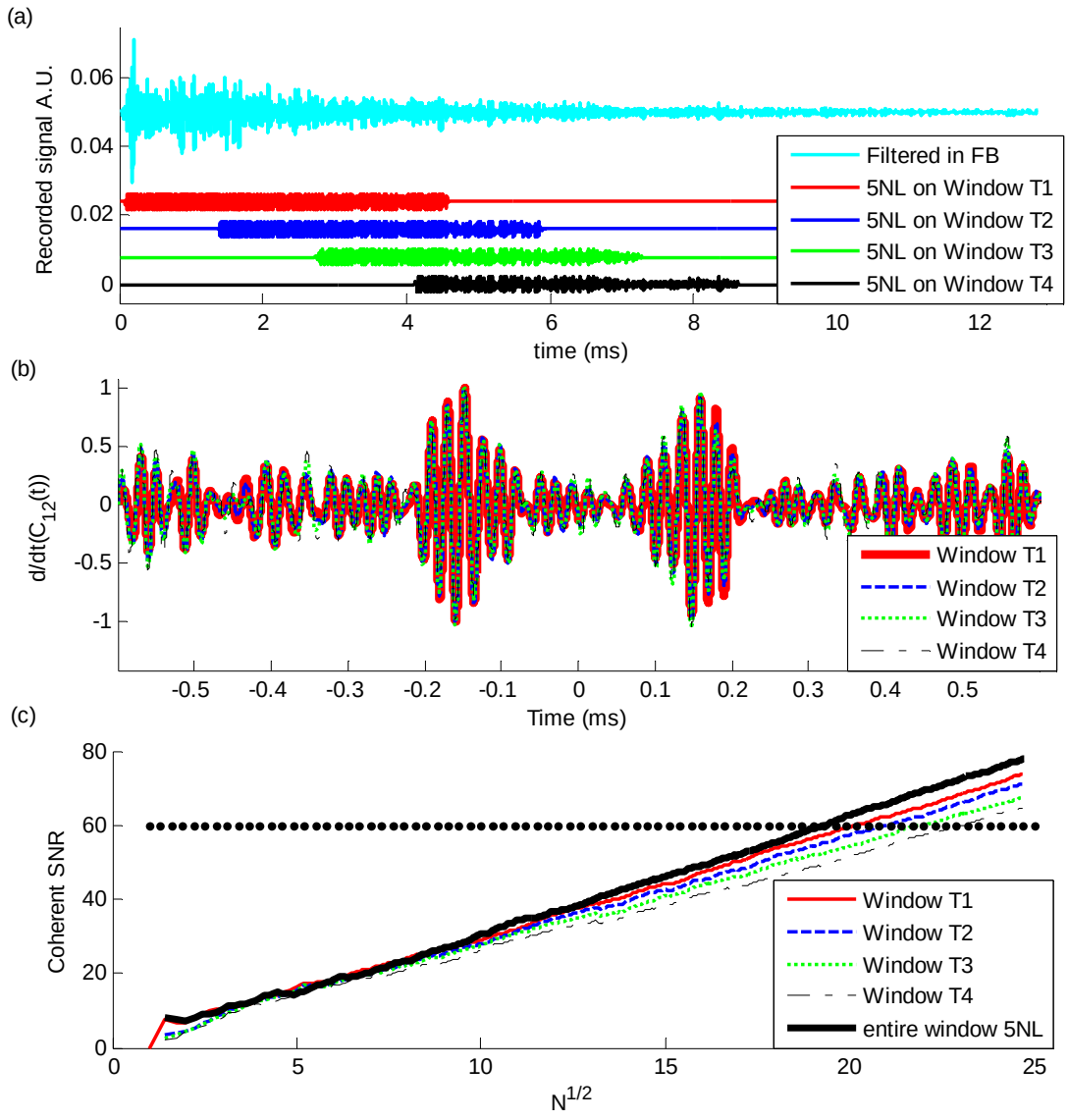

FIGURE 25.a: Typical recorded waveform filtered in *B* along with the four selected time-windows: T_1=[0-4.6133]ms, T_2=[1.3672- 5.9258] ms, T_3=[2.7344- 7.2930] ms , T_4=[4.1016-8.6602]ms of the clipped waveform. **25.b:** Coherent A_0 arrivals obtained from DFI for T_1 to T4 (N=610). **25.c:** Variations of the coherent $SNR(t_0)$ vs. $\sqrt{N}$ obtained from DFI using the time-windows T_1-T4.

Consequently, in agreement with the theoretical predictions from Eq. (14), the achieved coherent $SNR(t)$ for a given number of secondary sources N is lower when using late coda waves (e.g. window T_4) when compared to early coda waves results (e.g. window T_1) (see Fig 25.c). For instance in order to obtain an arbitrary value of 60 for the coherent $SNR(t_0)$ of the A_0 arrival, the number of secondary sources is increased from respectively N=408 in the window T_1, N=445 in the window T_2, to N=488 in the window T_3, and finally to N=535 in the window T_4. The variations of the coherent $SNR(t_0)$ evaluated on full length clipped at 5NL signals (T_{5NL}=[0-9.1]ms) is also shown for comparison (thick solid line) and is always higher for the same value of N than the other computed *SNR*, as expected from Fig. 23.

To conclude, by cross-correlating the diffuse part of the signal, an estimate of the local field Green's function can still be extracted using a large number of sources (here 130 sources more than with the early arrivals evaluation). The high number of sources required for this computation can be also explained by the fact that the diffuse field is not enough rich in modes.

3.2.4.6 Parametric variations of the coherent *SNR* vs. *N* and *T*

The last section of this chapter summarizes the previous studies in Fig. 26. Figure 26 displays contour plots of the variations in coherent *SNR* of the A_0 arrival for increasing values of T and N using three different pre-processing of the filtered reverberant waveforms: 5NL or 15NL clipping level or no clipping at all (similarly to the procedure used to generate Fig. 15 and Fig. 22). Based on the results from Fig. 19-20 showing that

the specific distribution of secondary sources does not influence significantly the coherent symmetric A_0 arrival computed from DFI, only one random realization of the spatial distribution of the secondary sources was used for any given value *N* (up to *N*=200 here). These parametric variations coherent *SNR* displayed on Fig. 26 are a summary of the combined results displayed in Fig. 17 and Fig. 23. Each contour represents a constant *SNR* level at the indicated value from 8 (i.e. 18dB) to 38 (i.e. 32 dB).

As expected, Fig. 26 shows that obtaining a given value of coherent *SNR* from DFI can be achieved by increasing either the recording duration *T* or number of sources *N*. Furthermore, following the findings from Fig 15.b and Fig. 16, Fig. 26 also illustrates the possibility of using amplitude clipping of the recorded data to further reduce the required value of *T* or *N* to achieve a given coherent *SNR* value, as seen by comparing the *SNR* contours on Fig. 26.a and Fig. 26.c. The asymmetric shape of each *SNR* contour curves with respect to the variables *T* and *N* also shows that an increase in recording duration *T* can not always compensate for a lack of secondary sources when using noisy multiply scattered signals. Indeed the near vertical portion of these parametric curves for small value of *N* shows that the coherent *SNR*(*t*) tend towards a plateau when $T > \tau_D$ due to the exponential decay of the measured reverberant waveforms and the influence of the incoherent measurement noise for low recorded SNR_r (see Eq. (13) and Fig. 21). Figure 26 shows that a given value of coherent *SNR* can be achieved optimally in the "elbow" region of each curve by minimizing both the necessary recording duration *T* and number of sources *N*. However, the lower the desired *SNR* level is, the fewer combinations of the parameters *T* and *N* exist, as the "elbow" region is sharper than for higher *SNR* levels. Indeed, for high SNR level, the contours begin to have a third linear

region instead of an “elbow” region, and these regions provide more possibilities to optimize the combination.

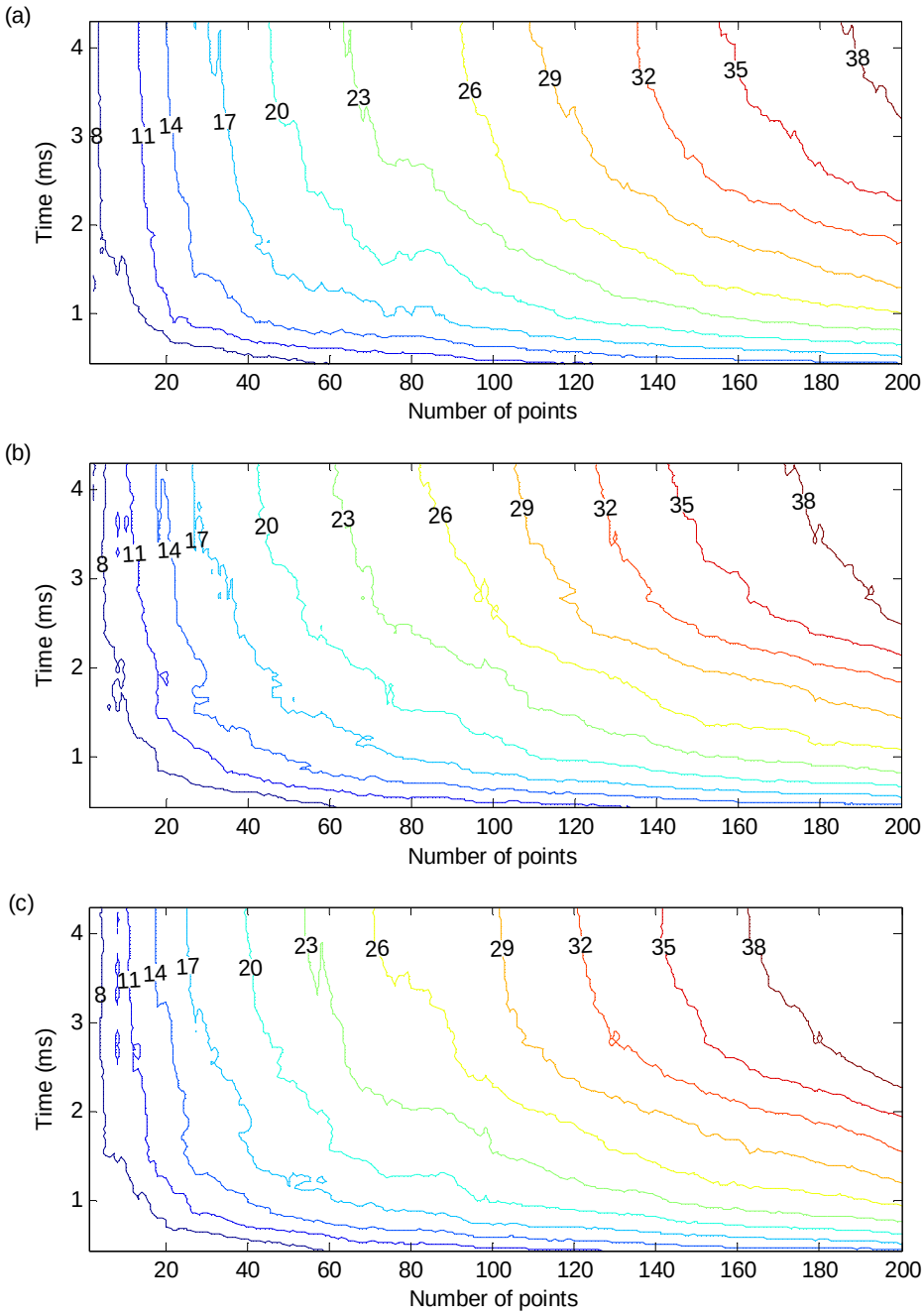

FIGURE 26: Parametric variations of the coherent *SNR* (linear scale) as a function of the recording duration *T* and number of secondary sources *N* (selected randomly across the measurement plate). Prior to cross-correlations, the recorded signals were first filtered in *B* and then three different clipping levels were applied: **26.a.** no clipping, **26.b.** 5NL, **26.c.** 15NL.

For instance, inspection of Fig. 26 shows that a coherent *SNR* level of 17 could be optimally achieved with the respective combinations (1.49ms, 47), (1.53ms, 49) and (1.37ms, 43) while for 35 the choice is wider, possible combinations are (3.25ms, 165), (2.82ms, 163) and (2.78ms, 152). The choice of the best combinations is not easy. It needs to be specified here that none of these contours have been smoothed which complicates the lecture on it. We can see that for a *SNR* level of 17, using N=25 points or N=200 points does not make a big difference (recording duration diminished by only 0.12ms and only 4 sources in less), however there is a clear improvement for a *SNR* level of 35: 0.5ms and 13 points win by using N=200 points instead of N=25 points. These figures are also useful to choose the right amount of sensors according to a specific recording duration.

3.3 Conclusion

The estimation of the Green's function of a mechanical structure using Diffuse Field Interferometry provides the possibility of remote SHM with none or a limited number of ultrasonic sources. Hence DFI provides a mean for local estimation of the monitored structure, which is easy to interpret and free from aberrations introduced by the source, from the effects of multiple reflections and distortions caused by structural and material complexity often encountered in typical aircraft components.

To study the potential of the DFI for passive and real-time Structural Health Monitoring of remote structural hot-spots in complex aircraft structures, Chapter 4 presents the results of the detection of a simulated defect using the DFI technique.

CHAPTER 4

DEFECT DETECTION EXPERIMENTS

4.1 Presentation of the two experiments

Experiments were conducted with the same aluminum plate as the first experiment described in Chapter 3 of thickness 2mm. In addition of cutting the plate edges irregularly, slots were cut on one edge of the plate to randomize the field faster (see Fig. 27) [Evans and Cawley 1999; Weaver 1986]. Instead of using piezoelectric actuators, the plate was excited by an impulsive ND-YAG laser (Continuum - Surelite). The use of the laser was motivated by several reasons. First, the laser has a wider frequency range than the actuators actually have. Secondly, the same excitation will be exactly reproduced at different locations. Finally, the laser allows us to easily excite the plate at more than two locations without moving the plate and grid, for practical SHM implementations of the DFI technique, it is likely that approximately only twenty sources would be used (as opposed to several hundred used in Chapter 3). The recordings of the out-of-plane displacements were here again done with the same Scanning Laser Doppler Vibrometer (SLDV, Polytech).

Two different experiments have been conducted on the plate. The first one was similar to the one described in Chapter 3, the ND-YAG laser was exciting the plate at two different locations #1 and #2, 10cm apart, and the SLDV was recording along a pre-defined grid of 339 points covering almost the entire plate (see Fig. 27). This experiment was done to confirm the similarities between actuator and laser excitements. The laser and the SLDV were synchronized through the data acquisition system of the SLDV. A wave generator (Agilent mod. 33220A – 20Mhz Functions) sending square pulses of

10μs long at 2Hz was exciting the laser.

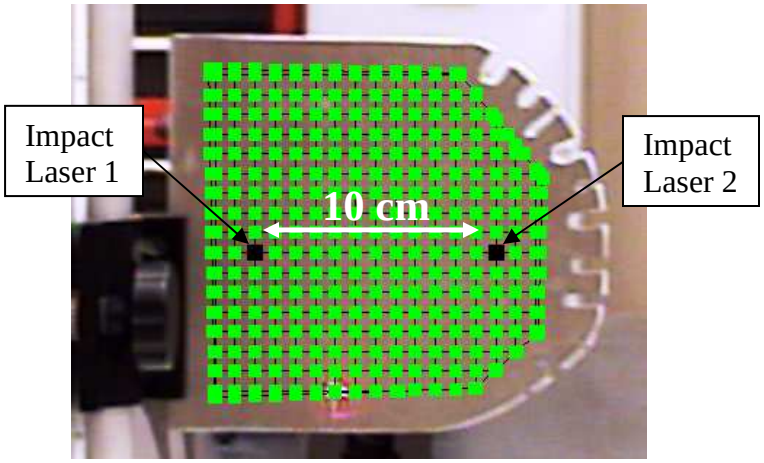

FIGURE 27: Location of the grid of 339 pts on the plate and the two laser impacts 10cm apart. The square pixel size is 0.83 cm.

The second experiment had for goal the detection of a defect and was thus done twice: once without defect (Experiment 1, with an intact plate) and once with one (Experiment 2, with a "damaged" plate). The setup is presented in Fig. 28. The two experiments were following the exact same scheme that consisted of exciting the plate at 25 random locations (approximately the same for both) using the ND-YAG laser (see Fig. 29.a), and the SLDV was recording the responses to each single excitation along a grid of 40 points split into two lines (see Fig. 29.b). The plate was fixed on an air table to avoid any vibration coming from the floor, and the laser was on a separated table to be able to move it easily without moving the plate. For practical reason, the lens was attached to the top of the laser using tape and a wooden support, thus avoiding the need to move the lens in order to focus the light of the laser each time the laser was moved. The SLDV was 1.5m away from the measured plate. Moreover, the defect, a damping screw, had been carefully stuck on the center of the scanning grid, so as not to move the plate between the two experiments. Indeed to be able to compare the recorded signals, neither

the plate nor the grid should move. The diameter of the contact zone (screw/plate) is 1.5cm.

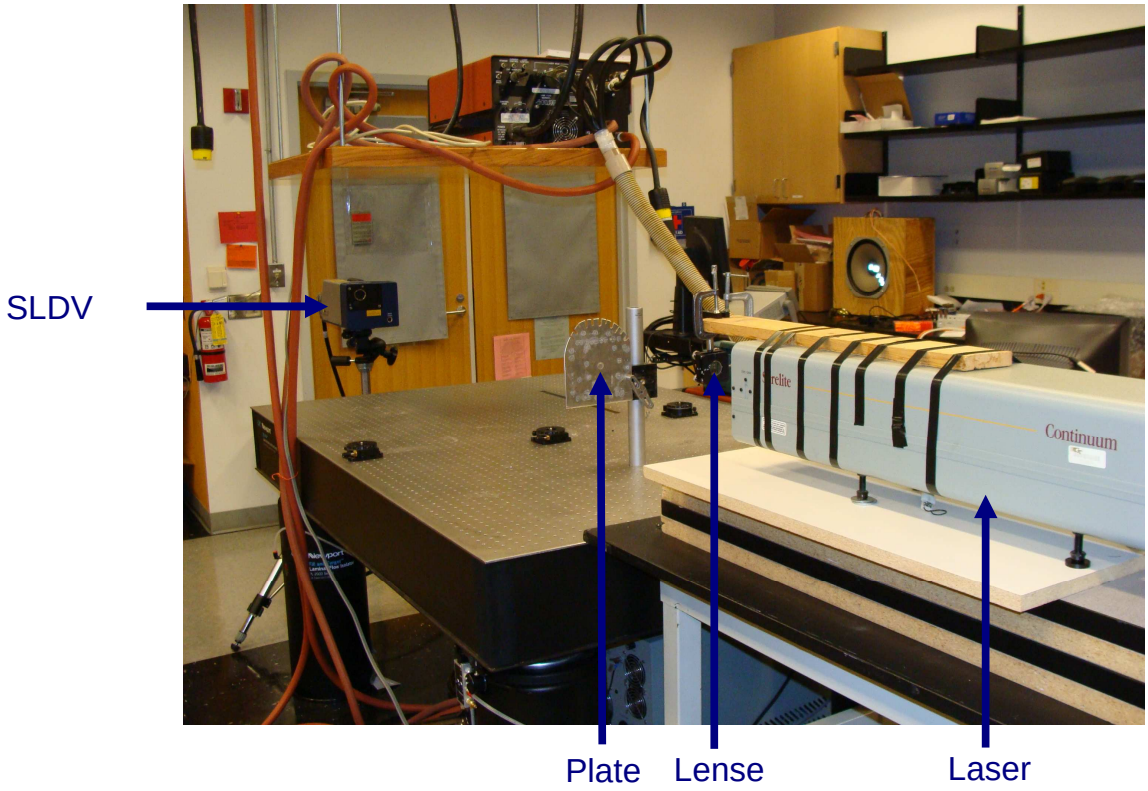

FIGURE 28: Setup of the defect detection experiment.

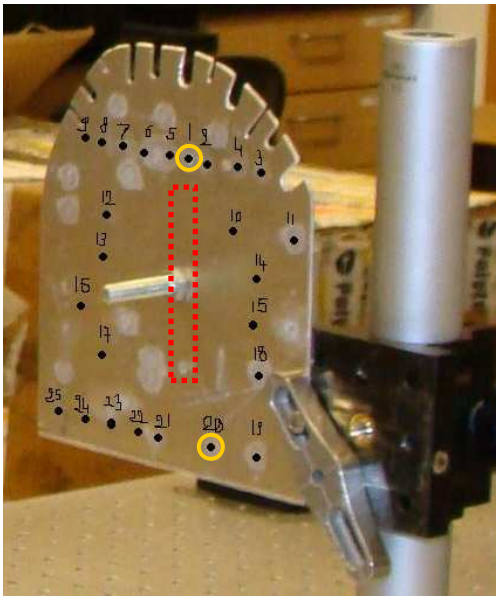

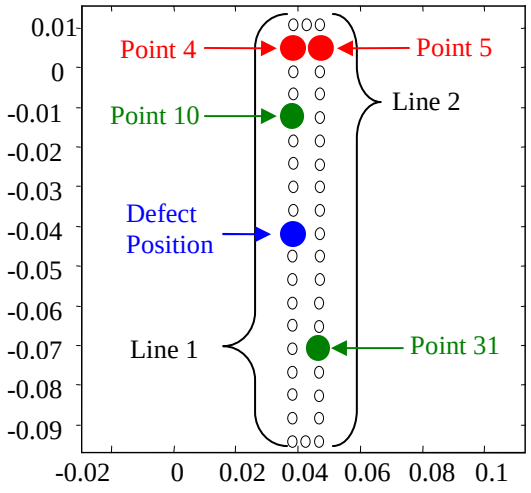

FIGURE 29.a: 2mm-thick aluminum plate subjected to laser excitations at the 25 different locations. The SLDV scanning grid is indicated by red dots. The defect, a damping screw, has been stuck on the center of the scanning grid. **29.b:** Pattern of the scanning grid of 40 points read by the SLDV (red line on Fig. 29.a). The vertical spacing is 0.46cm and the horizontal spacing is 1cm.

4.2 Experimental results

4.2.1 First experiment: Performance study

In this experimental setup, the signals had been recorded on a longer time-window, twice as long as the time-window of the experiment described in Chapter 3 (25.6ms compare to 12.8ms) at 339 points. The same method as earlier had been used to dismiss the bad points (see 3.2.1), but this time as we disposed of pre-trigger signal (see Fig. 30.a), by comparing the pre-trigger noise level of each signal to the mean one over the 339 points. After this, 317 points were remaining.

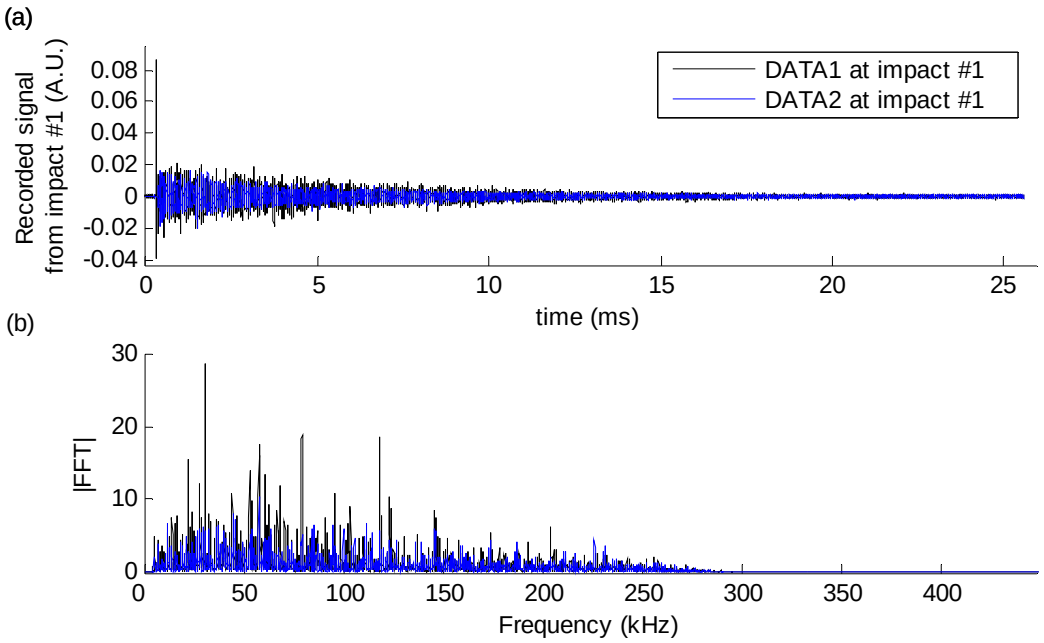

FIGURE 30.a: Waveforms collected by the SLDV following a laser impulse at impact #1 when hitting at impact #1 in black and at impact #2 in blue reported in function of time (see Fig. 27). **30.b:** FFT of the recorded signals: B_{laser}=[5-280] kHz. The energy is uniform along B_{laser}.

Figure 30.a shows the waveforms collected by the SLDV following a laser impulse at impact #1 when hitting at impact #1 in black and at impact #2 in blue reported in function of time (see Fig. 27). There is a delay between the two signals, which represents the traveling time of a wave from impact #1 to impact #2. The waveform shows also a long

"coda" caused by the multiple reflections on the edges. Moreover, Fig. 30.b illustrates the main interest of this experiment which is the wider frequency content of the signal. Indeed, in this case, the FFT is no more composed of several lobes where all the energy was mainly in one (B=[4-90]kHz) but only of one: B_{laser}=[5-280]kHz of high energy all along the window B_{laser}.

Furthermore, to have a comparison with the first experiment described earlier and especially with the study 3.2.3.1, the signals have been filtered in B=[50-90]kHz, and then clipped at different noise level: no clipping, 5NL and 15NL and all have been cut on the same time-window of length 7.6ms which corresponds like earlier to the length of the signals after clipping at 15NL.

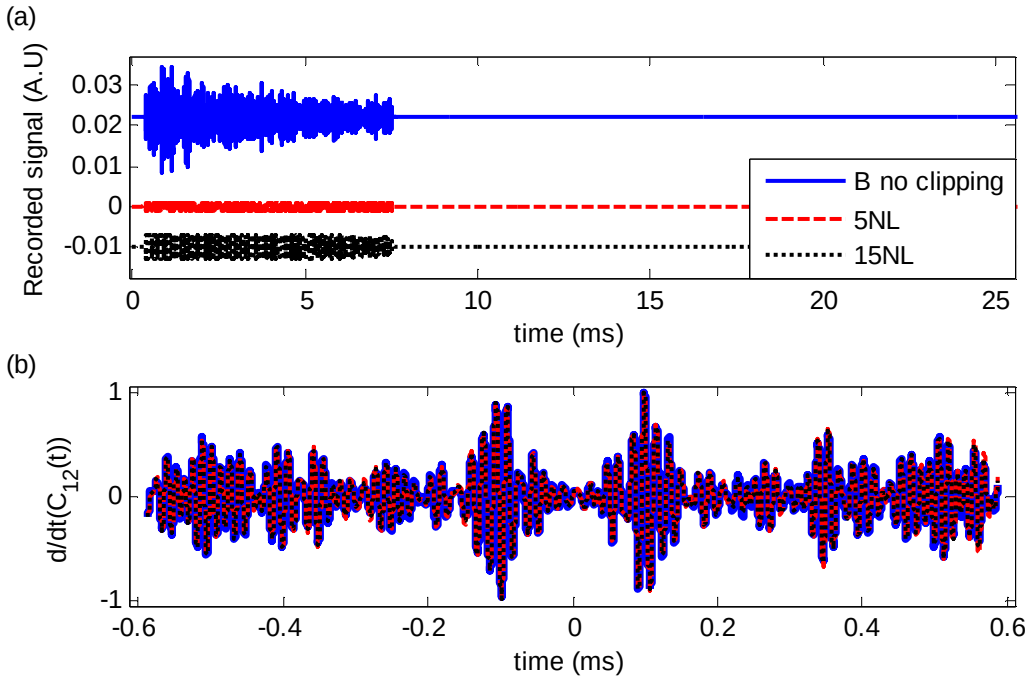

FIGURE 31.a: Recorded signal at impact #1 when impact #1 was active filtered in B=[4-90] kHz. The second and third ones had been clipped respectively at 5 and 15 times the electronic noise level over the same time-window of length 7.6ms. **31.b:** Normalized estimate of the Green's function of the 317 points added in a random order in the three cases.

Figure 31.a illustrates the three signals, and Fig. 31.b, the normalized estimate of the true GF corresponding to each case. As earlier, the arrival of the A_0 mode is similar in the three cases, and distinguished itself from the other arrivals. Also the three estimated GF are symmetric. Positive and negative measured A_0 arrival time for the three cases are all within 0.2μs of the asymptotic value obtained using the symmetric of the GF of the non clipped signal on all its length t_0=98.52μs. This value will help determining the phase velocity (see Fig. 33).

The *SNR* in function of $\sqrt{N}$ is given in Fig. 32. The variation of the *SNR* is the same as earlier growing as $\sqrt{N}$, regardless of the specific amplitude clipping threshold apply to the reverberant waveforms. As the contribution of only 317 points compare to 610 points in the first experiment had been taken into account, the *SNR* level reached here is lower and follows a smaller slope. Furthermore, results of Fig. 32 also demonstrate the slight improvement of coherent *SNR* when using a moderate clipping level (15NL, dotted line) with respect to no clipping at all (plain line). However, very low clipping level (5NL, dashed line) contrary to earlier does not improve the coherent *SNR* and stay approximately of the same level compare to the case of no clipping. This may occurs since this low clipping level artificially enhances the relative importance of the measurement noise component, and thus effectively lowers the recorded signal-to-noise ratio especially in the late coda. For instance in order to obtain an arbitrary value for the coherent *SNR* of 40 (i.e. 32dB), the number of secondary sources is increased from respectively 211 for a clipping threshold of 15NL to 217 when no clipping is applied and 220 for a clipping threshold of 5NL.

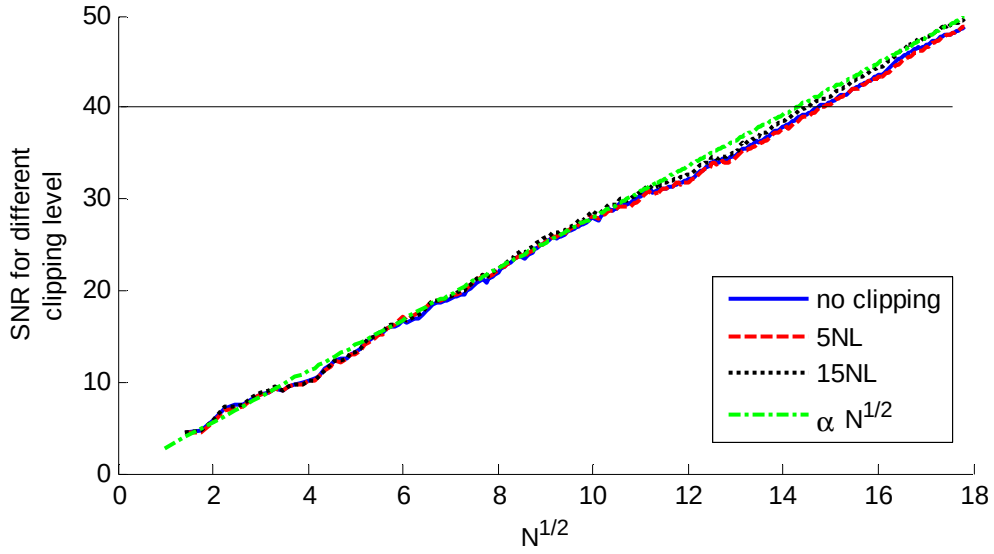

FIGURE 32: *SNR* in B_{laser} using the definition given by Eq. (2-4) for the three cases of thresholding from the previous figure in function of $\sqrt{N}$. The theoretical result is given in green, and confirms the growth in $\sqrt{N}$.

As previously, the precision of the phase and group velocity measurements obtained from DFI for a given set of N=317 points secondary sources is studied, in addition to the usual coherent *SNR* metric (see 3.2.4.2). The phase (resp. group) velocity was estimated as C_p=1015m/s^{-1} (resp. C_g=1014m/s^{-1}), using the value of the arrival time t_0 =98.52 µs (resp. t_0^{env} =98.7 µs) and knowing the separation distance D=10 cm between the two impact locations. These results are in good agreement with the ones estimated in the previous part C_p=1057m/s^{-1} (resp. C_g=1020m/s^{-1}) and thus with the predicted valued for the A_0 mode (wavelength λ≈1cm) in aluminum samples [Achenbach, 1993]. Figure 33 displays the variations of arrival time of the maximums of the symmetric cross-correlation waveform and its envelope, in the same three cases (5NL, 15NL clipping or no clipping all on a 7.6ms time-window) as in Fig. 31. A logarithmic scale was used for the horizontal axis in order to enhance the visualization of the variations for small values

of the parameter *N*.

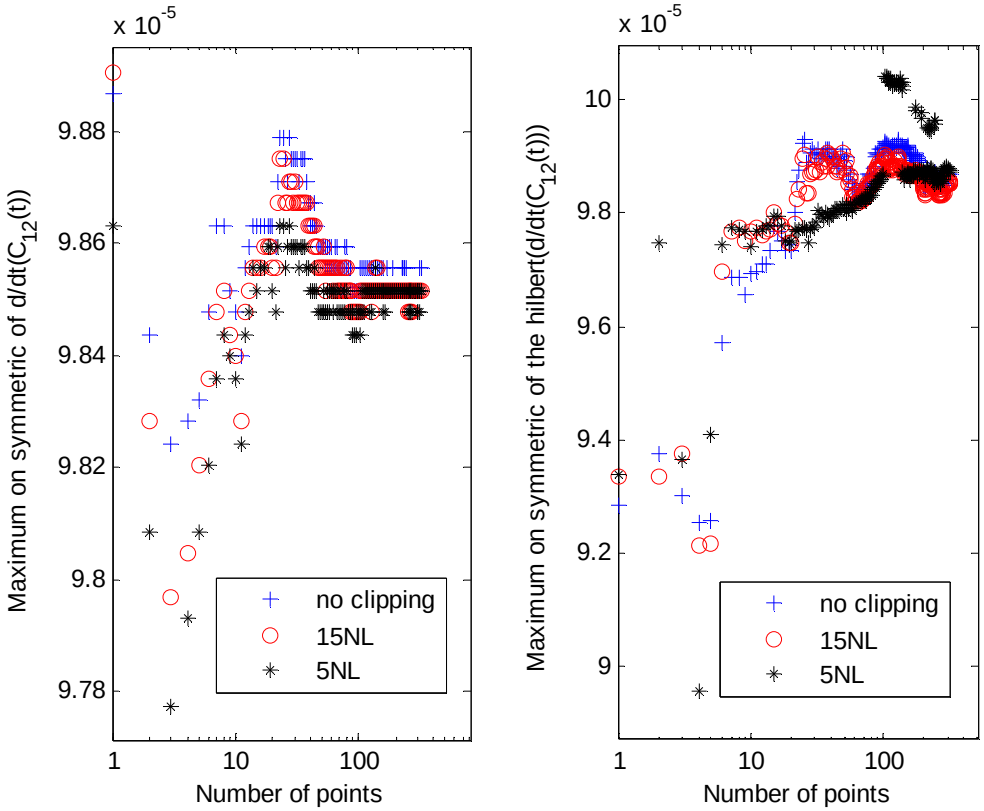

FIGURE 33.a: Evolution of the time of the maximums of the symmetric of the Green's function for the three cases in *B* in function of the number of sources ($\log_{10}$ (*N*)). **33.b:** Evolution of the time of the maximums of the symmetric the envelope of the Green's function for the three cases in function of the number of sources ($\log_{10}$(*N*)).

Contrary to Fig. 18, the variations of time given here are not centered on 0 but on the true values. We can thus see that the three curves in both figures converge approximately towards the same limit. It is more obvious on the Fig. 33.a. Indeed the vertical scale is different on both figures, and the variations are much higher in Fig. 33.b but stay in a good range of error. Overall in all cases, the error in measured arrival times becomes very small (<0.2 µs) after *N*=46 (resp. *N*=140) for phase (group) velocity measurements. These errors are slightly smaller than the one obtained with the piezoelectric. Hence, at this point, the obtained cross-correlation waveforms from DFI should yield reliable

estimates of the phase and group velocity of the A_0 mode on this thin aluminum plate.

These results show the equivalence between the two methods (piezoelectric or laser excitation).

4.2.2 Second experiment: Defect Detection

The spatial distribution of the 25 secondary sources (all around the grid) have been chosen to optimize the creation of diffuse field (see 3.2.4.5) and thus the extraction of the time domain Green's function from DFI between any two points of the scanning grid. The extraction of a high number of potential GF is the first objective (Experiment 1, with an intact plate). The second objective is to demonstrate that the extracted GF from DFI allows high-resolution detection of a defect located in the monitoring grid (Experiment 2, with a "damaged" plate).

4.2.2.1 Recorded diffuse fields

The diffuse field recorded by the SLDV at the grid point #4 (see Fig. 29.b) when the laser was impacting source point #1 (top middle of the plate, see Fig 29.a) is shown in Fig. 34. The FFT of the recorded raw data in Fig. 34.b shows once again that the ND-YAG laser has a large frequency bandwidth due to the impulsive nature of its excitation. We will however concentrate our study in the frequency band: B= [50-200] kHz, where the sensitivity of the SDLV is the highest. The signals presented in Fig. 34.a have been both filtered in this frequency band. Following the approach described by Sabra and al. (2008), the filtered signals were further processed using an amplitude

clipping procedure to assign uniform weights to the multiple reverberations (see 3.2.4.1). The level of the threshold was set at 30 times the standard deviation of the electronic noise level (30NL) which was estimated from the pre-trigger part of the signals. Fig. 34.a compares both the clipped (blue line) and original filtered (red line) signals.

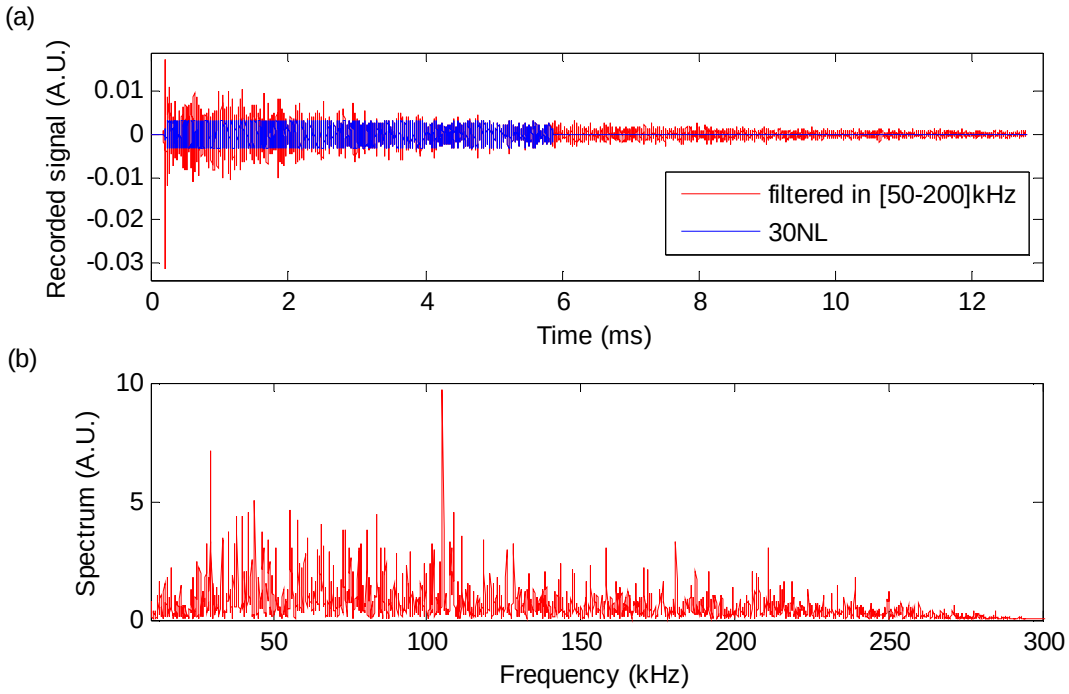

FIGURE 34.a: Recorded signal at #4 when the laser was exciting the plate at laser pt1 and filtered in B=[50-200]kHz. Comparison between the signal only filtered (red) and the signal also clipped at 30 times the electronic noise level (blue). **34.b:** FFT of the signal before filtering and clipping.

4.2.2.2 Estimate of the true GF and defect detection

Following the theoretical results from Eq. (4), the time-derivative of the cross-correlation functions between all sensor pairs, normalized by the energy of the records, was computed and then summed over all 25 secondary sources contributions. This was done in order to estimate all possible local GF between the scanning points and a fixed sensor reference. Fig. 35.a (resp. b) displays the normalized estimates of the GFs between point #5 (resp. point #4) and all sensors on the vertical line where it lays: line2 (resp.

line1) (see Fig 29.b). Each curve had been normalized by the maxima derivative of the auto-correlation of the signal without defect. Clear propagating wavefronts emerge from this coherent processing, as if the sensing points #4 and #5, located on the top of the scanning grid acted as virtual sources. The two wavefronts correspond to the main A_0 arrival and to the first reflection, given the frequency bandwidth of the recording and the fact that the SLDV records the plate out-of-plane displacements. Moreover, in agreement with theoretical predictions for a fully diffuse field, the noise cross-correlation is a symmetric function of time. Similar results were obtained using as reference sensors #20 and #21 which are located in the middle of the scanning grid (see Fig. 37). The "X" shape wavefronts correspond to A_0-dominated responses propagating away from the reference sensors.

The second experiment was then conducted, using the same experimental setup, by attaching to the plate a screw, acting as a local "defect". The effect of additional mass is to strongly attenuate the incident waves as shown in Fig. 36, where the attenuation effect of this surrogate defect is clearly visible in the recorded signal at sensor #20, which is located over the defect location. Figure 35 compares the estimated GF with and without defect. First, the difference in the amplitudes between the curves is only visible in Fig. 35.b and not in Fig. 35.a. This is due to the strong attenuation effect of the attached defect on the amplitude of the direct path for the GF between sensor #4 and the middle points of line 1 (#18,#20,#22, located around 4.1cm from #1) (Fig. 35.b). In comparison, little variations occur when sensor #5 is used as a virtual source since the defect is not on the direct path. Hence DFI allows the precise localization of the "defect" in the middle of line 1 of the scanning grid, without the need for a-priori information.

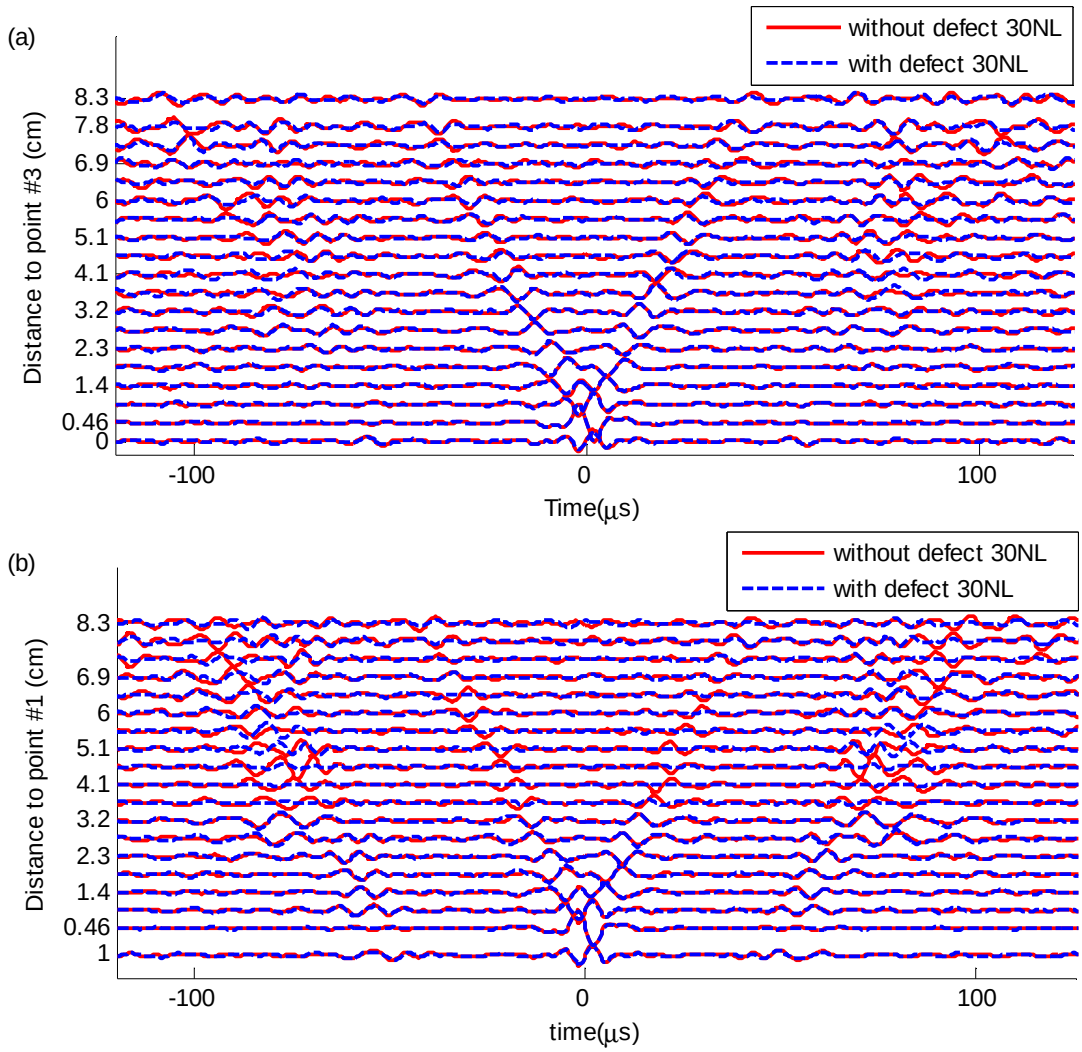

FIGURE 35: Comparison of estimates of the Green's function with and without defect. **35.a:** Green's function estimates between point #5 and the points along line 2. **35.b:** Green's function estimates between point #4 and the points along line 1.

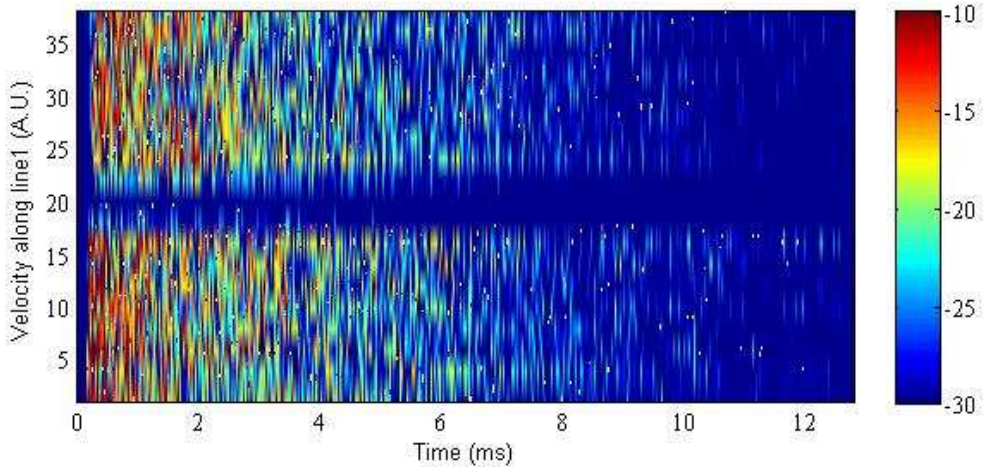

FIGURE 36: Recorded signals along line 1 when the laser excited the plate with defect at laser pt1 vs. time.

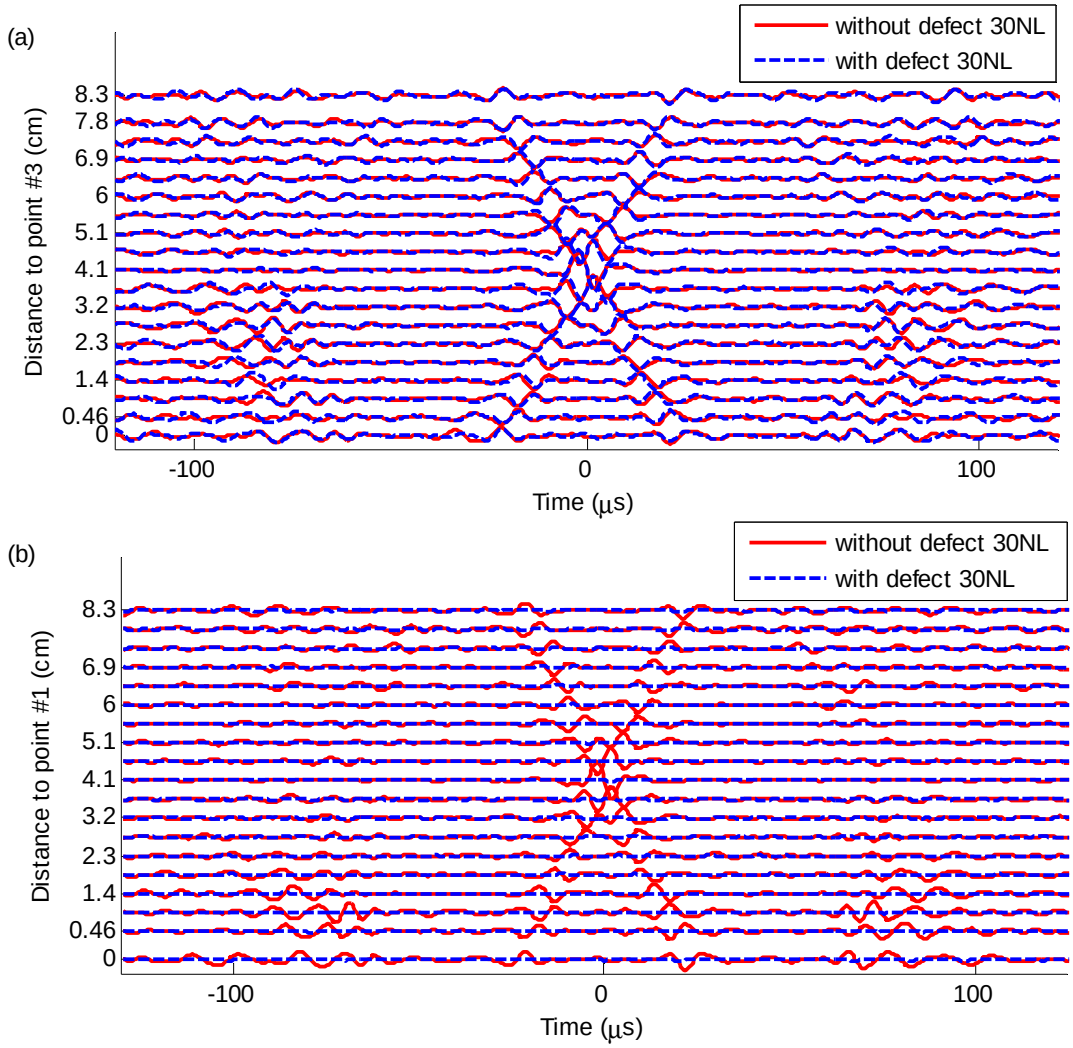

FIGURE 37: Comparison of estimates of the Green's function with and without defect. **37.a:** Green's function estimates between point #21 and the points along line 2. **37.b:** Green's function estimates between point #20 and the points along line 1.

Figure 37.a and .b further illustrate the high-resolution detection and localization of the defect from DFI using sensor #20 (i.e. at the actual defect location) and #21 as virtual sources. The GF estimates between the point #20 and line 1 has very low amplitude when the defect is present for all the points on the line: the virtual source #20 can not excite the plate since all waves are damped by the defect. On the other hand, the estimated GF between point #21, only two centimeters apart from the point #20, and the line 2 is not affected by the defect.

4.2.2.3 Time reversal reconstruction of the defect location

After estimating all the different GF for every single pair existing, and having a clear idea of the defect location, some more data reduction have been performed to identify the defect location precisely following the method described in [Tarantola 1984; Fichtner et al. 2006]. This method is based on the time reversal of the error produced by the defect back onto the source that created it, i.e. the defect location. The study has been performed on the symmetric of the estimated GF.

A first step consisted of evaluating the error which is the difference between the estimate of the GF without and with defect for every pair of points given by:

$$Error = (GF^{D}_{A,B} - GF^{U}_{A,B}) \tag{18}$$

where ^{U} stands for undamaged and ^{D} for damaged. Figure 38 illustrates the *Error* between the points #10 and #31 (plain blue) and the first arrival of the *Error* (dotted line) (Fig. 29.b and next step).

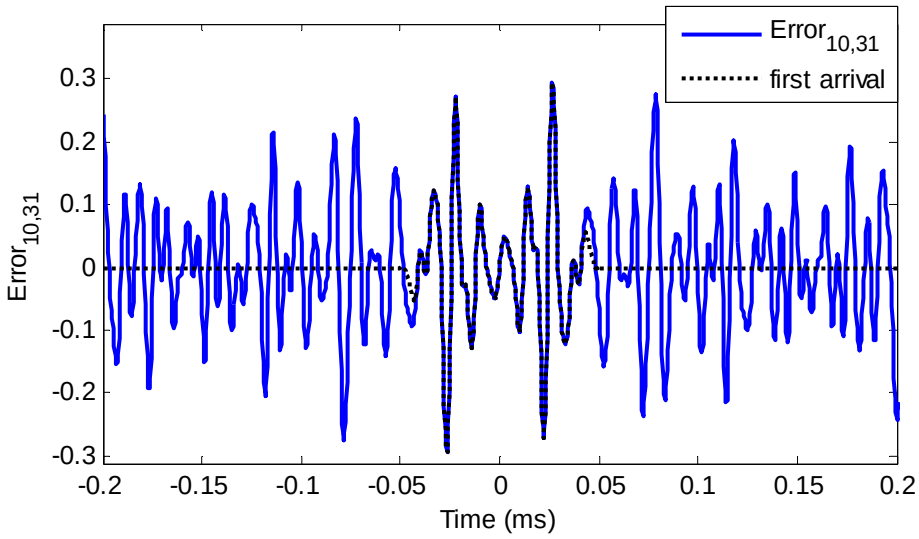

FIGURE 38: Error between the points #10 and #31 (plain blue) and the first arrival of the *Error* (dotted line).

Secondly, only the part included into the time interval [-60 ; 60]µs, which correspond to the first arrival, has been kept in each estimated GF undamaged ($GF_{i,j}^{U}$ where i and j are chosen arbitrarily) or damaged ($GF_{i,j}^{D}$) and also in the term *Error* (see Fig. 38). Figure 39 illustrates the undamaged $GF_{10,31}^{U}$, and in black is the first arrival of the wavefront between these two points and thus the only part kept for this study.

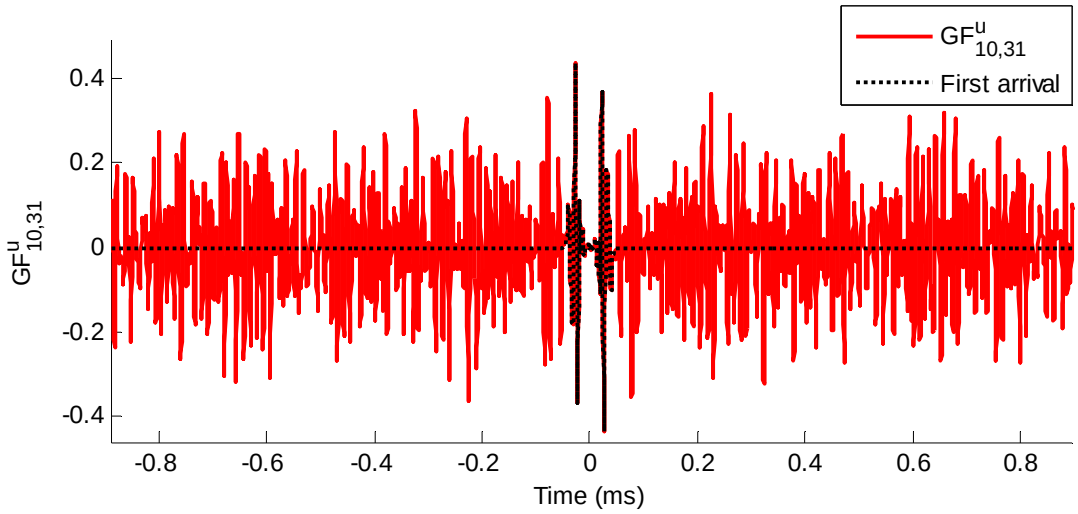

FIGURE 39: GF without defect between the points #10 and #31 (solid line), and first arrival in black.

Then, the third step was the whitening of the FFT of the estimates of the GF and also of the *Error*. The whitening consists of clipping all frequencies to a certain level so that there is no frequency dominating when it should not. The new FFT of the GF is given by:

$$FFTnew = \frac{FFT(GF_{i,j})}{abs(FFT(GF_{i,j})) + .05 * \max(abs(FFT(GF_{i,j})))} \tag{19}$$

where $GF_{i,j}$ is the estimate of the Green's function between the point i and j, *FFTnew* is the whitened FFT. This allows weighting spectral components based upon prior spectral components, and averaging spectral components with prior spectral components. Back in the time domain, the estimated GF without defect between the point #10 and the line1

(see Fig. 29.b) before and after whitening are compared in Fig. 40. Figure 40 shows that the signals recorded in this experiment are good, as there is not much difference between the whitened and the original estimated GF.

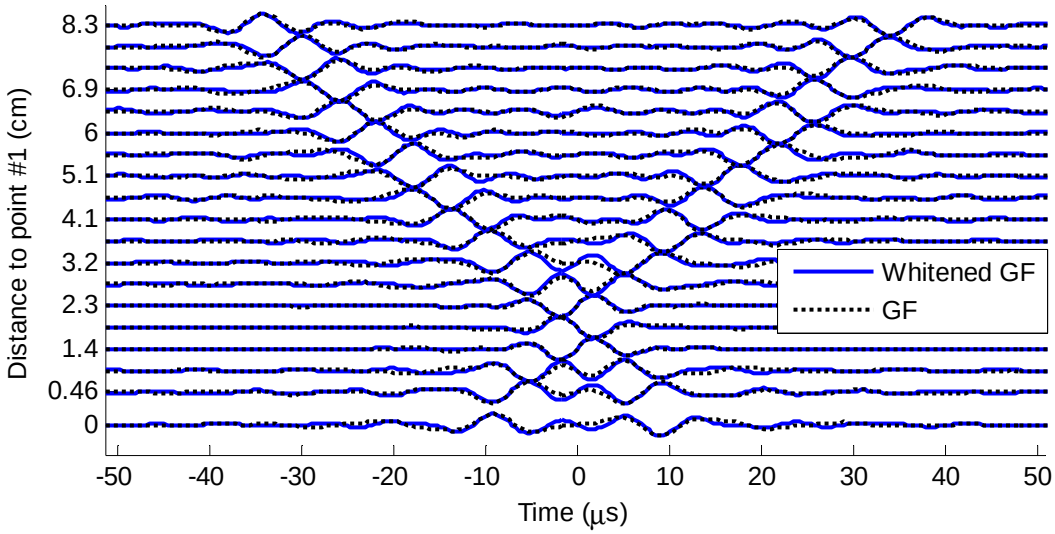

FIGURE 40: Comparison of the GF without defect between point #10 and line1 before (solid line) and after (dot line) whitening the FFT. The ordinate axis gives the number of the points #j on line1.

The final step was the defect location by using the *Error* term between two points #A and #B generally chosen each one on a different line. Moreover #A and #B have to be far enough from each others and on both side of the defect location estimated from the subsection 4.2.2.2 (location #20).

Let us first consider the two undamaged GF profiles of #A (resp. #B) and line1: $GF^{U}_{A,j}$ and $GF^{U}_{B,j}$ given in Fig. 40.

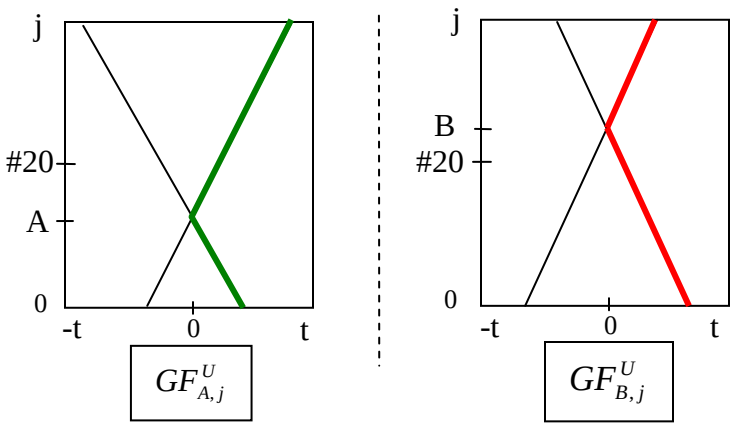

FIGURE 41: Profile of the first arrivals of the GF without defect (U for undamaged) between the points #A (resp. #B) and #j describing the entire line1.

Then the selected model tells us to convolute the conjugate of the *Error* and the two undamaged GF terms one at a time. These terms are given by the following formulas:

$$GF^{Error(A,B)}_{B,j} = \overline{(GF^{D}_{A,B} - GF^{U}_{A,B})}.GF^{U}_{B,j}$$
$$GF^{Error(A,B)}_{A,j} = \overline{(GF^{D}_{A,B} - GF^{U}_{A,B})}.GF^{U}_{A,j} \qquad (20)$$

where j covers line1, #A usually will be chosen on line1 and #B on line2. What the convolution actually does, is shifting $GF^{U}_{A,j}$ (resp. $GF^{U}_{B,j}$) to the right onto t_0^{Error} and to the left onto $-t_0^{Error}$ which are the times of the first A_0 arrival on the positive and negative sides of the *Error* term between the points #A and #B. These times are represented in Fig. 42 by the vertical dashed dot blue lines. So basically $GF^{U}_{A,j}$ (resp. $GF^{U}_{B,j}$) are reproduced twice symmetrically to t=0 centered on t_0^{Error} (dashed lines on Fig. 42). The important part in this study is how the positive side of $GF^{U}_{A,j}$ (resp. $GF^{U}_{B,j}$) is shifted (see the dashed lines in both profiles of Fig. 42). Indeed the intersection between one of these positive parts of $GF^{Error(A,B)}_{B,j}$ (resp. $GF^{Error(A,B)}_{A,j}$) and the positive side

of $GF^{U}_{A,j}$ (resp. $GF^{U}_{B,j}$) is where the defect is located. Figure 42 represents the defect location using this described technique.

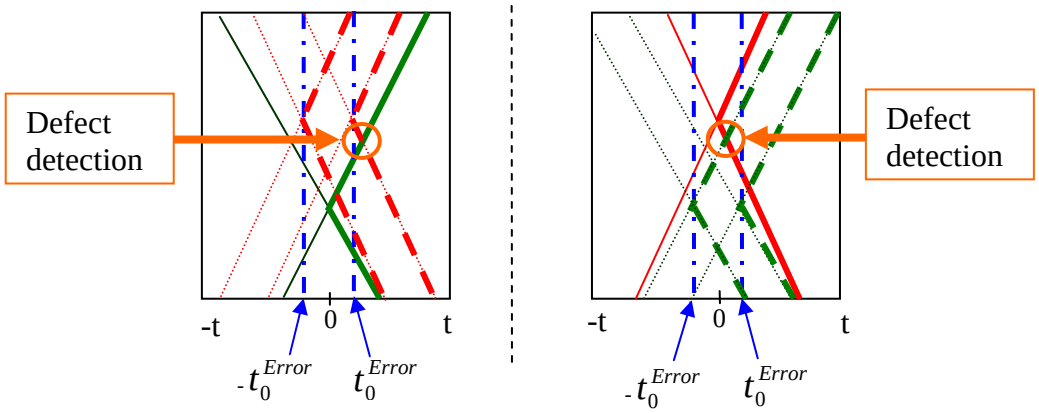

FIGURE 42: Detection of the defect location at the intersection between the positive side of the undamaged GF between #A and #j: $GF^{U}_{A,j}$ (solid red and "X" shape) (resp. $GF^{U}_{B,j}$ (solid green)) and $GF^{Error(A,B)}_{B,j}$ (dashed green line and "W" shape) (resp. $GF^{Error(A,B)}_{A,j}$ (dashed red)). The dashed dot blue line indicates the time of the first arrival in the *Error* term.

Fig. 43.a and .b illustrate this principle for the couple (#10, #31). The "X" shape of the undamaged estimate of the GF is distinguishable and given in solid red lines. And the "W" shape of the $GF^{Error(10,31)}_{AorB,j}$ is also clear in dashed blue lines. Both figures show that there are two intersections between the positive side of both $GF^{Error(10,31)}_{31,j}$ (resp. $GF^{Error(10,31)}_{10,j}$) and $GF^{U}_{10,j}$ (resp. $GF^{U}_{31,j}$) marked by circles. However, these two circles do not correspond to the location of the defect: in #20 but to the location of the two sources #10 and #31.

The result of this study is thus not good. Indeed instead of focusing onto the defect location it was focusing onto the sources #A and #B. This is due to the fact that almost all the energy contained in the error was mainly coming from the sources, which also means

that the screw glued on the plate had strictly damping effect and no scattering effect. To conclude, this method helped us to understand better what impact had the defect onto the field.

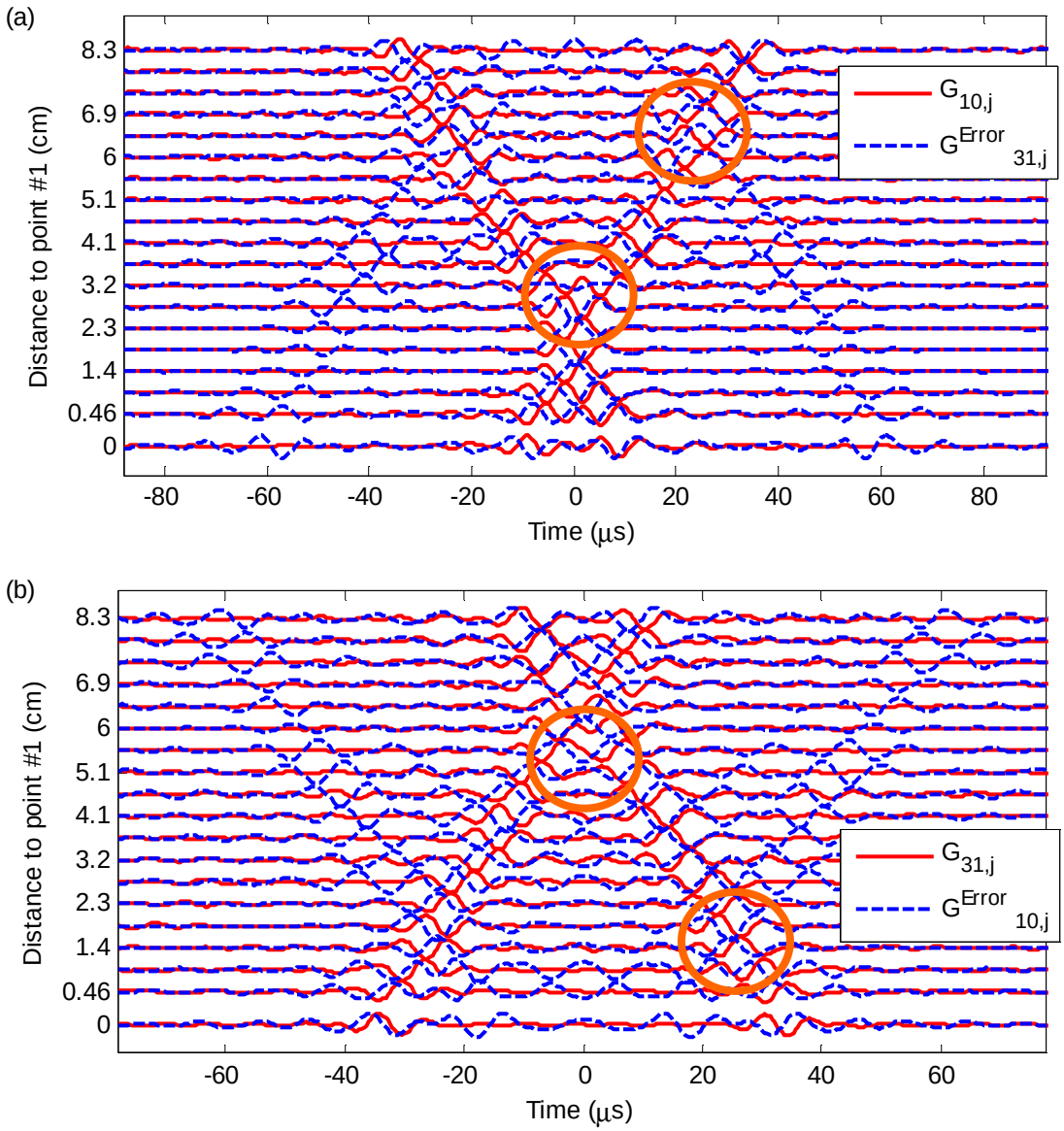

FIGURE 43: Comparison of $GF^{U}_{10,j}$ (solid red and "X" shape) (resp. $GF^{U}_{31,j}$ (solid red)) and $GF^{Error(10,31)}_{31,j}$ (dashed blue line and "W" shape) (resp. $GF^{Error(10,31)}_{10,j}$ (dashed line)) in order to locate the defect at the intersection of their positive side.

So to detect the defect another method such as tomography had to be used.

4.2.2.4 Tomography: defect detection

Using DFI, the local Green's function can be computed between any pair of the 40 SLDV locations surrounding the monitoring region with or without defect, thus providing up to 780 potential Green's function measurements between sensor pairs. This high number of crossed paths can be used advantageously for tomographic imaging of the defect region. It was found that the presence of the absorbing defect was affecting much more the amplitude the first coherent arrival (A_0 mode) than its arrival time. Hence only tomographic reconstruction of the local plate attenuation was performed thereafter. To do so, the monitoring area (see Fig. 29: width 2cm by height 9.2cm) was divided into small square cells of length 2mm. This grid size was determined by the sensor spacing and the measurement errors. The propagations paths of the A_0 mode along each pair of sensor #l-#m, on this the 2D tomography grid, were assumed to be straight. The ratio R_{lm} of the A_0 mode amplitude in the damaged case to the undamaged case was measured experimentally for each pair of sensors #l-#m. Hence, the amplitude of the A_0 mode in the undamaged case acts as a calibration factor when measuring the A_0 mode amplitude in the damaged case by effectively mitigating the amplitude variations caused by geometric spreading and transducer responses. By modeling the attenuation of the propagating A_0 wave by a simple exponential decay, the ratio R_{lm} can be expressed as (exponential decay):

$$R_{lm} = e^{-\gamma_{lm}} \tag{21}$$

where γ_{lm} is the relative cumulated decay of the A_0 mode along the inter-sensor path of length L_{lm}. A value of ratio R_{lm}=1 (i.e. γ_{lm}=0) theoretically indicates the absence of defect along path between sensors #l-#m. However, small amplitude fluctuations of the

ratio R_{lm}, on the order of 0.1, were actually measured even for those inter-sensor paths not crossing the defect region. This was likely due to variations in the experimental conditions and setups between the two experiments (undamaged and damaged case) which took place one day apart such as: 1) small errors in the repositioning of the ND-YAG laser when attempting to excite the same location of 25 secondary sources used for DFI and 2) small shifts in the alignment of the scanning grid of the SLDV (after having stuck the screw on the plate) and 3) small temporal changes of the actual Green's function in the plate (e.g. due to temperature changes) occurring between the two experiments. Hence only significant measurements of R_{lm}<0.9 were kept for a linear Bayesian tomography inversion scheme [Tarantola, 1987] for reconstructing the local plate attenuation α.

The average background attenuation α_0 =0.1m^{-1} was determined from the median value of the measured quantities γ_{lm} / L_{lm}. The local attenuation coefficient α(i) (m^{-1}) was assumed to be constant over each of grid cell #i. If $\boldsymbol{\gamma}$ is the column vector of cumulated decay estimated γ_{lm} from the cross-correlation time-function (with respect to the background attenuation α_0), $\boldsymbol{\alpha}$ is the column vector of the local attenuation coefficient α(i) at each grid cell #i, and assuming a simple linear model for the cumulated decay with propagation distance, the inversion problem reduces to:

$$\boldsymbol{\gamma} = \Phi\, \boldsymbol{\alpha}, \tag{22}$$

where Φ is the forward mapping matrix (or kernel) indicating for each particular straight A_0 paths its length across each crossed cell grids. The measurement-error covariance matrix Σ_T was defined as a diagonal matrix with elements $\sigma_T^2 = 0.2$ (m^{-1}) corresponding to a low a-priori measurement error of the cumulated decay given the high SNR for all

computed cross-correlation time functions. The elements of the a-priori error covariance matrix of the cell slowness Σ_s values are:

$$\Sigma_s(i,j) = \sigma_s^2 \exp(-D_{i,j}/L) \tag{23}$$

where $\sigma_s=2m^{-1}$ is the a-priori (large) variance in local attenuation, $D_{i,j}$ is the distance (in cm) between the center of the i^{th} and j^{th} grid cell and L=4mm is a smoothness scale selected to extend over 2 grid cells (i.e. slightly smaller to the sensor grid's vertical spacing). The a-priori attenuation vector $\boldsymbol{\alpha_0}$ was set to have constant elements $\boldsymbol{\alpha_0}(i)= \alpha_0$ over all grid cells. The maximum a-posteriori solution $\boldsymbol{\alpha}$ (attenuation vector) for the linear problem defined by Eq. (22) is then:

$$\boldsymbol{\alpha} = \boldsymbol{\alpha_0} + (\Phi^t \Sigma_T^{-1} \Phi + \Sigma_S^{-1})^{-1} \Phi^t \Sigma_T^{-1} (\boldsymbol{\gamma} - \Phi \boldsymbol{\alpha_0}). \tag{23}$$

where the superscript "t" indicates a transpose matrix.

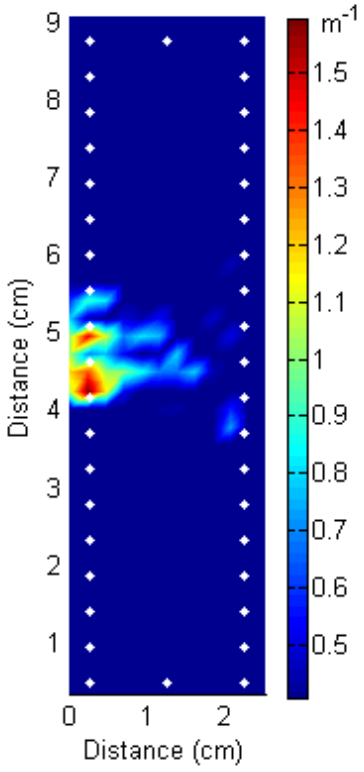

FIGURE 44: Tomographic reconstruction of the local attenuation coefficient in the presence of a simulated attenuating defect (see Fig. 29).

Figure 44 shows the reconstructed variations of the local attenuation coefficient obtained from the maximum a-posteriori solution (see Eq. (23)) [Tarantola 1987], which produces a residual variance reduction of 93% relative to the residual for the homogenous model. The high attenuation values clearly correspond to the defect region (see Fig. 29.a). But, only the rim of the (nearly) circular defect is mapped correctly with this simple linear tomographic reconstruction and the interior of the circular defect perturbation remains invisible. This likely occurs since the wavelength of the A_0 mode (~1cm here) is comparable to the defect size (estimated defect size 1.5cm) and thus only the rim of the defect acts as attenuation perturbation here [Fichtner et al. 2006].

4.3 Conclusion

This chapter has thus demonstrated the potential of the DFI technique. Indeed, the detection of the simulated damage (see Fig. 35) demonstrates that variations of the amplitude of the Green's function can also be correctly estimated from DFI. Furthermore, when implemented with a distributed sensor array (e.g. scanning grid of the SLDV), the performance of DFI originates from the high density of cross paths between all sensor pairs obtained with a minimal number of sources, thus potentially minimizing the power consumption. Hence DFI could be used for remote monitoring and tomographic reconstruction of structural hot spots.

CHAPTER 5

INFLUENCE OF THE BOUNDARY CONDITIONS

It should be noted that DFI relies on the spatial correlation of diffuse fields generated by one (or several) diffuse source recorded simultaneously between a pair of sensors. Hence, the extracted coherent waveforms from DFI are only sensitive to the local properties of elastic medium itself between the sensors and not to the precise source characteristics. For instance, when implementing DFI in a large plate with two sensors in its center, the first coherent arrivals (e.g. A_0 or S_0 guided modes on a plate) obtained from DFI are not sensitive to small changes in boundary conditions far from the sensors (similar to conventional active SHM results) even though the original recorded diffuse field are, since they may sample those boundaries. This ensures a good repeatability and robustness of the DFI output for practical SHM implementation.

Hence, DFI fundamentally differs from other active sensing techniques for diffuse fields; for instance, measuring how diffuse fields (e.g. coda waveforms) between a single source and single receiver pair change over time with respect to a reference waveform [Snieder et al. 2002; Lobkis and Weaver 2003; Michaels and Michaels 2005; Lu and Michaels 2006]. As opposed to DFI, these techniques: 1) are based on the temporal coherence of the medium, 2) are sensitive to global changes of the elastic medium but yet do not provide local information between sensors and 3) require a calibrated and highly repetitive elastic source and stable experimental setup in order to minimize potential artifacts due to changes in source excitation or mounting conditions when trying to detect actual changes of the propagating medium itself.

A study of the influence of boundary conditions on the cross-correlation obtained from DFI is exposed in this last chapter.

5.1 Presentation of the experiment

To evaluate the influence of the boundary conditions on the recorded data, experiments were conducted on the same plate as previously on which some more slots had been cut on two more edges. The influence of the mounting had been evaluated by comparing the exact same setup with two different mountings: the first one had two mounts on each side of the plate (see Fig. 45.a), and for the second one, the right side mount had been carefully removed so that the plate and the grid does not move between the two experiments and thus only the left one was remaining (see Fig. 45.b). The same ND-YAG laser used in the two previous experiments (see Chapter 4) was exciting the plate at three different locations (#1 and #3 were 9.1cm apart and #1 and #2 were 6.5cm apart), and the SLDV was recording the answers following a pre-defined grid of 323 points as shown on both figures hereunder.

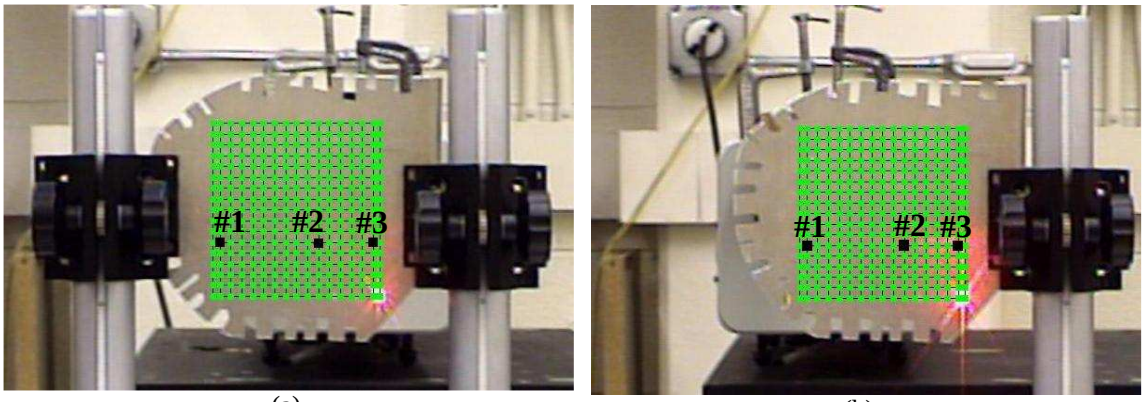

(a) (b)

FIGURE 45.a: Plate held with two mounts, excited once at a time at three different locations (#1, #2 and #3). The grid is constituted of the 323 points. The square pixel size is 0.65 cm. **45.b:** Plate held with one mount, the same left one as in Figuremount2, excited once at a time at three different locations (#1, #2 and #3). The grid is constituted of the 323 points.

The propagation of the waves into the plate can be represented in a RMS picture as shown in Fig. 46. Figure 46 illustrates the answer of the plate to a laser excitation at #1 when the plate was held by two mounts. The first arrivals are in red.

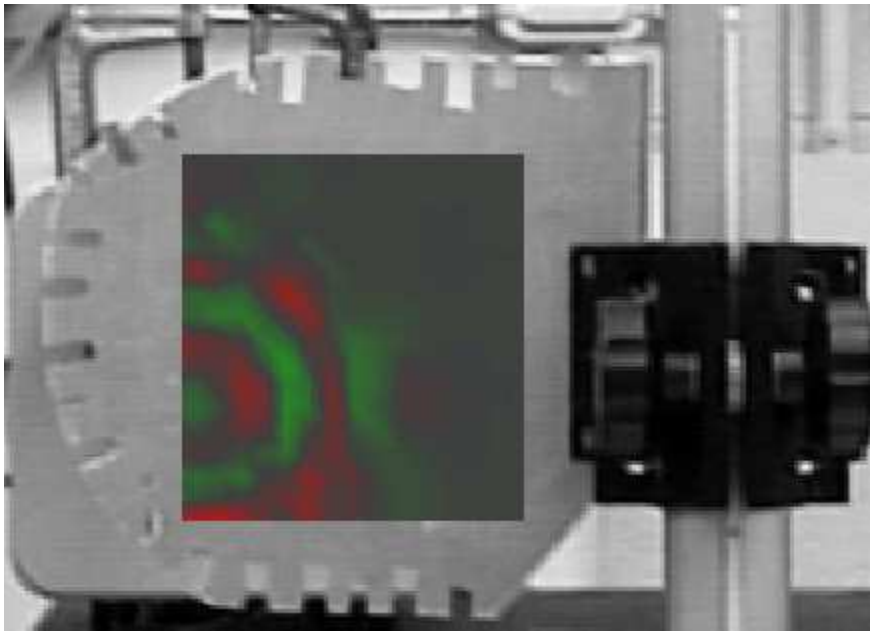

FIGURE 46: RMS field on the pre-defined grid when the laser was hitting location #1 on the plate. In red are the energetic first arrivals.

Then the same process to dismiss the bad recorded signals had been performed here by comparing the standard deviation of the pre-trigger signal to the median one overall the 323 points, and after this 308 points were remaining.

5.2 Experimental results

The signals at impact #1 recorded after each impact #1, #2 and #3 and their FFT are respectively plotted on Fig. 46. As expected, the propagation time of the first impulse from the point of impact of the laser to the point #1 increases proportionally with the distance. Indeed the time of the first maximum for the three cases are respectively

t_0^1= 0.271ms, t_0^2=0.3ms, t_0^3=0.313. Moreover, the FFT of these signals are comparable and as the two previous experiments on a wide bandwidth, which will allow to study on the signal on different frequency bandwidth (see next section).

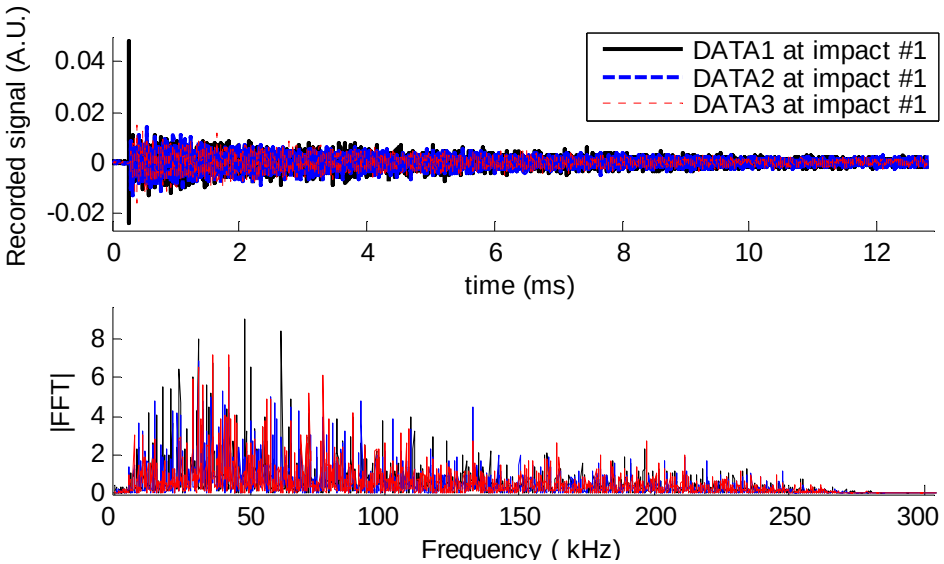

FIGURE 47.a: Waveforms collected by the SLDV on the plate held by one mount at impact #1 following a laser impulse at impact #1, #2 and #3 respectively. There is a delay between the three signals, which represents the traveling time of a wave from impact #1 to impact #2 and to impact #3. The waveform shows also a long "coda" caused by the multiple reflections on the edges. **47.b:** FFT of the recorded signals: B=[5-280] kHz.

Then the recorded signals had been filtered in different frequency bandwidth B_1=[50-90]kHz and B_2=[50-150]kHz (same as previous studies) and clipped at 25NL, but no constraint on the length of the signal had been applied. So that the signals compared with one or two mounts did not have the same recording duration: in B_1, T_1^{1mount} = 5.6ms and T_1^{2mount} = 4.2ms; in B_2, T_2^{1mount} = 7.5ms and T_2^{2mount} = 5.5ms. On these two frequency bandwidth, the estimates of the GF had been evaluated for both setups and compared for the three combinations of points: $G_{12}(t)$ (see Fig. 48), $G_{23}(t)$ (see Fig. 49), and finally $G_{13}(t)$ (see Fig. 50).

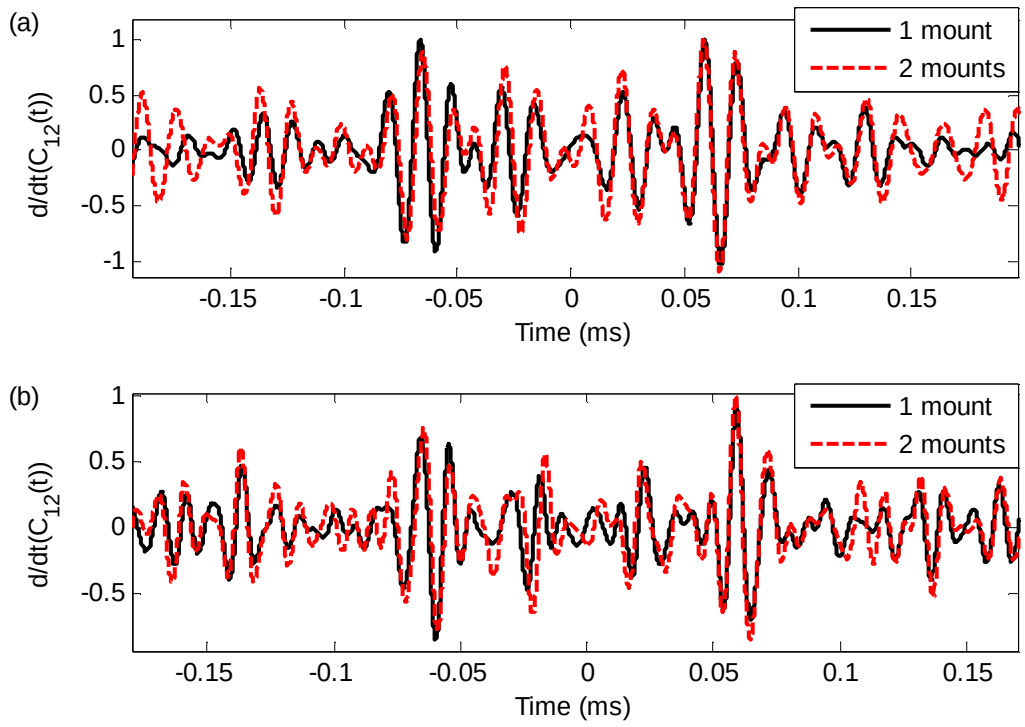

FIGURE 48: Comparison of the estimate of the GF: $G_{12}(t)$ between #1 and #2 with one (solid line) or two (dashed line) mounts **48.a:** filtered in B_1=[50-90]. **48.b:** filtered in B_2=[50-150].

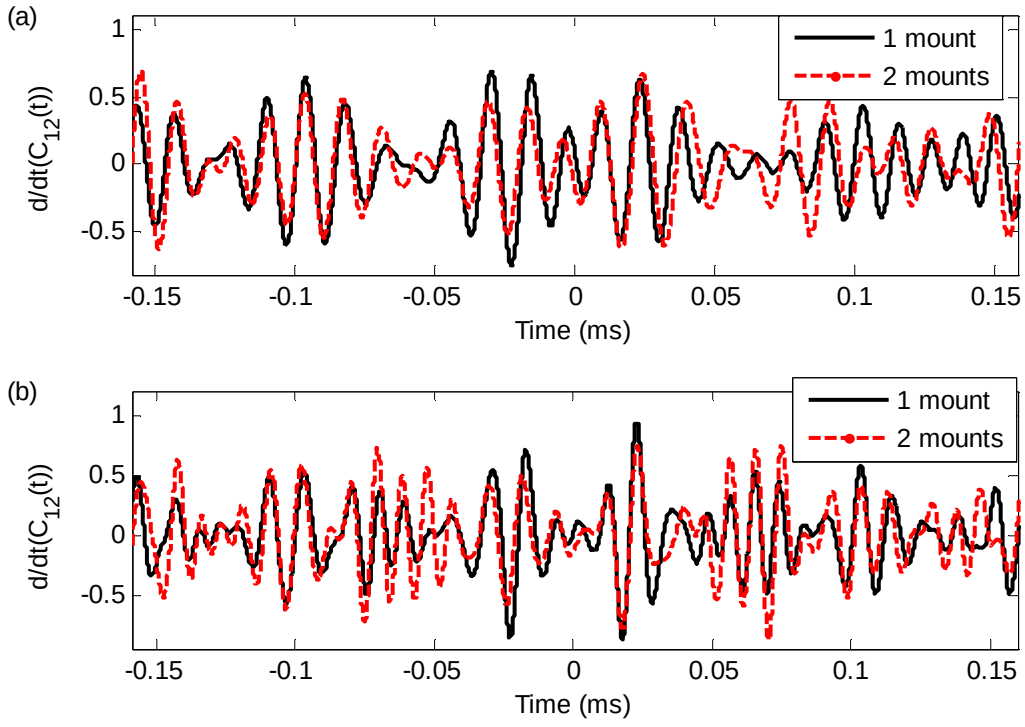

FIGURE 49: Comparison of the estimate of the GF: $G_{23}(t)$ between #2 and #3 with one (solid line) or two (dashed line) mounts **49.a:** filtered in B_1=[50-90]. **49.b:** filtered in B_2=[50-150].

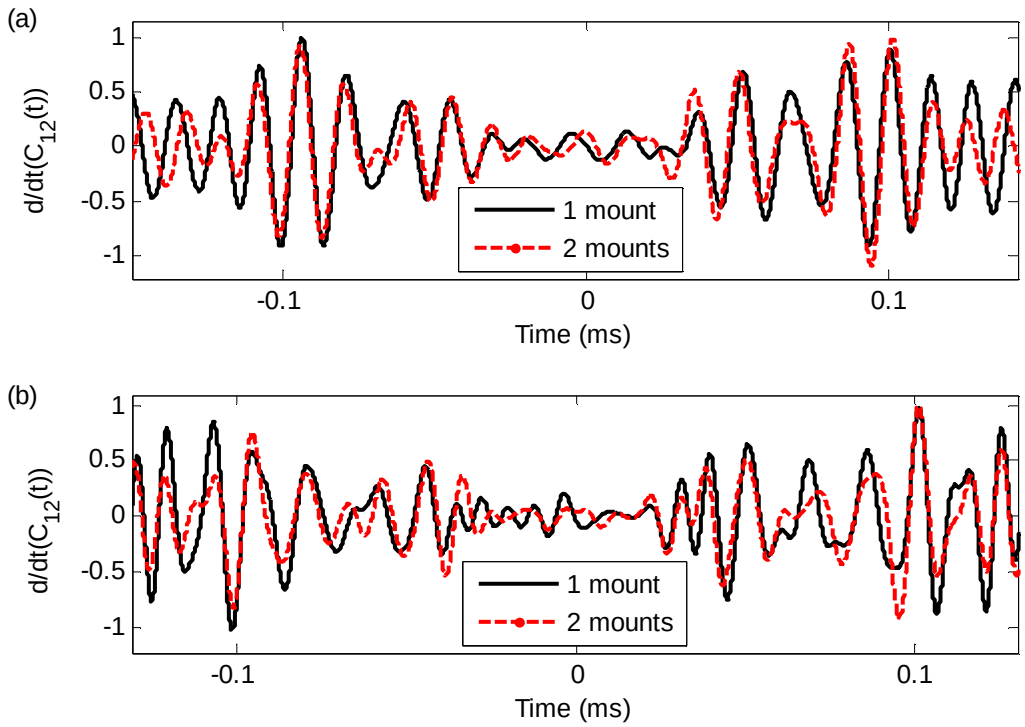

FIGURE 50: Comparison of the estimate of the GF: $G_{13}(t)$ between #1 and #3 with one (solid line) or two (dashed line) mounts **50.a:** filtered in B_1=[50-90]. **50.b:** filtered in B_2=[50-150].

Even if there are some discrepancies in amplitude, the phase of the first arrival is conserved between the two experiments as shown in Fig. 48-50, and this independently of the frequency bandwidth. However, the correlation waveforms seem to be slightly better reconstructed in the larger frequency bandwidth B_2=[50-150].

The errors between the A_0 arrival times for each pair of points on each frequency bandwidth had been computed and are given in Table 2 (more detailed values are given in Appendix A).

TABLE 2: Error between the arrival times for each case.

t_0^{1mount} vs. $t_0^{2mounts}$	**#1-#2**	**#2-#3**	**#1-#3**
[50-90]kHz	5%	0.9%	0.7%
[50-150]kHz	3.5%	0.7%	0.6%

The results of Table 2 are good, and lead to a good approximation of the phase velocities for the three couple of points studied here. Indeed, knowing the distances separating the three points, the phase velocities had been evaluated to be in accordance with the previous experiments with a mean value over the three phase velocities of C_p=1030m/s.

5.3 Conclusion

The results of this experiment confirm that the DFI technique allow a great freedom on the setup of the experiments and that the computation of the first coherent arrivals and thus the reconstruction of the estimate of the Green's function are not sensitive to small changes in boundary conditions far enough from the sensors.

CHAPTER 6

CONCLUSION

The Diffuse Field Interferometry technique investigated in this thesis has the potential to expand and improve SHM system applications since it allows transforming a simple receiver into a virtual elastic source using only cross-correlations of the signals recorded from a limited number of secondary sources which are remotely located from the sensing region. Theoretical predictions of the signal-to-noise ratio of the coherent waveforms extracted from DFI in the presence of incoherent measurement noise were developed using a simple model for the exponentially decaying reverberant wavefield. The performances of the DFI technique were also investigated experimentally based on cross-correlations of the multiply scattered wavefield measurements collected over a thin aluminum plate with complex geometry and boundaries, in the frequency bandwidth [4-90]kHz using a scanning SLDV. Estimates of the A_0 lamb wave component as well as coda waves arrivals of the local Green's function propagating between two arbitrary locations on the plate were extracted from DFI. Hence this highlights the robustness of DFI for estimating the full Green's function (i.e. ballistic and coda arrivals) locally using only passive sensors, in agreement with previous findings [Weaver et al., 2005; Sabra et al. 2006; Larose et al. 2008].

The coherent *SNR* of the Green's function estimates obtained from DFI sets the achievable accuracy for damage detections between a pair of passive sensors (e.g. for detecting the weak scattered field from a local crack). Hence theoretical predictions or

experimental determination of the dependency of the coherent *SNR* on independent parameters that the operator can potentially control -such as the recordings duration *T*, the number of secondary sources *N* or signal-to-noise ratio of the selected portion of the recorded waveforms- can be used to quantify the probability of detection of the SHM systems used to inspect the structure of interest [Achenbach 2000]. An extensive parametric analysis of the DFI performances was conducted experimentally and yielded the following findings: 1) the coherent SNR of the cross-correlation waveforms can be improved by using amplitude clipping of the recorded reverberant wavefield as long as the selected threshold remains higher than the noise level (NL) of the measurements (around 15NL for optimal results), carefulness should be used especially when using late coda portion of the reverberant wavefield, 2) the SNR is barely influenced by the spatial configuration of the secondary ultrasonic sources for small number of sources and by the boundary conditions applied to the plate, as long as the recorded field is diffused in the entire structure, as expected from previous numerical simulations [Larose et al. 2008], 3) a selected value of the coherent *SNR* can be optimally achieved with a certain combination of the parameters *T* and *N*. However an increase in recording duration *T* can not always compensate for a lack of secondary sources when using noisy multiply scattered signals, 4) late coda arrivals contain also “coherent information”, and thus an accurately reconstruction of the Green’s function is feasible. However, the influence of incoherent measurement noise (e.g. sensor noise) is higher on these late arrivals, which limits their use in the improvement of the DFI performances.

Furthermore, even if this technique offers good potentialities of retrieving an accurate

estimate of the true Green's function between two sensors, the performance of DFI can be limited by the geometry and material properties of the structure of interest: 1) as just stipulated, the incoherent measurement noise has to be much lower than the amplitude of the signals to allow the theory to be applicable. Great efforts have then to be done to reduce the ambient noise during the experimental recordings. 2) Moreover, highly disordered media have to be avoided as they allow the existence of closed loops or recurrent scattering. Thus adding too many slots on the plate can have detrimental effects on the performances of the DFI technique. 3) The reconstruction of the Green's function from DFI does not require necessarily high number of sources, however a quite substantial number (~100) is needed to lead to a good estimate of the phase and group velocities of the A_0 mode on this thin plate. This requirement on high number of secondary sources may result both from the presence of strong elastic attenuation (which increases the temporal decay of the diffuse field and thus limits the effective duration of the diffuse field record) and the small number of propagating modes in this plate at low frequencies (mainly S_0 and A_0 modes here at 50kHz).

Despites this, the theory works well when using the diffuse part of the signal to extract the local field Green's function. Especially as shown by the results of the detection of the simulated defect. Indeed, the experiment without damage had demonstrated the proposed DFI technique provides an estimate of the local GF between any pair of monitored points. Hence DFI provides a mean for local estimation of the monitored structure, which is easy to interpret and free from aberrations introduced by the source, from the effects of multiple reflections and distortions caused by structural

and material complexity often encountered in typical aircraft components. The experiment with damage illustrated the precise detection and localization of a damping defect with DFI using only passive sensors and no a-priori information. The use of a distributed sensor array (e.g. scanning grid of the SLDV) allows a precise tomographic reconstruction of structural hot spots. However the damping effect of the simulated defect did not allow the use of a time-reversal technique to detect it.

It will be interesting in the future to look at the performances of the DFI technique onto the detection of a scattering defect. However, the setup of this experiment will need great care to reduce significantly the incoherent measurement noise, to be able to notice the scattering effect of the defect. Once done, the great potential of the DFI technique in the monitoring of defect location will be definitely proven.

In closing, this thesis confirms that a great amount of information can be found from the diffuse part of a signal including the fact that, by cross-correlating the diffuse part of the signal, an estimate of the local field's Green's function can be extracted. As stated earlier, this can be very useful for analyzing aircraft fuselage and wing structures. These methods and the resulting Green's functions have the potential to facilitate significant application for passive and real-time Structural Health Monitoring to detect, locate, and quantify damage in structures.

APPENDIX A

MATLAB CODE

CODE TO LOAD THE RECORDED DATA

```
%=========================================================================
%Correlation Plaque
%=========================================================================
clc
clear all
close all
format compact

n=3; % number of DATA recorded
c=['ko','bo','ro'];
c1=['k','b','r'];
f1=fullfile('C:','Documents and Settings', 'Adelaide','My
Documents','Adelaide','LASER_TEST_09_16_08','2mounts');
f1=fullfile('Specific directory');
cd(f1)


Nn=[0,1:n];
%Objective #ii: Load and Arrange Data. First Actuator
for ii=Nn;
    ii
    if (ii==0) v=genvarname('DATA', who); eval([v ' =0;']);
    else
    cd(['pt',num2str(ii)])
    load('TH.mat');
    v=genvarname('DATA', who);
    eval([v ' =TH;']);
    co = load('xyz.mat');
    load ('raw_conn_data.mat');
    cd(f1)
    end

end
clear v
clear DATA

 %conn_data.geom.array; CM=ans; d=CM(:,[1 2 3 4])';
d=grid_r(:,[1 2 3 4])';
time=time_val;
Ts=time(2)-time(1) % sampling time

clear TH* %%pour faire la place

%Create Coordinate Matrix of xyz positions (co.x signifies the
structure)
%
```

```
CO=[co.x' co.y' co.z'];
xx = CO(:,1); yy = CO(:,2); zz = CO(:,3);
cd(f1)

%Drawing the grid and finding the excited points on it
figure(2);clf;
patch(xx(d),yy(d),zz(d)); hold on
axis equal

[x,y]=ginput(n);

for ii=1:1:length(x)
ii

    for jj=1:1:size(DATA1,2)
        D(jj)=sqrt((xx(jj)-x(ii)).^2+(yy(jj)-y(ii)).^2);
        [M,K(ii)]=min(D);

   end

end
K
X=xx(K);
Y=yy(K);

save K K

%Drawing the impact points on the grid
figure(4);clf;
patch(xx(d),yy(d),zz(d)); hold on
for ii=1:length(K)

    plot(xx(K(ii)),yy(K(ii)),c(2*ii-1:2*ii),'linewidth',5); hold on
end
axis equal
saveas(figure(1),'01- Location of impact points on plate')


%%%%%%%%%%%%%%%%%%%%%%%%%%%%%%%%%%%%%%%%%%%%%%%%%%%%%%%%%%%%%%%%%%%%%%%%%%%%
Fe=1/Ts; %sampling frequency
N=length(DATA1); % number of sample
freq=[0:N-1]/N/Ts;

%%%%%%%%%%%%%%%%%%%%%%%%%%%%%%%%%%%%%%%%%%%%%%%%%%%%%%%%%%%%%%%%%%%%%%%%%%%%
%%PLot one received data

for ii=1:n;%Choisis un des points
ii
figure(ii);clf;hold on
    for jj=1:n
        s=['DATA',num2str(jj)];
        D=eval(s);

        subplot(2,1,1);hold on
```

```
        %Temps
        plot( time*10^3,D(:,K(ii)),c1(jj));hold on
        xlabel('time (ms)','fontsize',10)
        ylabel('Velocity (A.U.)','fontsize',10)
        title(['DATAs at impact #', num2str(ii), ' and their
fft'],'fontsize',10)

        subplot(2,1,2);hold on %Frequence
        plot(freq,abs(fft(D(:,K(ii)))),c1(jj)); hold on
        xlabel('Frequency (Hz)','fontsize',10)
        ylabel('Spectrum','fontsize',10)
        clear s
        clear D
    end
    subplot(2,1,1);
    legend(['DATA1 at impact #', num2str(ii)],['DATA2 at impact #',
num2str(ii)],['DATA3 at impact #', num2str(ii)])
    saveas(figure(ii),['0',num2str(ii+2),'- DATAs at impact #',
num2str(ii), ' and their fft'])
end

%%%%%%%%%%%%%%%%%%%%%%%%%%%%%%%%%%%%%%%%%%%%%%%%%%%%%%%%%%%%%%%%%%%%%%%
%%Elimination of the signal with a std of the pre-trigger
%%%signal or the tail of the signal too high i.e. with a electric noise
too high
%%% in order to improve the SNR

%Objective #ii: Load and Arrange Data. First Actuator
for ii=Nn;
    ii

    if (ii==0) v=genvarname('NOISE', who); eval([v ' =0;']);
v1=genvarname('NOISElevel', who); eval([v1 ' =0;']);
    else
    s=['DATA',num2str(ii)];
    D=eval(s);
    v=genvarname('NOISE', who);
    eval([v ' =std(D(1:600,:));']);
    v1=genvarname('NOISElevel', who);
    eval([v1 ' =(median(std(D(1:600,:),0,1)));']);
    clear s D
    end

end

clear NOISE NOISElevel

figure(5);clf;hold on
for ii=1:n;
    s=['NOISE',num2str(ii)];
    D=eval(s);
    plot3(xx,yy,D,c(2*ii-1:2*ii));
end
saveas(figure(5),'06- Ambient NOISE through the plate')
```

```
KK=zeros(1,size(DATA1,2));
for ii=1:n;
    s=['NOISE',num2str(ii)];
    D=eval(s);
    s1=['NOISElevel',num2str(ii)];
    for jj=1:size(DATA1,2);
        if (D(:,jj)>3*eval(s1)) KK(jj)=jj; %DATA(:,ii)=0;%
        end
    end
end

%%%%%%%%%%%%%%%%%%%%%%%%%%%%%%%%%%%%%%%%%%%%%%%%%%%%%%%%%%%%%%%%%%%%%%%%%%%%
%%%% Reordering of none dismissed signals
L1=1:size(DATA1,2);
L1=L1-KK;
L1=sort(L1);

ZEro=find(L1==0);
ZEro=length(ZEro);

L=zeros(1,size(L1,2)-ZEro);
for jj=ZEro+1:size(KK,2);
      L(1,jj-ZEro)=L1(1,jj);
end

Ll=size(L,2);
Ll=randperm(Ll);
Ll=L(Ll);

save Ll Ll

%Location of the remaining points
figure(6);clf;
patch(xx(d),yy(d),zz(d)); hold on
plot(xx(Ll),yy(Ll),'bd','linewidth',3); hold on
for ii=1:length(K)
    plot(xx(K(ii)),yy(K(ii)),'ko','linewidth',5); hold on
end
axis equal
saveas(figure(6),'02- Location of remaining points')

tcorr=[-(N-1):(N-1)]*Ts;
Ipos=find(tcorr>=0);
Ineg=find(tcorr<=0);
tpos=tcorr(Ipos);
Nc=2*N-1;
freqC=[0:Nc-1]/Nc/Ts; %% axis of the correlation frequency

tfin=[-(N-1):0.1:(N-1)]*Ts; % redefined time axis
Iposfin=find(tfin>=0);
Inegfin=find(tfin<=0);
tposfin=tfin(Iposfin);
tnegfin=tfin(Inegfin);
Tsfin=Ts/10;
Nfin=(length(tfin)-1)/2;
```

CODE TO DO THE DIFFUSE FIELD ANALYSIS

```
%=========================================================================
%Diffuse field analysis
%=========================================================================

%% %%%%%%%%%%%%%%%%%%%%%%%%%%%%%%%%%%%%%%%%%%%%%%%%%%%%%%%%%%%%%%%%%%%%
%%%%%%% Selection of points only in the middle of the plate
%%i.e. eliminating the points on the edges

figure(2);clf;
patch(xx(d),yy(d),zz(d)); hold on
axis equal

[x,y]=ginput(4);

for ii=1:1:length(x)
ii

    for jj=1:1:size(DATA1,2)
        D(jj)=sqrt((xx(jj)-x(ii)).^2+(yy(jj)-y(ii)).^2);
        [M,K(ii)]=min(D);

   end

end
K
X=xx(K);
Y=yy(K);

save X X
save Y Y

% load X.mat
% load Y.mat

KK=zeros(1,size(Ll,2));
for ii=1:length(Ll);

if((xx(Ll(ii))>=X(4))&&(yy(Ll(ii))<=Y(1))&&(xx(Ll(ii))<=X(2))&&(yy(Ll(i
i))>=Y(3)))  KK(ii)=Ll(ii);
    end
end

KK=sort(KK);
ZEro=find(KK==0);
ZEro=length(ZEro);

L=zeros(1,size(KK,2)-ZEro);
for jj=ZEro+1:size(KK,2);
      L(1,jj-ZEro)=KK(1,jj);
end

LL=size(L,2);
```

```
LL=randperm(LL);
LL=L(LL);

clear L ZEro

save LL LL


figure(2);clf; hold on
patch(xx(d),yy(d),zz(d)); hold on
plot(xx(LL),yy(LL),'.b','markersize',15)
plot(xx(K),yy(K),'.k','markersize',30)
plot(xx(261),yy(261),'.r','markersize',30)
saveas(figure(2),'01-selected points on the plate')

%% %%%%%%%%%%%%%%%%%%%%%%%%%%%%%%%%%%%%%%%%%%%%%%%%%%%%%%%%%
%%% getting the envelope of DATA1 and DATA2
tmp2=zeros(size(DATA2(:,LL)));
for ii=1:size(LL,2);
    tmp2(:,ii)=abs(hilbert(DATA2(:,LL(ii))));
    tmp2(:,ii)=smooth(tmp2(:,ii),1500);
end

tmp1=zeros(size(DATA1(:,LL)));
for ii=1:size(LL,2);
      tmp1(:,ii)=abs(hilbert(DATA1(:,LL(ii))));
      tmp1(:,ii)=smooth(tmp1(:,ii),1500);
end

save tmp2 tmp2
save tmp1 tmp1


%%%%%%%%%%%%%%%%%%%%%%%%%%%%%%%%%%%%%%%%%%%%%%%%%%%%%%%%%%%%
%% %Computation of the mean, std on time-windows of the same length
%%%T/35
% load ENV.mat
% load ENV1.mat

T=length(tmp1)/35;
T=floor(T);

%% %%%%%%%%%%%%%%%%%%%%%%%%%%%%%%%%%%%%%%%%%%%%%%%%%%%%%%%%%%%%%%%%%
%%%%%%%%%%On the 1st intervalle:
Mean1=mean(tmp(1:1:T,:));
Mean11=mean(tmp1(1:1:T,:));

STD1=std(Mean1)/mean(Mean1);
STD11=std(Mean11)/mean(Mean11);

%%%%%%%%%%%%%%%%%%%%%%%%%%%%%%%%%%%%%%%%%%%%%%%%%%%%%%%%%%%%%%%%%%%
%%%%%%%%%%On the 2nd intervalle:
Mean2=mean(tmp(T:1:2*T,:));
Mean12=mean(tmp1(T:1:2*T,:));
```

```
STD2=std(Mean2)/mean(Mean2);
STD12=std(Mean12)/mean(Mean12);

…

%%%%%%%%%%%%%%%%%%%%%%%%%%%%%%%%%%%%%%%%%%%%%%%%%%%%%%%%%%%%%%%%%%%%%%%%%%%%
%%%%%%%%%%On the 34th intervalle:
Mean234=mean(tmp(33*T:1:34*T,:));
Mean134=mean(tmp1(33*T:1:34*T,:));

STD234=std(Mean234)/mean(Mean234);
STD134=std(Mean134)/mean(Mean134);

%%%%%%%%%%%%%%%%%%%%%%%%%%%%%%%%%%%%%%%%%%%%%%%%%%%%%%%%%%%%%%%%%%%%%%%%%%%%
%%%%%%%%%%On the 35th intervalle:
Mean235=mean(tmp(34*T:1:35*T,:));
Mean135=mean(tmp1(34*T:1:35*T,:));

STD235=std(Mean235)/mean(Mean235);
STD135=std(Mean135)/mean(Mean135);

%%%%%%%%%%%%%%%%%%%%%%%%%%%%%%%%%%%%%%%%%%%%%%%%%%%%%%%%%%%%%%%%%%%%%%%%%%%%
%%%%%%%%%%On the 36th intervalle:
Mean236=mean(tmp(35*T:1:end,:));
Mean136=mean(tmp1(35*T:1:end,:));

STD236=std(Mean236)/mean(Mean236);
STD136=std(Mean136)/mean(Mean136);

%%%%%%%%%%%%%%%%%%%%%%%%%%%%%%%%%%%%%%%%%%%%%%%%%%%%%%%%%%%%%%%%%%%%%%%%%%%%
%%%%%%%%%%%%%%%%%%%%%%%%%%%%%%%%%%%%%%%%%%%%%%%%%%%%%%%%%%%%%%%%%%%%%%%%%%%%
%%%%%%%%%%%%%%%%%%%%%%%%%%%%%%%%%%%%%%%%%%%%%%%%%%%%%%%%%%%%%%%%%%%%%%%%%%%%
Meanact1=[Mean11; Mean12 ;Mean13; Mean14; Mean15; Mean16;Mean17;
Mean18;Mean19;...
    Mean110; Mean111;Mean112;Mean113; Mean114;Mean115;Mean116;...
    Mean117;Mean118;Mean119; Mean120;Mean121;Mean122;Mean123;
Mean124;Mean125;Mean126;...
    Mean127;Mean128;Mean129; Mean130;Mean131;Mean132;Mean133;
Mean134;Mean135;Mean136];

Meanact2=[Mean1; Mean2;Mean3;Mean4; Mean5;Mean6;Mean7; Mean8;Mean9;...
    Mean10; Mean211;Mean212;Mean213; Mean214;Mean215;Mean216;...
    Mean217;Mean218;Mean219; Mean220;Mean221;,Mean222;Mean223;
Mean224;Mean225;Mean226;...
    Mean227;Mean228;Mean229; Mean230;Mean231;Mean232;Mean233;
Mean234;Mean235;Mean236];

save Meanact1 Meanact1
save Meanact2 Meanact2

STDact2=[STD1,STD2,STD3,STD4,STD5,STD6,STD7,STD8,STD9,...
    STD10,STD211,STD212,STD213,STD214,STD215,STD216,STD218,...
    STD219,STD220,STD221,STD222,STD223,STD224,STD225,STD226,...
```

```
    STD227,STD228,STD229,STD230,STD231,STD232,STD233,STD234,...
    STD235,STD236];

STDact1=[STD11,STD12,STD13,STD14,STD15,STD16,STD17,STD18,STD19...
    ,STD110,STD111,STD112,STD113,STD114,STD115,STD116,STD118...
    ,STD119,STD120,STD121,STD122,STD123,STD124,STD125,STD126...
    ,STD127,STD128,STD129,STD130,STD131,STD132,STD133,STD134...
    ,STD135,STD136];

save STDact2 STDact2
save STDact1 STDact1

figure(1);clf;
plot(time([1:length(STDact1(1:end-1))]*T)*1000,STDact1(1:end-
1),'k','linewidth',2); hold on
plot(time([1:length(STDact2(1:end-1))]*T)*1000,STDact2(1:end-
1),'r','linewidth',2)
xlabel('Time (ms)')
ylabel('Energy level')
legend('act1','act2','Location','Best')
saveas(figure(1),'02-Energy level')

figure(3);clf;
plot3(xx(LL),yy(LL),Meanact1(1,:),'bo');hold on
plot3(xx(LL),yy(LL),Meanact2(1,:),'*r');hold on
zlabel('Mean on the 1st interval of time ')
legend('Mean for DATA act1','Mean for DATA act2','Location','Best')
saveas(figure(3),'04-Mean on the first interval of time')

figure(4);clf;
plot3(xx(LL),yy(LL),Meanact1(25,:),'bo');hold on
plot3(xx(Ll),yy(LL),Meanact2(25,:),'*r');hold on
zlabel('Mean on the 25th interval of points ')
legend('Mean for DATA act1','Mean for DATA act2','Location','Best')
saveas(figure(4),'05-Mean on the 25nd interval of time')
```

CODE TO FIT THE RECORDED SIGNALS TO A DECAYING EXPONENTIAL

```
f3=fullfile(f1, 'directory');
cd(f3)

load tmp
load tmp1
load Meanact1
load Meanact2
load STDact2
load STDact1
load LL

%%
ii=261
jj=find((LL>=261)&(LL<=261));
figure(7);clf;
plot(time*1000,DATA1(:,ii),'r');hold on
plot(time*1000,DATA2(:,ii),':b');hold on
plot(time*1000,tmp1cut(:,jj),'g','linewidth',2);hold on
plot(time*1000,tmp2cut(:,jj),':k','linewidth',2);hold on
xlabel('time (ms)')
ylabel('Recorded signals and their envelopes at the middle point')
legend('Act1 #middle point','Act2 #middle point','Envelope act1 #middle
point','Envelope act2 #middle point')
saveas(figure(7),'07-Recorded signals and their envelopes at the middle
point')

%%
T=length(time)/35;
T=floor(T);
X=[9*T:1:29*T];
ENV=zeros(size(tmp));
ENV=tmp(X,:);
ENV1=tmp1(X,:);
Tfinal=time(X(end));
Xfinal=ENV1(end,jj);
xdata=time(X);
%% first estimation of x0
figure(8);clf;
plot(time*1000,tmp1(:,jj),'b','linewidth',1);hold on
plot(xdata*1000, Xfinal*exp(-220*(xdata-Tfinal)),'g');
% plot(time*1000,0.0004*exp(-210.0059*(time-0.0155)));
xlabel('time (s)')
ylabel('DATAs envelope')
legend('envelope #350','fit sur tmp(X):0.0002*exp(-210.0083*(t-
0.0183))','fit sur tmp:0.0004*exp(-210.0059*(time-0.0155))')

%%
x0=[ Xfinal 220];

for ii=1:size(ENV1,2);
    xs1(ii,:)=lsqcurvefit(@FITT,x0,xdata,ENV1(:,ii));
    xs(ii,:)=lsqcurvefit(@FITT,x0,xdata,ENV(:,ii));
end
```

```
save xs1 xs1
save xs xs


F1=xs1(jj,1).*exp(-xs1(jj,2).*(time-xdata(end)));
F=xs(jj,1).*exp(-xs(jj,2).*(time-xdata(end)));


figure(9);clf;hold on
plot(time*1000,tmp1(:,jj),'b');hold on
plot(time*1000,F1,'g');
plot(time*1000,tmp(:,jj),'r');hold on
plot(time*1000,F,'k');
plot(time(9*T)*1000,0:0.0003:tmp1cut(9*T,jj),'+k','linewidth',1)
plot(time(29*T)*1000,0:0.0003:tmp1cut(29*T,jj),'+k','linewidth',1)
xlabel('time (ms)')
ylabel('Envelope and its fit at the middle point between #1 and #2')
legend('envelope #middle point when #1 active','fit sur #1','envelope
#middle point when #2 active','fit sur #2')
saveas(figure(9),'08-Envelope and its fit at the middle point between
#1 and #2' )
```

where the function FITT is defined by:

```
function F = FITT(x,xdata)

F=x(1).*exp(-x(2).*(xdata-xdata(end)));
```

CODE TO FILTER AND CLIPPED THE RECORDED DATA

```
%% Filtering between F1e3 and F2e^3 and clipping at THR1 NL
F1=50;
F2=90;
THR1=25;

f4=fullfile(f1,['BF=',num2str(F1),'-',num2str(F2),'kHz clipped at
',num2str(THR1),'NL']);
if (exist(f4) == 0)
   mkdir (f4);
end
cd(f4)



%% %%%%%%%%%%%%%%%%%%%%%%%%%%%%%%%%%%%%%%%%%%%%%%%%%%%%%%%%%%%%%%%%%%%%5
%%DATA processing before
correlation%%%%%%%%%%%%%%%%%%%%%%%%%%%%%%%%%%%%5
%%%%%%%%%%%%%%%%%%%%%%%%%%%%%%%%%%%%%%%%%%%%%%%%%%%%%%%%%%%%%%%%%%%%%%%
%% Choice of the frequency
bandwidth%%%%%%%%%%%%%%%%%%%%%%%%%%%%%%%%%%%%%%%%%%%%%%%%

%BF1
Fmin=F1*10^3;
Fmax=F2*10^3;


freq_intALL=[Fmin Fmax];%%in Hz;

[BB,AA]=butter(4,[freq_intALL]/Fe*2);Fs=Fe/N;% Parameters of the passe-
band filter

%% Filtering of the recorded signals
DATA1=filtfilt(BB,AA,DATA1);
DATA2=filtfilt(BB,AA,DATA2);
DATA3=filtfilt(BB,AA,DATA3);

IND1=99
DATAref1=DATA1(:,K(1));% Choice of the references points
DATAref2=DATA2(:,K(2));
DATAref3=DATA3(:,K(3));


%% %%%%%%%%%%%%%%%%%%%%%%%%%%%%%%%%%%%%%%%%%%%%%%%%%%%%%%%%%%%%%%%%%%%%%%%
%%%Determine common Threshold estimated of the pre-trigger signal or
the
%%%tail of the signal
for ii=1:n;
    s=['NOISElevel',num2str(ii)]
    A(ii)=eval(s);
end
NOISElevel=mean(A);
```

```
THR=THR1*NOISElevel;

%%%%%%%%%%%%%%%%%%%%%%%%%%%%%%%%%%%%%%%%%%%%%%%%%%%%%%%%%%%%%%%%%%%%%%%%%%%%
%%%%%Detect THRESHOLD
DECAY=200; %%number of points for the decay
WINDOW=hanning(DECAY*2);
INDEX=1;
for jj=1:size(DATA1,2)
jj
    for Rec=[1, 2, 3];
        if Rec==1
            D1=DATA1(:,jj);
        elseif Rec==2
            D1=DATA2(:,jj);
        elseif Rec==3
            D1=DATA3(:,jj);
        end

        IIok=find(abs(D1)>=THR);
        ImaxALL(INDEX,jj)=max(find(diff(IIok)<=1));%%Prevent fomr
getting influenced by isolated spikes
        IIok=[IIok(1):IIok(ImaxALL(INDEX,jj))];

        Imax(:,jj)=IIok(end);
        Imin(:,jj)=IIok(1);
    end
end

Imax=mean(Imax);
Imin=mean(Imin);
Imax=floor(Imax);
Imin=(floor(Imin));


DECAY=200; %%number of points for the decay
WINDOW=hanning(DECAY*2);
INDEX=1;
for jj=1:size(DATA1,2)
jj
    for Rec=[1, 2, 3];
        if Rec==1
            D1=DATA1(:,jj);
        elseif Rec==2
            D1=DATA2(:,jj);
        elseif Rec==3
            D1=DATA3(:,jj);
        end

        IIok1=Imin:Imax;

        Imax=IIok1(end);
        Imin=IIok1(1);

        %%Select the part of the signal above the threshold "THR"
```

```
        TEMP=zeros(N,1);
        TEMP(IIok1)=D1(IIok1);

        %%Smooth the edges
        TEMP(Imax-DECAY+1:Imax)=TEMP(Imax-
DECAY+1:Imax).*WINDOW(DECAY+1:end);
        TEMP(Imin:Imin+DECAY-1)=TEMP(Imin:Imin+DECAY-
1).*WINDOW(1:DECAY);


        IIhigh=find(abs(TEMP)>=THR);

        %%Clip the amplitude;
        TEMP(IIhigh)=THR.*sign(TEMP(IIhigh));
        D1=TEMP;

        %Replace each line by its clipped values
        if Rec==1
            DATA1(:,jj)=D1;
        elseif Rec==2
            DATA2(:,jj)=D1;
        elseif Rec==3
            DATA3(:,jj)=D1;
        end

    end

end;


%% Compare the signals before and after clipping
for ii=1:n
    sref=['DATAref',num2str(ii)]
    s=['DATA',num2str(ii)]
    D=eval(s);
    figure(IND1-(ii));clf;
    plot(time*10^3,eval(sref),'b')
    hold on
    plot(time*10^3,D(:,(K(ii))),'r')
    ylabel(['DATA', num2str(ii), ' #', num2str(ii)],'fontsize',10)
    xlabel('time(ms)','fontsize',12)
    title(['filtered in [', num2str(F1),'-',num2str(F2),'] kHz and
clipped at ',num2str(THR1),'*NL '],'fontsize',10)
    legend(['Filtered in BF=', num2str(F1),'-
',num2str(F2),'kHz'],['Clipped at',num2str(THR1),'NL'])
    saveas(figure(IND1-(ii)),['01-DATA',num2str(ii),' at the impact
#',num2str(ii),' clipped ',num2str(THR1),'NL '])
end
```

CODE TO COMPUTE THE PERFORMANCE OF THE DFI TECHNIQUE:

BY EVALUATING THE ESTIMATE OF THE GREEN'S FUNCTION, THE SNR , THE ARRIVAL TIME AND R(N,T)

```
%%%%%%%%%%%%%%%%%%%%%%%%%%%%%%%%%%%%%%%%%%%%%%%%%%%%%%%%%%%%%%%%%%%%%%%%
%% Computation of the cross-correlation
CORR=0

for jj=1:length(Ll);
    jj
    CORR=CORR+xcorr(DATA2(:,Ll(jj)),DATA1(:,Ll(jj)));

end

CORRorig=CORR;
save CORRorig CORRorig


%% Comparison of the two definition of Correlation
figure(100);clf;hold on;
plot(tcorr*1000,CORR/max(CORR),'k')
xlim(1.5*[-1 1])
drawnow
xlabel('Time (ms)')
ylabel('C_1_2(t)')
saveas(figure(100),['01-Normalized Correlation between ',num2str(rr), '
and ', num2str(RR),...
    'BF=',num2str(F1),'-',num2str(F2),'kHz at ',num2str(THR1),'NL '])

%% reassign the time axis of the Correlation
tfin=[-(N-1):0.1:(N-1)]*Ts;
Cfin=spline(tcorr,CORRorig,tfin);
figure(101);clf;
plot(tfin,Cfin);
xlim(1.5e-3*[-1 1]);
xlabel('time(s)')
ylabel('C_1_2(t) using spline')
saveas(figure(101),['02-Correlation using spline between ',num2str(rr),
' and ', num2str(RR),...
    'BF=',num2str(F1),'-',num2str(F2),'kHz clipped at
',num2str(THR1),'NL '])


%% Gradient of Corr
DCfin=gradient(Cfin);
figure(102);clf;
plot(tfin*1000,DCfin/max(DCfin));
xlim(1.5*[-1 1]);
xlabel('Time (ms)')
ylabel('d/dt(C_1_2(t))')
```

```
saveas(figure(102),['03-DCfin between ',num2str(rr), ' and ',
num2str(RR),...
    'BF=',num2str(F1),'-',num2str(F2),'kHz at ',num2str(THR1),'NL '])

save DCfin DCfin

%% determination of the max and min of the green function
I=3.22e5:Nfin+1;
II=Nfin+1:Nfin+1+length(I)-1;

figure(111);clf;hold on
plot(tfin,DCfin/max(DCfin));
plot(tfin(I),DCfin(I)/max(DCfin),'g');
plot(tfin(II),DCfin(II)/max(DCfin),'r');
xlim(1.5e-3*[-1 1]);

Iposfin=find(tfin>=0);
Inegfin=find(tfin<=0);
tposfin=tfin(Iposfin);
tnegfin=tfin(Inegfin);
Tsfin=Ts/10;
[Mmin,Imin]=min(DCfin(II));
[Mmax,Imax]=max(DCfin(I));


%% symmetric of DCfin and its max time
CC=fliplr(DCfin);
CDsym=(DCfin-CC)./2;
figure(103);clf;hold on
plot(tfin,DCfin,'b');
plot(tfin,CDsym,'r');
xlim(1.5e-3*[-1 1]);
xlabel('time(s)')
ylabel('symmetric and d/dt(C_1_2(t)) using spline')
saveas(figure(103),['04-Symmetric and GF between ',num2str(rr), ' and
', num2str(RR),...
    'BF=',num2str(F1),'-',num2str(F2),'kHz clipped at
',num2str(THR1),'NL '])

[Mpossym,Ipossym]=min(CDsym(II));
[Mnegsym,Inegsym]=max(CDsym(I));
tmax=tfin(I(1)+Imax-1)
tmin=tfin(II(1)+Imin-1)
tminpossym=tfin(II(1)+Ipossym-1)

%% On a small time-window
DCfinlast=DCfin(Nfin+1-6000:Nfin+1+6000);
CDsymlast=CDsym(Nfin+1-6000:Nfin+1+6000);
figure(104);
plot(DCfinlast)
[Mmin,Imin2]=min(DCfinlast(6001:end));
Imin2=Imin2+6000;
[Mmax,Imax2]=max(DCfinlast(1:6000));
[Mpossym,Ipossym2]=min(CDsymlast(6001:end));
Ipossym2=Ipossym2+6000;
```

```
IM=[Imax2,Imin2,Ipossym2];
save IM IM

DD=abs(hilbert(DCfin));
DDsym=abs(hilbert(CDsym));

[Mpossymenv,Iposenvsym]=max(DDsym(II));
[Mposenv,Iposenv]=max(DD(II));
[Mnegenv,Inegenv]=max(DD(I));
tmaxnegenv=tfin(I(1)+Inegenv-1)
tmaxposenv=tfin(II(1)+Iposenv-1)
tmaxposenvsym=tfin(II(1)+Iposenvsym-1)

save TTmax tmax tmin tminpossym tmaxposenv tmaxnegenv tmaxposenvsym

%%%%%%%%%%%%%%%%%%%%%%%%%%%%%%%%%%%%%%%%%%%%%%%%%%%%%%%%%%%%%%%%%%%%%%%
%% Location of the different time-windows
STD=5.9e5:6.2e5;
STD2=4.086e5:4.086e5+length(STD);
STD3=3.425e5:3.425e5+length(STD);

figure(105);clf;
plot(tfin,DCfin);hold on
plot(tfin(STD),DCfin(STD),'r');hold on
plot(tfin(STD2),DCfin(STD2),'g'); hold on
plot(tfin(STD3),DCfin(STD3),'k')
xlabel('time (s)')
ylabel('GF')
saveas(figure(105),'05-Location of STD on GF')


%%%%%%%%%%%%%%%%%%%%%%%%%%%%%%%%%%%%%%%%%%%%%%%%%%%%%%%%%%%%%%%%%%%%%%%
%% Do the correlations receiver one by one. then sum all of them
tref=tminpossym;
trefenv=tmaxposenvsym;
trefneg=-tref;
trefnegenv=-trefenv;
Irefpos=find((tfin>=tref)&(tfin<=tref+Tsfin))
Irefneg=Nfin+1-Irefpos+1
Irefneg=find((tfin>trefneg)&(tfin<(trefneg+Tsfin)))-1
Irefposenv=find((tfin>trefenv)&(tfin<trefenv+Tsfin))
Irefnegenv=find((tfin>trefnegenv)&(tfin<(trefnegenv+Tsfin)))-1

%% computation of the correlation and SNR
I=3.22e5:3.26e5;
II=3.295e5:3.335e5;

figure(200);clf;
plot(tfin,DCfin,'b');hold on
plot(tfin(I),DCfin(I),'g');hold on
plot(tfin(II),DCfin(II),'r');

CORR=0
% figure(6);clf;
XX=0;
```

```
XXsym=0;
for jj=1:200; %size(Ll,2);
    jj
    temp=xcorr(DATA2(:,Ll(jj)),DATA1(:,Ll(jj)));
    tempfin=spline(tcorr,temp,tfin);
    Dtempfin=gradient(tempfin);
    Dtempfin1=Dtempfin(Nfin-6000:Nfin+6000);
    CORR=CORR+temp;
    Cfin=spline(tcorr,CORR,tfin);
    DCfin=gradient(Cfin);
    DCfin1=DCfin(Nfin-6000:Nfin+6000);


    DCsym=(-DCfin+fliplr(DCfin))./2;
    DCsym1=DCsym(Nfin-6000:Nfin+6000);
    Dtempsym=(-Dtempfin+fliplr(Dtempfin))./2;
    Dtempsym1=Dtempsym(Nfin-6000:Nfin+6000);
    DD=abs(hilbert(DCfin));
    DDsym=abs(hilbert(DCsym));

%     %%%for STD
    STDD=std(DCfin(:,STD),0,2);
    STDDsym=std(DCsym(:,STD),0,2);

    %%%for STD2
    STDD2=std(DCfin(:,STD2),0,2);
    STDDsym2=std(DCsym(:,STD2),0,2);

    %%%for STD3
    STDD3=std(DCfin(:,STD3),0,2);
    STDDsym3=std(DCsym(:,STD3),0,2);

    %Estimate of the arrival time on the envelope

    [Max_ENVpos(jj,1),Imin_ENVpos(jj,1)]=max(DD(II));

    [Max_ENVneg(jj,1),Imax_ENVneg(jj,1)]=max(DD(I));

    [Max_ENVsym(jj,1),Imax_ENVsym(jj,1)]=max(DDsym(II));

    %Estimation of the arrival time on the GF and of R(N,T)

   [Min_pos(jj,1),Iminpos(jj,1)]=min(DCfin(:,II));
    M_pos(jj)=-Min_pos(jj)/STDD;
    M_pos2(jj)=-Min_pos(jj)/STDD2;
    M_pos3(jj)=-Min_pos(jj)/STDD3;

    [Max_neg(jj,1),Imaxneg(jj,1)]=max(DCfin(:,I));
    M_neg(jj)=Max_neg(jj)/STDD;
    M_neg2(jj)=Max_neg(jj)/STDD2;
    M_neg3(jj)=Max_neg(jj)/STDD3;

    [Max_sym(jj,1),Imaxsym(jj,1)]=max(DCsym(:,II));
    M_sym(jj)=Max_sym(jj)/STDDsym;
```

```
    M_sym2(jj)=Max_sym(jj)/STDDsym2;
    M_sym3(jj)=Max_sym(jj)/STDDsym3;

   %%%computation of the SNR

    XX=(XX+Dtempfin1.^2);
    Varr(:,jj)=sqrt((jj/(jj-1)*(XX*1/jj-(1/jj*DCfin1).^2))/jj);
    Varrmin(jj)=median(Varr(IM(2)-2000:IM(2)+2000,jj));
    SNR(:,jj)=(1/jj)*DCfin1./(Varrmin(jj));

    XXsym=(XXsym+Dtempsym1.^2);
    Varrsym(:,jj)=sqrt((jj/(jj-1)*(XXsym*1/jj-(1/jj*DCsym1).^2))/jj);
    Varrminsym(jj)=median(Varrsym(IM(3)-2000:IM(3)+2000,jj));
    SNRsym(:,jj)=(1/jj)*DCsym1./(Varrminsym(jj));

end

%% SNR vs. sqrt(N) at the maximum point of the GF
figure(8);clf;
plot(sqrt(1:size(SNR,2)),SNR(IM(1),:),'r','linewidth',2); hold on
plot(sqrt(1:size(SNR,2)),-SNR(IM(2),:),'b','linewidth',2);
plot(sqrt(1:size(SNR,2)),SNRsym(IM(3),:),'k','linewidth',2)
title('SNR in function of N^1^/^2')
xlabel('N^1^/^2')
ylabel('SNR ')
legend('negative side','positive side','symmetric')
saveas(figure(8),'07-SNR in function of sqrt N')

%%%%%%%%%%%%%%%%%%%%%%%%%%%%%%%%%%%%%%%%%%%%%%%%%%%%%%%%%%%%%%%%%%%%%%%%%%%%%%%
%% time representation: phase velocity and group velocity
figure(11);clf;
subplot(1,2,1)
plot(-tfin(I(1)+Imaxneg-1),'+r');hold on
plot(tfin(II(1)+Iminpos-1),'+b');hold on
plot(tfin(II(1)+Imaxsym-1),'*k');
plot(1:0.1:length(Ll),tref,'--g','linewidth',4)
xlabel('Number of points')
ylabel('Maximum time on symmetric of d/dt(C_1_2(t)) ')
legend('negative side','positive side','symmetric'...
    ,'reference time')
subplot(1,2,2)
plot(-tfin(I(1)+Imax_ENVneg-1),'+r');hold on
plot(tfin(II(1)+Imin_ENVpos-1),'+b');hold on
plot(tfin(II(1)+Imax_ENVsym-1),'*k');
plot(1:0.1:length(Ll),trefenv,'--g')
xlabel('Number of points')
xlabel('Number of points')
ylabel('Maximum time on symmetric of the envelope of d/dt(C_1_2(t)) ')
saveas(figure(11),'10-Maximum time on symmetric of DCfin and its
envelope')

%% comparison between SNR and R(N,T) on the symmetric of the GF
figure(12);clf;
plot(sqrt(1:length(Ll)),M_sym/max(M_sym),'b','linewidth',2);hold on
plot(sqrt(1:length(Ll)),M_sym2/max(M_sym2),'b','linewidth',2);hold on
```

```
plot(sqrt(1:length(Ll)),M_sym3(1:length(Ll))/max(M_sym3(1:length(Ll))),
'g','linewidth',2);hold on
plot(sqrt(1:length(Ll)),SNRsym(IM(3),:)/max(SNRsym(IM(3),:)),'k','linew
idth',2);
xlabel('N^1^/^2')
ylabel('SNR')
title('SNR with VARR and MAx/max(MAX) in function of N^1^/^2 ')
legend('symmetric Max/STD2','symmetric Max/STD3','symmetric VARR')
saveas(figure(12),'14- Comparison two SNRs in function of sqrt N')

save SNR SNR
save SNRsym SNRsym
save Imaxneg Imaxneg
save Imaxsym Imaxsym
save Iminpos Iminpos
save Imax_ENVneg Imax_ENVneg
save Imax_ENVsym Imax_ENVsym
save Imin_ENVpos Imin_ENVpos

save M_sym M_sym
save M_sym2 M_sym2
save M_sym3 M_sym3
```

CODE TO COMPUTE THE WIGNERVILLE

```
%%%%%%%%%%%%%%%%%%%%%%%%%%%%%%%%%%%%%%%%%%%%%%%%%%%%%%%%%%%%%%%%%%%%%%%%%%%%
%%%%% WIGNERVILLE %%%%%%%%%%

DCORR=gradient(CORR);
DCORR1=DCORR(N-800:N+800);

CORR=DCORR1;

FeOLD=2.5e6;
freq_int1=[10e3 90e3];%%en hz;
[BB,AA]=butter(4,[freq_int1]/FeOLD*2);% Parametres du Filtre passe-
bande
CORR=filtfilt(BB,AA,CORR);

%%Downsample by a factor RATE to reduce the number of points in the
time-series
%%Need to Change the sampling frequency
RATE=4;
Fe2=FeOLD/RATE;
    CORR=decimate(CORR,RATE);


                    %%Redefine Time-frequency axis after resampling
                    Ts2=1/Fe2;
Mpoint=(length(CORR)-1)/2;%floor(delay/Ts);
tcorr2=[-(Mpoint):(Mpoint)]*Ts2;

Ipos2=find(tcorr2>=0);
Ineg2=find(tcorr2<=0);
tpos2=tcorr2(Ipos2);
Nc2=length(tcorr2); %2*N-1;
freqC2=[0:Nc2-1]/Nc2/Ts2; %%axe de frequence pour la correlation


%%%PLot the two correlations
figure;;hold on
subplot(2,1,1)
plot(tcorr2,CORR/max(abs(CORR)),'r');
xlabel('time')
ylabel('normalized correlation')
subplot(2,1,2)
plot(freqC2,abs(fft(CORR)),'k')
xlabel('frequency')
ylabel('FFT of the correlation')

%%%%%%%%%%%%%%%%%%Time Frequency analysis;
addpath('C:\Documents and Settings\Sarah Herbison\My
Documents\TIME_FREQUENCY\tftb-0.1\mfiles')

%%%%%%%%%%%%For Time Frequ Analysis
IcentTF=Ineg2;%pos2;%Ineg; %%Select only positive time
%%Make it even number-> remove last point;
```

```
IcentTF(end)=[];
TcentTF=tcorr2(IcentTF);
LENGTH1=length(TcentTF)/2;
Nc_TF=length(TcentTF);
freqC_TF=[0:Nc_TF-1]/Nc_TF/Ts2;
Csym=(-CORR+flipud(CORR))/2; %figure;plot(Csym)
CC=Csym(IcentTF).*hanning(length(IcentTF));
% CC=CORR(IcentTF).*hanning(length(IcentTF));

   %%Select Frequency equalization to improve bandwidth/ resolutions
   EXPOwhiten=0.01
       CC=FREQ_WHITEN_HANNINGonly(fft(CC),freq_int1,Fe2,EXPOwhiten);

        [Wig,Tc1,F1] =tfrspwv(CC+sqrt(-
1)*hilbert(CC),[1:length(TcentTF)],LENGTH1);
      %  [Wig, RWig] =tfrrspwv(CC+sqrt(-
1)*hilbert(CC),[1:length(TcentTF)],LENGTH1);
     Wig=((Wig.'));%%each column is a frequency

       Fc1=[0:LENGTH1-1]/length(TcentTF)/Ts2;
       If1=find(Fc1>=freq_int1(1) & Fc1<=freq_int1(2) );
       Fc2=Fc1;If2=If1;

       [RWig, Tc1, Fc2,Wt] =
tfrscalo(CC,[1:length(TcentTF)],sqrt(length(TcentTF))/4,freq_int1(1)/Fe
2,freq_int1(2)/Fe2 );
       Fc2=Fc2*Fe2; %[0:LENGTH1-1]/length(TcentTF)/Ts;
       If2=[1:length(Fc2)] ;


       RWig=((RWig.'));%%each column is a frequency

       RMMamp=max(max(abs(RWig)));
       MMamp=max(max(abs(Wig)));

       Scale=10 %%in DB
       figure;clf;hold on
                subplot(2,1,1);hold on

pcolor(TcentTF,Fc1(If1),20*log10(abs(Wig(:,If1).')/MMamp))
               hold on
               shading interp
               caxis([-1 0]*Scale);colorbar
       %        xlim(0.1/2*[-1 1])
               ylim(freq_int1)
               hold off
               axis tight
       title('Smooth-Pseudo Wigner Ville - Ineg on
symGrad(CORR)BF1_2_._5_N_L')

       subplot(2,1,2);hold on

pcolor(TcentTF,Fc2(If2),20*log10(abs(RWig(:,If2).')/RMMamp))
               hold on
               shading interp
```

```
                caxis([-1 0]*Scale);colorbar
        %        xlim(0.1/2*[-1 1])
                ylim(freq_int1)
                hold off
                axis tight
title('Scalogram')
```

REFERENCES

- Achenbach, J.D., (1993), *Wave Propagation in Elastic Solids*, North Holland, Amsterdam.

- Achenbach, J.D., (2000), "Quantitative non-destructive evaluation", International Journal of Solids and Structures 37, Issues 1-2, p. 13-27.

- Akolzin, A., and Weaver R. L., (2004), "Generalized Berry conjecture and mode correlations in chaotic plates", Phys. Rev. E 70, 046212.

- Derode, A., Tourin, A., and Fink, M., (1999), "Ultrasonic pulse compression with one-bit time reversal through multiple scattering", J. Appl. Phys. 85, 6343.

- Evans, M.J., and Cawley, P., (1999), "Measurement and prediction of diffuse fields in structures" J. Acoust. Soc. Am., 106, 3348-3360.

- Farrar, C., and James, G., (1997), "System identification from ambient vibration measurements on a bridge," J. Sound Vib. 205, 1-18.

- Fichtner, A., Bunge, H.-P., and Igel, H., (2006), "The adjoint method in seismology. I. Theory", Phys. of the Earth and Planetary Interiors 157, 86-104.

- Giurgiutiu, V., (2007), *Structural Health Monitoring: with Piezoelectric Wafer Active Sensors*, Academic Press, NY.

- Langley, R.S., (2007), "On the diffuse field reciprocity relationship and vibrational energy variance in a random subsystem at high frequencies", J. Acoust. Soc. Am. 121, 913-921.

- Larose, E., Derode, A., Campillo, M., and Fink, M., (2004), "Imaging from one-bit correlations of wide-band diffuse wavefields", J. Appl. Phys. 95 (12), pp 8393-8399.

- Larose, E., Lobkis, O.I., and Weaver, R.L., (2006), "Passive correlation imaging of a buried scatterer," J. Acoust. Soc. Am., 119, 3549-3552.

- Larose, E., Roux P., Campillo, M., (2007), "Reconstruction of Rayleigh-Lamb dispersion spectrum based on noise obtained from an air-jet forcing", J. Acoust. Soc. Am., 122 pp 3437.

- Larose, E., Roux, P., Campillo, M., and Derode, A., (2008), "Fluctuations of correlations and Green's function reconstruction: Role of scattering", Am. Institute of Physics 103, 114907-1.

- Lobkis, O. I., and Weaver, R.L., (2003), "Coda-Wave Interferometry in Finite Solids: Recovery of P-to-S Conversion Rates in an Elastodynamic Billiard", Phys. Rev. Lett. 90, 254302.

- Lu, Y., and Michaels J. E., (2006), "A methodology for structural health monitoring with diffuse ultrasonic waves in the presence of temperature variations", Ultrasonics, 43, 717-731.

- Michaels, J. E., and Michaels, T. E., (2005), "Detection of Structural Damage from the Local Temporal Coherence of Diffuse Ultrasonic Signals", IEEE trans. on Ultrason., Ferroelec., and Frequ. Control, 52.

- Paul, A., Campillo, M., Margerin, L., Larose, E., and Derode, A., (2005), "Empirical synthesis of time-asymmetrical Green functions from the correlation of coda waves", J. Geophys. Res. 110, L003521.

- Proakis, J.G., (1995), *Digital Communications*, McGraw-Hill, NY, pp. 159-163.

- Roux, P., Sabra, K.G., Kuperman, W., and Roux, A., (2004), "Ambient noise crosscorrelation in free space: Theoretical approach", J. Acoust. Soc. Am. 117, 79–84.

- Sabra, K.G., Roux, P., and Kuperman, W.A., (2005a), "Arrival-time structure of the time-averaged ambient noise cross-correlation function in an oceanic waveguide," J. Acoust. Soc. of Am 117, 164-174.

- Sabra, K.G., Roux, P., and Kuperman, W.A., (2005b), "Emergence rate of the time domain Green's function from the ambient noise cross correlation," J. Acoust. Soc. Am. 118, 3524-3531.

- Sabra, K.G., Gerstoft, P., Roux, P., Kuperman, W.A. and Fehler, M.C. (2005c). "Surface wave tomography from microseisms in Southern California," Geophys. Res. Lett. 32, L14311.

- Sabra, K.G., Winkel, E.S., Bourgoyne, D.A., Elbing, B.R., Ceccio, S.L., Perlin, M., and Dowling, D.R., (2007a), "On using cross-correlation of turbulent flow-induced ambient vibrations to estimate the structural impulse response. Application to structural health monitoring," J. Acoust. Soc. Am. 121, 1987-2005.

- Sabra, K.G., Srivastava A., Lanza di Scalea, F., Bartoli, I., Rizzo, P., and Conti S., (2008), "Structural health monitoring by extraction of coherent guided waves from diffuse fields", J. Acoust. Soc. Am. 123, EL8-EL13.

- Shapiro, N.M., Campillo, M., Stehly L., and Ritzwoller, M. (2005), "High resolution surface-wave tomography from ambient seismic noise," Science 29, 1615–1617.

- Snieder, R., Grêt, A., Douma, H., and Scales, J., (2002), "Coda wave interferometry for estimating nonlinear behaviour in seismic velocity", Science 295, 2253–2255.

- Snieder, R., (2004), "Extracting the Green's function from the correlation of coda waves: A derivation based on stationary phase", Phys. Rev. E 69, 046610.

- Snieder, R. and Cafak, E., (2006), "Extracting the building response using seismic interferometry; theory and application to the Millikan Library in Pasadena, California", Bull. Seism. Soc. Am. 96, 586-598.

- Tarantola, A., (1984), "Inversion of seismic reflection data in the acoustic approximation", Geophysics vol. 49, no. 8, p. 1259-1266.

- Tarantola, A., (1987), *Inverse Problem Theory: Methods for Data Fitting and Model Parameter Estimation,* Elsevier, Amsterdam.

- Van Wijk, K., (2006), "On estimating the impulse response between receivers in a controlled ultrasonic model," Geophysics 71, SI79-SI84.

- Weaver, R.L., (1982), "On diffuse waves in solid media", J. Acoust. Soc. Am. 71, 1608–1609.

- Weaver, R.L., (1984), "Diffuse Waves in Finite Plates", J. Sound Vib. 94, 319–335.

- Weaver, R.L., (1986), "Laboratory studies of diffuse waves in plates", J. Acoust. Soc. Am. 79, 919-923.

- Weaver, R.L., and Lobkis, O.I., (2001), "Ultrasonics without a source: thermal fluctuation correlations at MHz frequencies," Phys. Rev. Lett. 87, 134301.

- Weaver, R.L., and Lobkis, O.I., (2004), "Diffuse fields in open systems and the emergence of the Green's function," J. Acoust. Soc. Am. 116, 2731-2734.

- Weaver, R.L. and Lobkis. O.I., (2005), "The mean and variance of diffuse field correlations in finite bodies" J. Acoust. Soc. Am. 118, Issue 6, pp. 3447-3456.

- Wilcox, P.D., Lowe, M.J.S. and Cawley, P. (2001). "Mode and transducer selection for long range Lamb wave inspection," J. of Intelligent Material Systems and Structures, Vol. 12, pp. 553–566.